

The electrocatalytic ORR activity of nanostructured manganese oxides in aprotic media

Von der Fakultät für Mathematik und Naturwissenschaften
der Carl von Ossietzky Universität Oldenburg
zur Erlangung des Grades und Titels eines

Doktors der Naturwissenschaften

Dr. rer. nat.

angenommene Dissertation

von Herrn Matthias Augustin
geboren am 5.8.1984 in Buxtehude



Gutachter: Prof. Dr. Jürgen Parisi

Zweiter Gutachter: Prof. Dr. Matthias Busse

Tag der Disputation: 25. Juni 2015

Abstract

In this work nanostructured manganese oxides were synthesized and characterized with respect to their electrocatalytic activities for the oxygen reduction reaction (ORR) in aprotic media. The carbon substrate used for the electrochemical measurements shows an ORR pathway, which results in an electron transfer subsequent to a chemical reaction. The intermediate species O_{ads} being generated during this process, is supposed to enhance the decomposition of aprotic electrolytes. Mn_3O_4 is catalytically active for this mechanism, whereas $\alpha\text{-}Mn_2O_3$ catalyzes a direct electrochemical reduction of O_2 , which results in the formation of the desired final product Li_2O_2 . Based on the obtained mechanistic insights conclusions on the morphological and structural properties of an ideal ORR electrocatalyst are drawn.

Kurzfassung

In dieser Arbeit wurden nanostrukturierte Manganoxide synthetisiert und auf ihre elektrokatalytische Aktivität für die Sauerstoffreduktionsreaktion (ORR) in aprotischen Elektrolyten untersucht. Das Kohlenstoff-Substrat für die elektrochemischen Messungen führt zu einem ORR-Mechanismus, bei dem die Sauerstoff-Reduktion nach einer chemischen Reaktion erfolgt. Von dem hierbei entstehenden Zwischenprodukt O_{ads} wird angenommen, dass es zu einer Zersetzung von aprotischen Elektrolyten beiträgt. Mn_3O_4 ist für diesen Mechanismus katalytisch aktiv, wohingegen $\alpha\text{-}Mn_2O_3$ eine direkte elektrochemische Reduktion von O_2 katalysiert, die zur Bildung des gewünschten Endprodukts Li_2O_2 führt. Auf Grundlage dieser Ergebnisse werden Rückschlüsse auf die morphologischen und strukturellen Eigenschaften eines idealen ORR-Katalysators gezogen.

FOR THOSE ABOUT TO ROCK

Für meine indonesischen Mädels

„Wer soll dir verraten, welches Unheil durch deine Erfindungen verhindert wurde? Zehn Katastrophen oder zwanzig oder auch nur eine einzige, das Verhinderte bleibt dir ewig verborgen, nur was du angerichtet hast, ist sichtbar.“

(Jurek Becker, Jakob der Lügner)

„Probleme sind dazu da, um sich zu vermehren,
... wenn man nicht hinguckt, mal 'n Moment.“

(Helge Schneider, Kaktist)

Table of contents

Index of figures.....	iv
Index of schemes	vii
Index of tables.....	viii
1. Introduction	1
2. Fundamentals	3
2.1. Lithium/air batteries	3
2.2. The ORR/OER processes in the aprotic Li/air system	6
2.3. Aprotic electrolyte solvents	9
2.4. Electrochemical kinetics and catalysis	13
2.4.1. Electrochemical theory	13
2.4.2. Catalysts for the Li/air system	19
2.4.3. Manganese oxides.....	21
3. Experimental part	23
3.1. Materials.....	23
3.2. Manganese oxide synthesis	24
3.2.1. Mixed-phase manganese oxide particles	24
3.2.2. Pure-phase manganese oxide particles.....	24
3.3. Morphological and structural analysis	25
3.3.1. Electron microscopy	25
3.3.2. X-ray diffraction (XRD) and <i>in situ</i> -XRD	26
3.3.3. Thermogravimetric analysis (TGA) and differential scanning calorimetry (DSC).....	28
3.3.4. N ₂ adsorption-desorption.....	28

Table of contents

3.4. Electrochemical analysis of the catalytic activity	29
3.4.1. Electrode preparation	29
3.4.2. Electrochemical measurements	29
4. Results & Discussion	33
4.1. Synthesis and characterization of the manganese oxides	33
4.1.1. Mixed-phase manganese oxides	33
4.1.1.1. Mn(II) glycolate precursor by polyol synthesis	33
4.1.1.2. Mixed-phase Mn ₃ O ₄ /Mn ₅ O ₈ by calcination	35
4.1.2. Nanostructured pure-phase manganese oxides	37
4.1.2.1. Mn(II) glycolate precursor by a modified polyol synthesis.....	38
4.1.2.2. The formation of various Mn _x O _y phases during heating.....	41
4.1.2.3. Mn _x O _y species by calcination at different temperatures	46
4.1.2.4. The formation of pure-phase Mn ₅ O ₈ by calcination	52
4.1.2.5. Morphological and structural characterization of the Mn ₃ O ₄ , Mn ₅ O ₈ and α-Mn ₂ O ₃ compounds	55
4.1.3. Conclusion	61
4.2. Characterization of the electrochemical system.....	63
4.2.1. Electrolyte characterization	63
4.2.2. The impact of model electrode properties on the ORR processes	70
4.2.3. The impact of electrode rotation on the ORR processes.....	76
4.2.4. Conclusion	79
4.3. The effect of the Mn _x O _y catalysts on the ORR processes	81
4.3.1. The ORR activities at a scan rate of 100 mV/s.....	81
4.3.2. The ORR mechanisms at a scan rate of 100 mV/s.....	87
4.3.2.1. The ORR processes on the carbon electrode surfaces	92
4.3.2.2. The ORR processes in the presence of α-Mn ₂ O ₃	94

4.3.2.3. The ORR processes in the presence of Mn_3O_4 or Mn_5O_8	98
4.3.3. Conclusion.....	101
4.4. The scan rate dependence of the observed ORR processes	103
4.4.1. The scan rate dependence of the ORR mechanisms	103
4.4.1.1. The ORR processes on GC and $\alpha\text{-Mn}_2\text{O}_3/\text{C}$	108
4.4.1.2. The ORR processes on VC and $\text{Mn}_5\text{O}_8/\text{C}$	110
4.4.1.3. The ORR processes on $\text{Mn}_3\text{O}_4/\text{C}$	112
4.4.2. The scan rate dependence of the ORR activities.....	117
4.4.3. Conclusion.....	119
5. Conclusion & Outlook.....	121
References	125

Index of figures

Figure 2.1: Four types of Li/air cells with (a) aprotic, (b) aqueous, (c) hybrid (aprotic/aqueous) and (d) solid-state electrolytes.....	4
Figure 2.2: Galvanostatic discharge and charge curves of a Li/O ₂ cell	5
Figure 2.3: Example of (a) a CV measurement and (b) the cathodic (ORR) scan.....	14
Figure 2.4: The influence of an applied overpotential on the activation energy barrier for an electrochemical reaction.....	15
Figure 2.5: Example of a Tafel plot of the ORR region observed during a CV measurement.....	17
Figure 2.6: Metal prices and abundance (relative to Si abundance) of the chemical elements in Earth's upper continental crust.....	20
Figure 3.1: (a) Schematic representation and (b) photo of the setup in the Ar-filled glove box	30
Figure 4.1:(a) XRD pattern and (b) TEM image of the Mn(II) glycolate particles after synthesis at 200°C for 50 min	34
Figure 4.2: XRD pattern of the mixed-phase Mn _x O _y product obtained after calcination at 400°C for 2 h in O ₂ atmosphere.....	35
Figure 4.3: TEM images of the Mn ₃ O ₄ /Mn ₅ O ₈ particles.....	36
Figure 4.4: Powder XRD pattern of Mn(II) glycolate particles after synthesis at 170°C for (a) 1 h and (b) 7 h	39
Figure 4.5: (a) SEM and (b), (c) TEM images of the Mn(II) glycolate precursor synthesized at 170°C for 7 h	40

Figure 4.6: *In situ*-XRD patterns recorded during the heating of the Mn(II) glycolate precursor from 35°C to 700°C in an O₂ flow..... 41

Figure 4.7: TGA/DSC measurements recorded during the heating of the Mn(II) glycolate precursor to 700°C in Ar and O₂/Ar (1:2) atmospheres 43

Figure 4.8: Powder XRD patterns of the Mn_xO_y products obtained after calcination at temperatures between 320°C and 550°C for 2 h 47

Figure 4.9: Mn_xO_y low-angle reflection intensities detected at different calcination temperatures in Ar (black) and O₂ atmospheres (red) 48

Figure 4.10: *In situ*-XRD patterns during constant heating of the Mn(II) glycolate precursor at 400°C for 350 min in an O₂ flow 53

Figure 4.11: XRD pattern of Mn₅O₈ obtained by calcination at 400°C for 5 h in an O₂ atmosphere..... 54

Figure 4.12: Schemes of the unit cells of the Mn_xO_y species of interest for the ORR investigations 56

Figure 4.13: TEM images of the (a) Mn₃O₄, (b) Mn₅O₈ and (c), (d) α-Mn₂O₃ particles..... 57

Figure 4.14: (a) N₂ adsorption-desorption isotherms and (b) the corresponding pore size distributions of Mn₃O₄, Mn₅O₈ and α-Mn₂O₃ 59

Figure 4.15: LSV measurements recorded in different Ar-saturated electrolytes 64

Figure 4.16: CV measurements recorded in different O₂-saturated electrolytes 66

Figure 4.17: CV measurements recorded with GC and Nafion[®]-coated GC.. 71

Figure 4.18: Nicholson/Shain plots for GC and GC-N 73

Index of figures

Figure 4.19: Nicholson/Shain plots for GC with (a) $\omega = 1000$ rpm and (b) $\omega = 200$ rpm.....	78
Figure 4.20: CV measurements recorded with different working electrodes ..	82
Figure 4.21: Representative Tafel plots for different working electrodes.....	85
Figure 4.22: Nicholson/Shain plots for the VC-based electrodes.....	90
Figure 4.23: Variation of the n^* values with the applied scan rate.....	106
Figure 4.24: Variation of the Tafel slopes with the applied scan rate.	107
Figure 4.25: Variation of the (a) Tafel slopes and (b) onset potentials with the applied scan rate.....	114
Figure 4.26: Variation of the peak potentials with the scan rate	116
Figure 4.27: Variation of the (a) apparent rate constants k_{app}^0 and (b) scan rate-normalized k_{app}^0 with the scan rate	117

Index of schemes

Scheme 2.1: Representation of an aprotic Li/O₂ cell8

Scheme 4.1: Idealized model for the investigated Mn_xO_y/C electrodes.89

Scheme 4.2: Different ORR mechanisms detected for different working electrodes at $\nu = 100$ mV/s92

Scheme 4.3: ORR mechanisms suggested to take place on the surface of α -Mn₂O₃/C.96

Scheme 4.4: ORR mechanisms suggested to take place on the surface of Mn₃O₄/C99

Scheme 4.5: ORR mechanisms detected at various scan rates 104

Index of tables

Table 2.1: Comparison of the theoretical properties of aqueous and aprotic Li/air systems	5
Table 3.1: Chemicals used for Mn(II) glycolate synthesis; gases used for calcination and TGA/DSC as well as electrochemical measurements.*	23
Table 3.2: Chemicals used for electrode preparation and electrochemical measurements.*	23
Table 4.1: Loss of sample masses detected during the TGA measurements and attributed processes in Ar and O ₂ /Ar atmospheres.....	44
Table 4.2: Crystalline Mn _x O _y phases obtained after calcination at temperatures between 320°C and 550°C in Ar and O ₂ atmospheres	49
Table 4.3: Summary of the properties of the Mn _x O _y samples of interest for the ORR investigations.....	62
Table 4.4: Comparison of the ORR potentials and ORR/OER potential gaps for the different electrolytes	68
Table 4.5: Comparison of ORR potentials and kinetic parameters for GC and GC-N	72
Table 4.6: Potentials and kinetic parameters obtained from CV measurements recorded with a GC at $\nu = 100$ mV/s with different rotational frequencies	76
Table 4.7: ORR peak and onset potentials for the different electrode materials	83
Table 4.8: ORR/OER potential differences and electric charge ratios for the different electrode materials.....	84

Table 4.9: Partial current densities j_0 and apparent reaction rate constants k_{app}^0 for the different electrode materials 86

Table 4.10: Tafel slopes and αn values derived thereof for the different electrode materials 87

Table 4.11: Potentials and kinetic parameters for GC and VC at $\nu = 100$ mV/s with $\omega = 0$ rpm and $\omega = 200$ rpm. 93

Table 4.12: Potentials and kinetic parameters for α -Mn₂O₃/C at $\nu = 100$ mV/s with $\omega = 0$ rpm and $\omega = 200$ rpm. 97

Table 4.13: Potentials and kinetic parameters for Mn₃O₄/C and Mn₅O₈/C at $\nu = 100$ mV/s with $\omega = 0$ rpm and $\omega = 200$ rpm. 100

Table 4.14: Overview of the final products proposed to be generated during the diffusion-controlled ORR processes observed for GC and α -Mn₂O₃/C. . 108

Table 4.15: Overview of the final products proposed to be generated during the ORR processes observed for VC and Mn₅O₈/C. 110

Table 4.16: Overview of the final products proposed to be generated during the diffusionless ORR processes observed for Mn₃O₄/C. 112

1. Introduction

The interest in the secondary Li/air battery has grown rapidly over the past two decades, as it exhibits a theoretical specific energy of more than 3,400 Wh/kg[1,2]. Even by taking into account the weight of the cell components, the practically achievable energy density is around 1,700 Wh/kg, which equals that of gasoline and is well beyond those of conventional lithium ion (160 Wh/kg), Ni metal hydride (50 Wh/kg) and Zn/air cells (350 Wh/kg)[2–5]. These large energy densities are due to the very light-weight cell components, i.e., Li metal as anode and porous carbon as cathode material. The use of a Li metal anode has the further advantage, that lithium is the most electronegative metal, which – in combination with the active (reacting) species oxygen (O_2) – results in a high cell voltage.

Despite the relevance of the Li/air system surprisingly little is known about the actual mechanisms of the discharge (oxygen reduction, ORR) and charge (oxygen evolution, OER) reactions. Information about the discharge and charge mechanisms, however, is needed to overcome the major drawback of the Li/air system: the low electric efficiency due to large discharge and charge overpotentials. In order to reduce these overpotentials (and thus increase the electric efficiency) the impact of possible catalysts was investigated in a vast number of studies over the past years. Despite this large effort of scientific research, the knowledge obtained about active catalysts is rather small. A main reason for this is the fact that until 2012, most of the studies about the Li/air battery were conducted with electrolytes based on organic carbonate solvents, which were adopted from the Li ion system and considered to be suitable for the Li/air system. As these electrolytes are not stable, the majority of investigations about the reaction mechanisms in this system were rather reports on the decomposition of

1. Introduction

electrolytes. A stable electrolyte has not been found yet, although some solvents are proposed to exhibit sufficient stability under laboratory conditions. The lack of a stable electrolyte led to a decreased interest of the major industries in the Li/air system. Therefore, most of the recent investigations are conducted by simply scanning whole classes of suitable solvents in order to find a stable electrolyte. Many of these studies are done by galvanostatic cycling, from which no or only little insight into the reaction mechanisms can be obtained. Regarding the recent research on electrocatalysts for the Li/air system, a similar scientific approach is observed. The majority of catalytic investigations were (and still are) conducted (i) by galvanostatic cycling, i.e., give no mechanistic insight, and (ii) in several different electrolytes, which makes a comparison in terms of reaction mechanisms hardly possible. More detailed electrochemical studies on ORR/OER catalysts and/or reaction mechanisms, on the other hand, are mainly conducted in aqueous media, for which the results are hardly comparable to those obtained in aprotic media.

This work provides insight into the ORR reaction mechanisms observed in the presence of three nanostructured manganese oxide (Mn_xO_y) catalysts in an aprotic electrolyte, which is stable under the working conditions. The catalytic ORR activities of these compounds are investigated by comparison to those of carbon reference materials. Prior to the electrochemical analysis, the synthesis of the particles is presented. The influence of different process parameters on the sizes and morphologies of the obtained particles is discussed as well as the formation of different Mn_xO_y phases, which is observed during heat treatment by *in situ* investigations.

2. Fundamentals

In this chapter, the currently discussed types of the Li/air system and their respective advantages and disadvantages will be introduced. As this work investigates the aprotic Li/air battery, the different reactions occurring during discharge and charge in non-aqueous electrolytes and a short overview of several electrolyte solvents are presented. The electrochemical basics used for the investigation of the electrocatalytic activities are provided together with a brief summary of the most promising catalysts for the Li/air battery.

2.1. *Lithium/air batteries*

Currently mainly four types of Li/air cells are under investigation, which are named based on the class of electrolytes used in the system (see Figure 2.1 on the next page): (a) the aprotic, (b) the aqueous, (c) the hybrid aprotic/aqueous and (d) the solid-state Li/air system.

The least investigated of these different Li/air cells is the solid-state Li/air system (see Figure 2.1.d), which is due to the fact that up to now, no solid electrolyte exhibits sufficient Li^+ ion conductivity. Improvements with regard to energy density and power density are still due for this cell type, which makes it less attractive as an alternative to Li ion batteries.

The main advantage of the aqueous over the aprotic system (see Figure 2.1.a and Figure 2.1.b, respectively) is that moisture in the air, which is provided on the cathode side, will not result in side reactions or cell failure. However, the aqueous electrolyte has the disadvantage, that the contact of water with of the Li metal anode has to be prevented by a protective layer,

2.1. Lithium/air batteries

which decreases the volumetric and gravimetric capacity. This is also the case for the hybrid Li/air system (see Figure 2.1.c)[5].

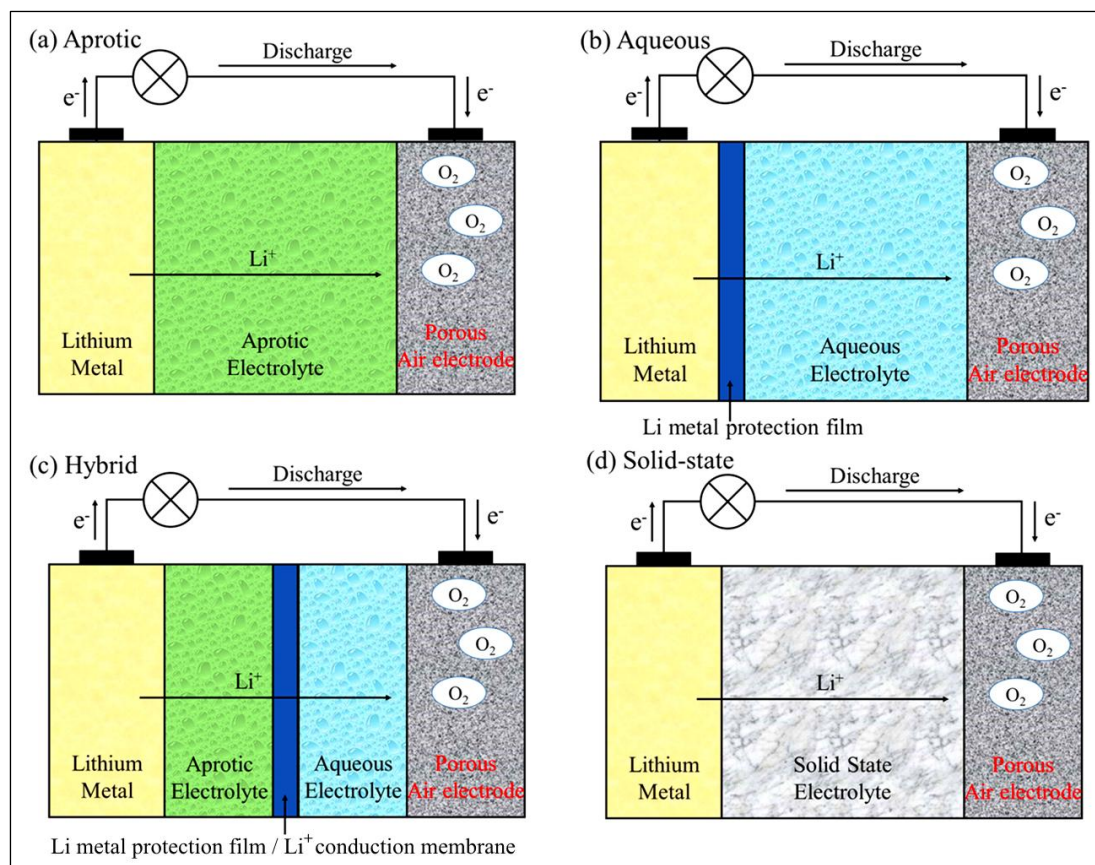


Figure 2.1: Four types of Li/air cells with (a) aprotic, (b) aqueous, (c) hybrid (aprotic/aqueous) and (d) solid-state electrolytes[5].

Another disadvantage of the aqueous Li/air system is a more than 30% lower theoretical energy density in comparison to that of the aprotic system (see Table 2.1 on the next page), which is due to (i) several possible electrochemical and chemical reaction pathways and (ii) the low solubility of the discharge product LiOH in the aqueous electrolyte[6].

As the aprotic Li/air cell (Figure 2.1.a) is the most-promising system in terms of energy density and possible applications, this work focuses on the effect of ORR catalysts in non-aqueous electrolytes.

Table 2.1: Comparison of the theoretical properties of aqueous and aprotic Li/air systems[1].

	Discharge product	Cell voltage / V	Specific density / Wh/kg	Energy density / Wh/L
Aprotic	Li ₂ O ₂	3.0	3,505	3,436
Aqueous	LiOH	3.2	3,582	2,234

Despite the advantages of the aprotic Li/air battery, several unsolved problems still prevent an industrial application of this system. One of the most prominent disadvantages is the occurrence of large overpotentials, which are obtained during discharge and especially recharge, making the system quite inefficient (see Figure 2.2).

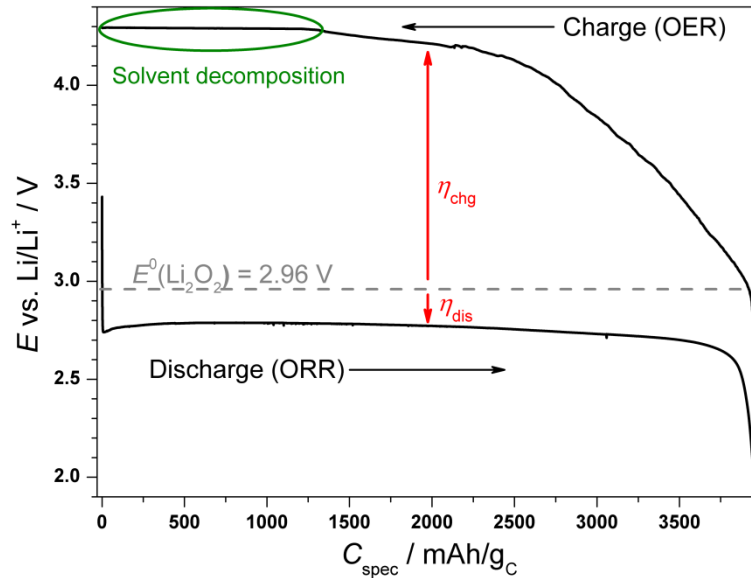


Figure 2.2: Galvanostatic discharge and charge curves of a Li/O₂ cell. Cell setup: Li metal anode, Vulcan[®] carbon powder as active cathode material; electrolyte: 1 M Li⁺/dimethyl-sulfoxide (DMSO); $p(\text{O}_2) = 2$ bar; specific discharge/charge current $i = \pm 100 \mu\text{A}/\text{cm}^2$; the dashed grey line indicates the reversible formation potential of lithium peroxide (Li₂O₂) E^0 vs. Li/Li⁺ = 2.96 V[7,8]; η_{dis} and η_{chg} are the overpotentials observed during discharge and charge with respect to E^0 .

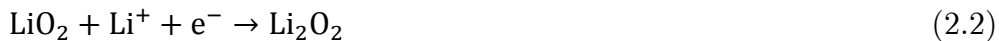
2.2. The ORR/OER processes in the aprotic Li/air system

The galvanostatic discharge/charge curves of a Li/O₂ cell depicted in Figure 2.2 show the main problems, which prevent the aprotic Li/air system from its practical application. During cycling large overpotentials η_{dis} and η_{chg} of the ORR and OER processes are obtained, which results in a low voltage efficiency $\mu_E = E_{\text{dis}}/E_{\text{chg}}$. The large charge overpotentials furthermore lead to a decomposition of the aprotic electrolyte solvent at too high potentials (highlighted green in Figure 2.2).

In order to solve these problems much research focusing on ORR/OER electrocatalysts and the screening of stable electrolyte solvents was carried out during the past years. The fundamentals of the reaction processes, suitable electrolyte solvents and possible catalysts for the aprotic system will be described in the following sections.

2.2. The ORR/OER processes in the aprotic Li/air system

The oxygen reduction reaction (ORR) is the discharge reaction taking place at the cathode side of the Li/air cell, for which different mechanisms have been suggested for aprotic media. Based on results from cyclic voltammetry (CV) measurements Lacroix *et al.* proposed the following sequence of possible cathode reactions[9,10]:



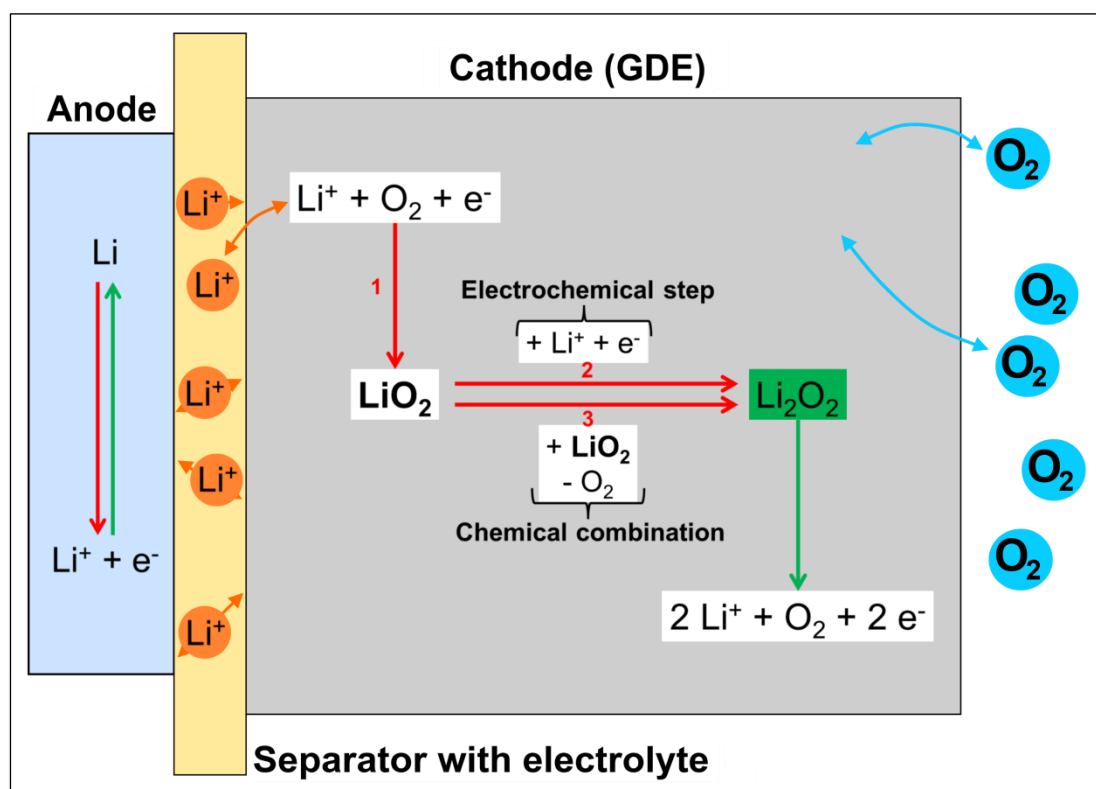
During discharge a one-electron reduction of oxygen (O₂) to superoxide (LiO₂, eq. (2.1)) is followed by a further one-electron reduction and/or a

chemical disproportionation of LiO_2 to lithium peroxide (Li_2O_2 , eqs. (2.2)-(2.3)), which has been detected as a discharge product in porous carbon electrodes[11–13]. This mechanism was confirmed by *in situ*-surface-enhanced Raman spectroscopy (SERS) and *in situ*-differential electrochemical mass spectroscopy (DEMS), which revealed lithium superoxide (LiO_2) as an intermediate product during the ORR in non-aqueous solvents[14]. Furthermore, this study provided evidence for the subsequent chemical disproportionation of LiO_2 to Li_2O_2 (eq. (2.3))[14]. A further two-electron reduction of Li_2O_2 takes place at lower potentials and results in the formation of lithium oxide (Li_2O , eq. (2.4)). Although a discharge to Li_2O could increase the theoretical specific energy of the aprotic Li/air system by about 800 Wh/kg[15], the electrochemically irreversible Li_2O formation would result in larger charge overpotentials. Therefore, Li_2O_2 (with a reversible formation potential of $E^0 = 2.96$ V[7,16]) is generally considered as the desired discharge product[3,10,17].

During recharge (oxygen evolution reaction, OER) Li_2O_2 is oxidized *via* a direct two-electron step to O_2 without the formation of a LiO_2 intermediate[14]. Hence, the OER does not proceed *via* a reverse reaction pathway of the ORR (eqs. (2.1)-(2.3)). The desired ORR and OER processes are depicted in Scheme 2.1 (see next page).

The ORR processes discussed above (eqs. (2.1)-(2.3) and Scheme 2.1) are considerably influenced by the nature of the electrode and catalyst surfaces, i.e., the number of active sites as well as physicochemical properties, such as O_2 adsorption enthalpies.

2.2. The ORR/OER processes in the aprotic Li/air system



Scheme 2.1: Representation of an aprotic Li/O₂ cell. The ORR processes (red arrows) are shown for the formation of the desired discharge product Li₂O₂ (eqs. (2.1)-(2.3)); the charge reaction (OER) is shown by the green arrow.

A dependence of the reduction mechanism and the discharge product on the respective catalysts was suggested in a CV study investigating glassy carbon and polycrystalline noble metal electrodes (Au and Pt) in aprotic organic electrolytes suggested [18]. A theoretical study suggested that the reduction pathway to Li₂O₂ *via* the rate-determining formation of LiO₂ (eqs. (2.1)-(2.3)) is catalyzed by electrode materials with low oxygen adsorption strength, e.g., carbon[19]. The first ORR step is assumed to be the formation of superoxide radicals as weakly adsorbed species, which are solvated by solvent molecules of the used electrolyte. The O₂⁻ radicals subsequently react with Li⁺, thus forming adsorbed LiO₂[10]. Furthermore, the authors of the theoretical study suggested an alternative ORR mechanism to take place in the presence of electrode materials and catalysts with a large number of active sites and/or

large oxygen chemisorption energies, such as Pt. Here, O_2 is dissociatively adsorbed on the surface (eq. (2.5)) and subsequently reduced to $[LiO]_{ads}$ species (eq. (2.6)), from which a stoichiometric equivalent to Li_2O_2 is generated by another electron transfer (eq. (2.7))[19].



The adsorbed oxygen atoms produced in the first chemical step of this mechanism (eq. (2.5)) were suggested to enhance the decomposition of dimethyl ether-based electrolytes[20]. Based on DFT and experimental studies it was proposed that although the first reduction product on Au metal might be LiO_2 (eq. (2.1)), it will finally form $[LiO]_{n,ads}$ species[21–23]. These compounds were also shown to be the energetically favored products on Pt metal and proposed to be further reduced to $[Li_2O]_{n,ads}$ species on Au as well as Pt surfaces[21–23]. Therefore, the current investigation of cathode substrate materials and catalysts focuses on compounds with low oxygen adsorption enthalpies, which are active for the non-dissociative ORR mechanism (eqs. (2.1)-(2.3))[19]. An overview of the currently investigated catalysts for the Li/air system is given in section 2.4.2.

2.3. Aprotic electrolyte solvents

One of the major limitations of the aprotic Li/air system is the electrochemical stability of the non-aqueous electrolytes. The search for a stable electrolyte is complicated by the very different properties a suitable solvent has to exhibit. The most important of these properties are (i) stability against Li metal (on the anode side), (ii) stability against the O_2^-

2.3. Aprotic electrolyte solvents

radicals produced during the ORR (on the cathode side) and (iii) low volatility for long-term applications.

Further properties of suitable solvents include a high O_2 solubility and the stabilization of the LiO_2 intermediate to prevent a direct formation of Li_2O_2 or even Li_2O . In an early approach Laoire *et al.* investigated possible electrolyte solvents with respect to their capability of LiO_2 stabilization[10]. This study was conducted by considering the HSAB (**h**ard and **s**oft **a**cids and **b**ases) concept established by Pearson[24]. In short, this theory ascribes acidic or basic properties to chemical species based on their strengths for electron acceptance (Lewis acidity). This theory can be applied to the ORR processes as follows: the Li^+ ions generated during discharge are strong electrophils, i.e., hard Lewis acids due to their small ion radii and consequently large charge densities. Therefore, Li^+ will preferably react with the strong nucleophils O_2^{2-} and O^{2-} , which results in the generation of lithium peroxide (Li_2O_2) and lithium oxide (Li_2O). The desired LiO_2 intermediate, however, is formed with the weak nucleophil O_2^- . Hence, it is important to use an electrolyte solvent with *basic* properties to decrease the *acidity* of the Li^+ ions, e.g., by formation of $[Li^+(\text{solvent})_n]$ complexes. The decreased acidity of the Li^+ ions resulting from such a solvation increases the affinity to O_2^- and results in stabilized LiO_2 intermediates in the electrolyte. The Lewis basicity required for a suitable solvent is defined by the Gutmann (electron) donor number (DN). Laoire *et al.* investigated the effect of the DN of different electrolyte solvents on the reversibility of the ORR/OER potentials observed in CV measurements[10]. In short, it was concluded that the higher the DN of a solvent, the more readily Li^+ is solvated, i.e., the first reduction product LiO_2 is better stabilized by the solvent molecules. The stabilization of LiO_2 by electrolyte solvents, which are still used in current research[12,14,25,26], was reported to decrease in the order: dimethyl-

sulfoxide (DMSO, DN: 29.8) > acetonitrile (MeCN, DN: 14.1) > dimethyl ether (DME, DN: 20.0) > tetraethyleneglycol dimethylether (TEGDME, DN: 16.6)[10].

CV studies using MeCN as electrolyte solvent, on the other hand, showed Li_2O_2 formation without any detection of the LiO_2 intermediate[27–29]. Furthermore, the ORR potential was reported to be considerably lower in MeCN- compared to DMSO-based electrolytes[29].

However, the initially mentioned physical and chemical solvent properties have to be considered, too, e.g., a possible limitation of the cell capacity by high volatility, which is the case for DME. Despite this considerable disadvantage, studies using DME were and still are carried out under laboratory conditions, which is due to the solvent’s stability towards O_2^- radicals[11,30].

Regarding a low volatility, one class of materials should be mentioned, namely ionic liquids – and here especially the commonly used compound 1-butyl-1-methylpyrrolidinium bis(trifluoromethanesulfonyl)imide (BMPTFSI). Ionic liquids are of major interest for the Li/air system, as they exhibit low volatility, high thermal as well as (electro)chemical stability and low flammability[31–37]. Furthermore, their structures exhibit separated charges due to their salt-like character, i.e., negative charges in the anions and positive charges in cations, which leads to a good stabilization of the LiO_2 intermediate. A major drawback of ionic liquids, however, is the high viscosity, which limits the mobility of the solvated Li^+ ions in the electrolyte[38].

The electrolytes most commonly used for investigations concerning the Li/air system are based on the solvents TEGDME and DMSO.

2.3. Aprotic electrolyte solvents

TEGDME is a long-chain ether, which, besides its stability in the presence of Li metal, exhibits a low volatility due to its large molecular weight compared to the short-chain ether DME. Furthermore, TEGDME was reported to be stable against chemically generated LiO_2 [39]. In the same study, however, the polyvinylidene fluoride (PVdF) binder material of the carbon electrode was observed to decompose during cycling[39].

DMSO is the solvent, in which for the first time the superoxide radical O_2^- was found to be stable by Sawyer and Roberts[40]. Furthermore, it is widely regarded as suitable solvent for the use in Li/air battery investigations under laboratory conditions[27,41,42]. Subsequent to galvanostatic cycling in DMSO-based electrolytes several groups reported the presence of toroidally shaped Li_2O_2 particles, which were detected by scanning electron microscopy (SEM) and atomic force microscopy (AFM) on the surface of discharged electrodes[43,44]. A recent *in situ*-infrared (IR) study showed the electrochemical stability of a Li^+ /DMSO electrolyte at potentials as low as 1.9 V vs. Li/Li⁺ during CV measurements in the presence of O_2 [45]. Here, a decomposition of DMSO to DMSO_2 was reported only at potentials > 4.2 V vs. Li/Li⁺ during the charge reaction[45]. Further insight into the behavior of the different electrolyte solvents is given in section 4.2.1.

2.4. Electrochemical kinetics and catalysis

2.4.1. Electrochemical theory

The methods used in this study for the electrochemical investigations are linear sweep voltammetry (LSV) and cyclic voltammetry (CV). For both methods, a potential change is applied at a specific rate (scan rate ν) in one direction, and the electrochemical reactions are detected by a change of the current density signal. Hence, in case of a potential sweep in the cathodic (negative) direction (which is used for the observation of the ORR processes in this work), negative current densities are observed. For CV measurements the sweep is reversed at a potential at least 0.06 V below the peak potential E_{peak} to allow a detailed evaluation of the measurement (see Figure 2.3 on the next page)[46]. During the reversed sweep information about the anodic (OER) processes can be obtained, i.e., the oxidation of the products generated during the cathodic scan.

Important parameters for LSV and CV measurements are the onset and peak potentials, E_{onset} and E_{peak} , which indicate the start and the end of a kinetically controlled reaction, respectively (see Figure 2.3.b for an example of the cathodic reaction). The overpotentials η obtained during galvanostatic cycling (see Figure 2.2) are observed in CV measurements as the difference between the applied potential E , at which the reactions are observed, and the redox potential of reversible Li_2O_2 formation E^0 (see Figure 2.3.a). At potentials $< E_{\text{peak,ORR}}$ in the cathodic direction (and potentials $> E_{\text{peak,OER}}$ in the anodic direction), the kinetics of the ORR (and OER) processes are sufficiently fast. Here, the transport of the educts to the active electrode surface is the rate-determining process, which results in the observation of diffusion-limited current densities j_{lim} (see Figure 2.3.b).

2.4. Electrochemical kinetics and catalysis

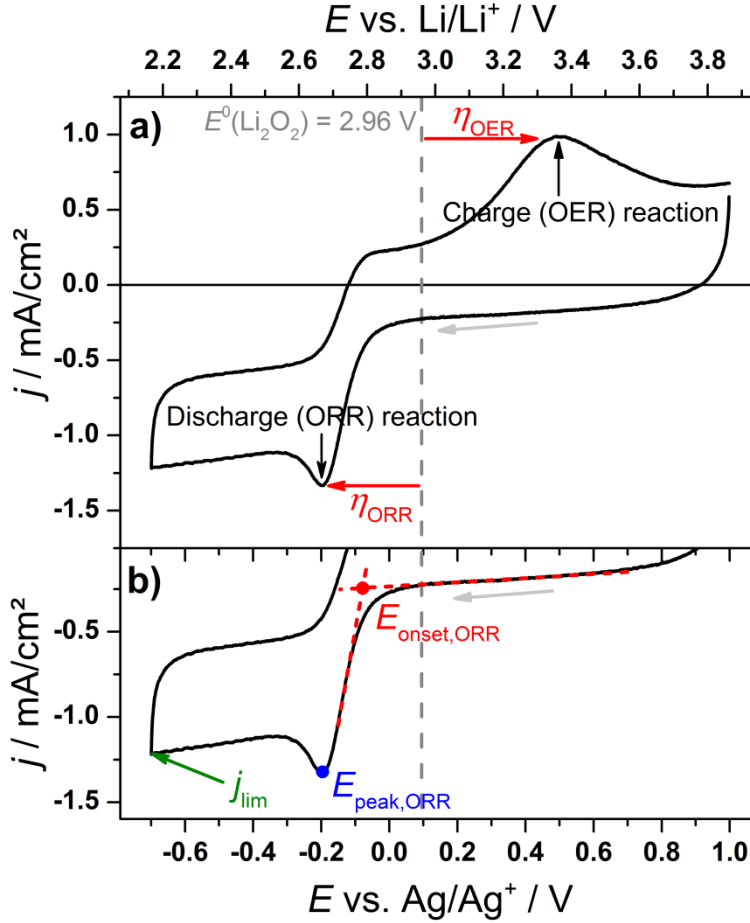


Figure 2.3: Example of (a) a CV measurement and (b) the cathodic (ORR) scan. Working electrode: Vulcan[®] carbon powder; electrolyte: 1 M Li⁺/DMSO; $\nu = 100$ mV/s; $\omega = 200$ rpm; the dashed grey line denotes the reversible Li₂O₂ formation potential E^0 vs. Li/Li⁺ = 2.96 V[7,8]; in (a) η_{ORR} and η_{OER} are the overpotentials with respect to E^0 , at which the ORR and OER reactions are observed during the cathodic and anodic scans, respectively; in (b) the parameters E_{onset} , E_{peak} and j_{lim} are shown (for definitions, see text).

The initial one-electron transfer resulting in the respective intermediate ORR product (see eqs. (2.1) and (2.6)) takes place at the start of the cathodic reaction, so that information about these reactions can be obtained at potentials close to E_{onset} .

For the kinetic investigation of the initial electron transfer the “cathodic quantity” αn [47] has to be determined, which consists of the charge transfer

coefficient α and the number of electrons transferred during the rate-determining step n . The value of α in the range from 0 ... 1 is defined as the relative change of the activation energy ΔG^\ddagger (which is needed to form the activated complex of an electrochemical reaction) resulting from a change of the applied overpotential η , i.e., $\alpha = d\Delta G^\ddagger / d\eta$.

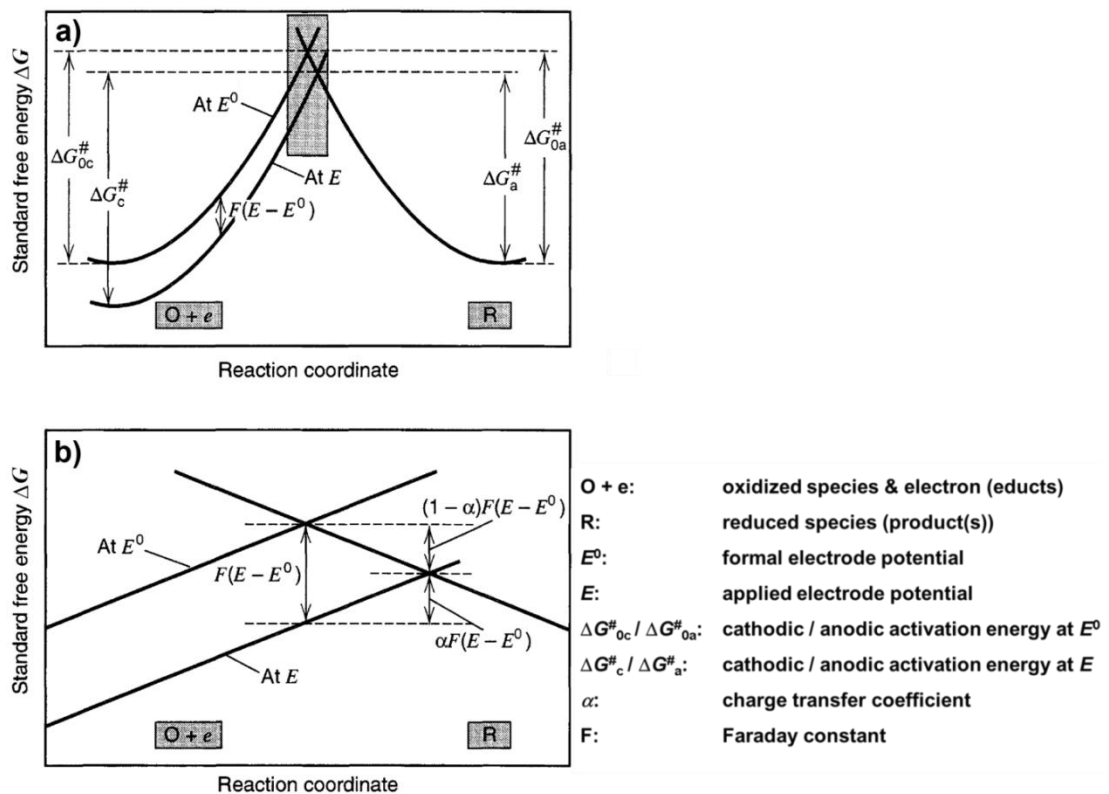


Figure 2.4: The influence of an applied overpotential on the activation energy barrier for an electrochemical reaction[48]. Cathodic direction on the reaction coordinate from left to right; (a) influence of an applied (positive) overpotential $\eta = E - E^0$ on the standard free energy ΔG of the educts ($O + e$) and the activation energy ΔG_{oc}^\ddagger needed for the reaction to the product (R); (b) detailed view of the potential curve intersections for E^0 and an applied potential E , showing the standard free energies ΔG of the activated complexes for the respective potentials and the meaning of the charge transfer coefficient α .

2.4. Electrochemical kinetics and catalysis

Figure 2.4 (see previous page) depicts the influence of the applied potential E on the standard free energies ΔG of the reactants ($O + e$), the activated complex (the potential curve intersections in Figure 2.4.b) and the product (R). The increase of the cathodic activation energy barrier by the application of a positive overpotential $\eta = (E - E^0)$ is shown in Figure 2.4, i.e., the application of a negative overpotential results in a decrease of the cathodic activation energy by:

$$\Delta G_c^\# = \Delta G_{0c}^\# + \alpha n \cdot F \cdot \eta \quad (2.8)$$

with the activation energy for the formation of the activated complex in the cathodic direction $\Delta G_{0c}^\#$, the activation energy for the formation of the activated complex in the cathodic direction at the applied overpotential $\Delta G_c^\#$, the Faraday constant F and the number of electrons transferred during the reaction n . As this equation is only applicable for a one-electron transfer ($n = 1$)[48,49], the charge transfer coefficients α for the reaction intermediates of eqs. (2.1) and (2.6) can be determined at low overpotentials immediately after the start of the reaction, i.e., close to the onset potential E_{onset} . Therefore, the cathodic part of the Butler-Volmer equation, which describes the dependence of the obtained negative current densities j on the negative overpotential η , can be applied for the ORR processes:

$$j = -j_0 \cdot \exp\left(-\frac{\alpha n \cdot F}{R \cdot T} \eta\right) \quad (2.9)$$

with the molar gas constant R , the temperature T and the partial current density for the cathodic (ORR) processes j_0 , which is a direct descriptor for the kinetic activity of an electrode surface. j_0 and α can be obtained by plotting α vs. $\ln|j|$ in so-called Tafel plots. These show linearity in the overpotential region of -0.05 V to -0.30 V, depending on the electrode material. An example is given in Figure 2.5 (see next page).

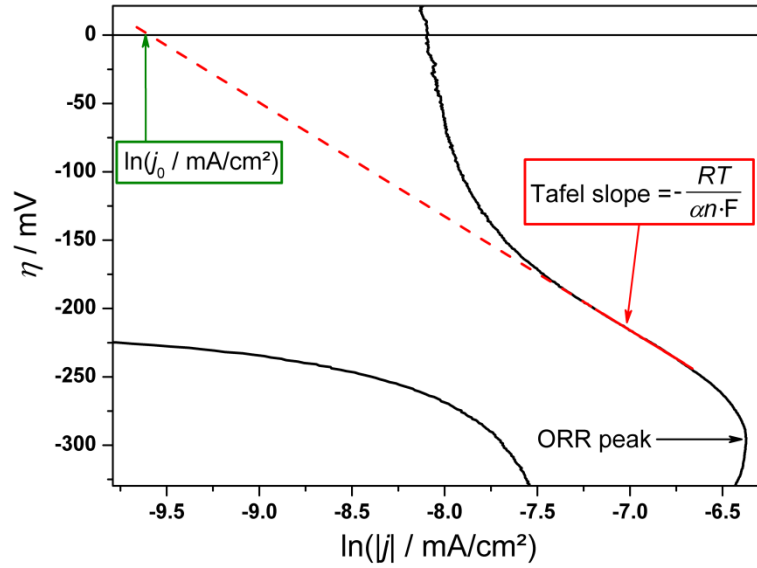


Figure 2.5: Example of a Tafel plot of the ORR region observed during a CV measurement. The dashed red line indicates the fit of the linear Tafel region, from which the intercept at $\eta = 0$ V (green box) and the Tafel slope (red box) can be obtained.

The reciprocal value of the exponential term in eq. (2.9) equals the Tafel slope, from which the value of α can be determined (see also red box in Figure 2.5):

$$\frac{d\eta}{d\ln|j|} = -\frac{R \cdot T}{\alpha n \cdot F} \quad (2.10)$$

It has to be pointed out again, that the Butler-Volmer equation is only applicable for one-electron transfers, although two-electron transfers are expected during the reduction of O_2 to Li_2O_2 . These, however, will not take place in single steps, which is highly improbable due to a large activation energy barrier for simultaneous two-electron transfers[50,51]. Two or more consecutive one-electron transfers, on the other hand, can be indirectly deduced from the Tafel plots, if improbably low Tafel slopes are obtained[47,49,52]: rate-determining one-electron transfers without any preceding steps result in a Tafel slope of about 118 mV/dec, whereas Tafel slopes < 118 mV/dec indicate electron transfers preceding the rate-

2.4. Electrochemical kinetics and catalysis

determining reduction step[49,53,54]. Tafel slopes > 118 mV/dec are attributed to either (i) a preceding chemical dissociation or (ii) a subsequent chemical combination as well as (iii) an electrode transfer through an oxide layer[49]. In order to avoid confusion, the values obtained from the Tafel slopes will be referred to as “cathodic quantities” αn in the following sections, as these will directly be used for the investigation of the ORR mechanisms.

Furthermore, information about the kinetic activity of an electrode material can be obtained from the Tafel plots. The intercept of the linear fit of the Tafel slope with $\eta = 0$ V gives the value of $\ln j_0$, from which the partial current density j_0 is obtained (see green box in Figure 2.5). From j_0 – dependent only on the activity of the electrode material under otherwise similar reaction conditions – the apparent reaction rate constant k_{app}^0 for the reduction reaction can be determined by:

$$j_0 = n \cdot F \cdot C_{\text{O}_2} \cdot k_{\text{app}}^0 \quad (2.11)$$

with the oxygen concentration in the electrolyte C_{O_2} (in aprotic media usually the solubility of O_2 in the respective solvent is used[9,10,55]).

The dependence of the current density on the scan rate, which was found by Randles and Ševčík, provides insight into the rate limitation of electrochemical mechanisms[56,57]. As the Randles/Ševčík relationship is only applicable for reversible processes, the ORR processes investigated in this work have to be evaluated with the semi-empirical relationship for quasi- and irreversible reactions reported by Nicholson and Shain[58]. This is based on the Randles/Ševčík relationship and makes use of the cathodic quantities obtained from the Tafel slopes:

$$j_{\text{peak}} = 2.69 \cdot 10^5 \cdot C_{\text{O}_2} \cdot \sqrt{(\alpha n) \cdot \nu \cdot D_{\text{O}_2} \cdot n^*} \quad (2.12)$$

with the cathodic peak current density j_{peak} , the diffusion coefficient of O_2 in the electrolyte D_{O_2} and the descriptor for the rate limitation of the reaction

n^* [47,48,59]. As the peak current density j_{peak} is defined as the end of the kinetically controlled and hence the start of the diffusion-limited reaction, a linear relationship of $\frac{dj_{\text{peak}}}{d\sqrt{v}} = 1 = n^*$ indicates diffusion control of the ORR processes, whereas $n^* = 2$ points to diffusionless processes and/or preceding chemical reactions[60]. Therefore, the rate limitation of the ORR processes is described by the n^* values obtained from eq. (2.12)[9,10,27,59].

2.4.2. Catalysts for the Li/air system

As already mentioned in section 2.2, research on appropriate ORR/OER catalysts focuses on materials with low oxygen adsorption enthalpies to avoid a dissociative O_2 adsorption and the generation of highly reactive O_{ads} species, which are formed in the presence of noble metals, such as Ir, Ru, Pd, and Pt[19–23,61–65]. Here, transition metals (e.g., Mn, Fe, Co and Ni) are considered as interesting alternatives[66]. Many of these elements show multiple stable valences resulting in a large number of oxides, whose general advantages include high abundance and low cost (see Figure 2.6 on the next page).

Several perovskite and transition metal oxide catalysts, such as LaBO_3 ($\text{B} = \text{Ni}, \text{Fe}, \text{Mn}, \text{Cr}$), Zr/CeO_x , RuO_2 , Co_3O_4 , CaMnO_3 and MnO_2 , have been reported to show electrocatalytic activities comparable those of noble metals in aqueous and ether-based electrolytes[68–75]. Furthermore, recent X-ray absorption spectroscopy (XAS) and *in situ*-infrared (IR) spectroscopy studies suggested, that the presence of different oxidation states of transition metals, e.g., Cr^{2+} and Ir^{2+} in Cr , Cr_2O_3 and LaCrO_3 as well as IrO_2 catalysts increases the catalytic activities for the OER process in ether-based and aqueous electrolytes, respectively[68,76]. Several reports, on the other hand, raise

2.4. Electrochemical kinetics and catalysis

doubt about the need of electrocatalysts in the Li/air system – especially regarding the ORR processes[20,77]. McCloskey *et al.* observed the decomposition of a DME-based electrolyte to proceed during discharge of a Li/air cell in the presence of Au, Pt and MnO_2 catalysts rather than ORR processes[20].

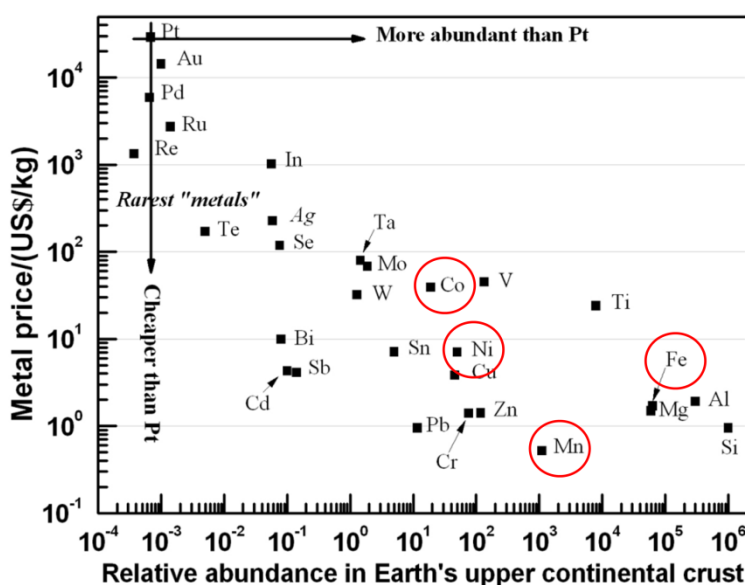


Figure 2.6: Metal prices and abundance (relative to Si abundance) of the chemical elements in Earth's upper continental crust[67]. The metal price data were taken from www.metalprices.com on September 2, 2005.

In order to clarify the different results on the impact of catalysts for the Li/air system, this work investigates the catalytic ORR activities of different Mn_xO_y compounds, as this class of materials has been shown to exhibit interesting catalytic properties in the Li/air system[17,78–80]. The results presented in these studies, however, were obtained with instable electrolytes, i.e., electrolyte decomposition was observed rather than ORR/OER processes. Therefore, a re-evaluation of the ORR activities of Mn_xO_y catalysts in a stable electrolyte is carried out in this work.

2.4.3. Manganese oxides

Manganese oxides exist in various morphologies, which contain Mn^{z+} ions of different valence states, e.g., Mn^{II} , Mn^{III} and Mn^{IV} , corresponding to stable Mn_xO_y compounds, such as MnO , Mn_3O_4 , Mn_2O_3 and MnO_2 [81]. Many Mn_xO_y phases consist of tunnel structures built from MnO_6 octahedra. These structures provide several advantages, e.g., an easier access of reactants to the active reaction sites (provided by the tunnels) and a better electron transport in the oxide structure (due to the presence of $\text{metal}[\text{O}]_6$ octahedra). The latter point has been shown to be of advantage for the ORR/OER activities of pyrochlore catalysts (which exhibit RuO_6 octahedra) in aqueous and ether-based systems[82–85].

Furthermore, oxygen vacancies in Mn_xO_y structures with could result in an increase of the catalytic activities for reduction and oxidation reactions, as a non-stoichiometric amount of lattice oxygen results in variable oxidation states of metal cations within the oxide structure[87]. Here, an especially interesting species is Mn_3O_4 , as it has the same space group as the anatase structure of TiO_2 ($I4_1/amd$)[86]. TiO_2 is known to be a highly active catalyst and support material for several gas phase reactions due to surface $\text{Ti}^{4+}/\text{Ti}^{3+}$ redox centers and oxygen vacancies inside the structure[87–91].

These properties (different Mn^{z+} oxidation states, MnO_6 octahedra and a possible presence of oxygen vacancies) led to an increased interest in Mn_xO_y compounds for applications as ORR/OER catalysts in Li/air systems[78,80,92,93].

Additionally, the advantages of manganese oxides can be enhanced by nanostructuring, which has been shown in recent studies focusing on the various morphologies of MnO_2 . These compounds were found to be active ORR/OER catalysts in pure form as well as in combination with graphene

2.4. Electrochemical kinetics and catalysis

and different noble metals in aqueous and aprotic electrolytes[94–100]. Other nanostructured Mn_xO_y species have been widely synthesized as, e.g., mesoporous crystals, nanoparticles, nanodiscs and nanorods[101–105]. Up to now, however, their catalytic ORR/OER activities have mostly been investigated in aqueous systems.

A useful method to synthesize nanoscale Mn_xO_y compounds is the calcination process, for which a suitable precursor material is needed[106–109]. Whereas there exist many synthetic routes yielding Mn_xO_y particles on a nanometer scale[110], e.g., precipitation and solvothermal syntheses, these methods require long reaction times up to 24 h and subsequent drying procedures of up to 2 days[103,111–115]. A synthesis *via* oxidation of manganese metal nanoparticles by gas condensation has to be followed by annealing in O_2 -containing atmospheres in order to obtain different Mn_xO_y species[116].

Here, the calcination route studied within this work is an advantageous alternative, because the morphology as well as the size of the precursor material are conserved during the oxidation process. This is of special interest, when nanoscale precursor particles are used. Furthermore, a calcination in the absence of O_2 , e.g., in inert Ar atmosphere, can prevent the complete oxidation of the resulting Mn_xO_y , so that the lattice oxygen density is decreased, which can result in a certain amount of oxygen vacancies. Further advantages of this process include a relatively short synthesis time of about 1 h to 5 h and the fact that one precursor material can be used to obtain several different products by a variation of the calcination conditions, such as temperature, time and gas atmosphere. Even more, pure-phase Mn_5O_8 (whose catalytic ORR activity in aprotic media is investigated for the first time in this work) has up to now only been reported to be obtained by calcination processes[116–121].

3. Experimental part

3.1. *Materials***Table 3.1:** Chemicals used for Mn(II) glycolate synthesis; gases used for calcination and TGA/DSC as well as electrochemical measurements.*

	<i>Abbreviation</i>	<i>Purity</i>	<i>Company</i>
Manganese(II) acetate tetrahydrate	MnAc ₂	> 99%, pure	Carl-Roth
Ethylene glycol	EG	> 99.5%, p.a.	
Tetraethyleneglycol	TEG	99%	Sigma-Aldrich
Argon	Ar	5.0	Linde
Oxygen	O ₂	6.0	

*All chemicals were used without further purification.

Table 3.2: Chemicals used for electrode preparation and electrochemical measurements.*

	<i>Abbreviation</i>	<i>Purity</i>	<i>Company</i>
Ethanol	EtOH	analytical reagent-grade	Fisher Scientific
Vulcan[®] XC72R carbon	VC	n.a.	Cabot
Lithium bis(trifluoromethylsulfonyl)imide	LiTFSI	reagent-grade	Merck KGaA
Acetonitrile	MeCN	≥ 99.9%	
10wt% Nafion[®]/water	-	n.a.	
Dimethyl-sulfoxide	DMSO	anhydrous, ≥ 99.9%	Sigma Aldrich
Tetraethyleneglycol dimethylether	TEGDME	99%	
1-Butyl-1-methylpyrrolidinium bis(trifluoromethylsulfonyl)imide	BMPTFSI	99%	io-li-tec

*All chemicals were used without further purification.

3.2. Manganese oxide synthesis

3.2. Manganese oxide synthesis

3.2.1. Mixed-phase manganese oxide particles

The synthesis of Mn(II) glycolate was done by a polyol process reported by Liu *et al.*[108]. In short, 5 mg manganese(II) acetate tetrahydrate (MnAc_2) were dissolved in 50 mL ethyleneglycol (EG) and 5 mL tetraethyleneglycol (TEG). The solution was stirred and simultaneously heated up to 200°C with a heating rate of about 6 K/min. During heating the solution turned brown at a temperature of about 115°C. After about 15 min of constant heating at 200°C a white precipitate appeared, indicating the formation of the precursor particles. Following further 35 min of stirring at 200°C the product was cooled down to room temperature. The white solid was centrifuged and re-dispersed in ethanol several times to remove any remaining impurities. Subsequently, the product was dried at room temperature for 2 h in an Ar flow.

The obtained precursor was calcined at 400°C for 2 h in an O_2 flow of 50 NL/h to obtain crystalline $\text{Mn}_3\text{O}_4/\text{Mn}_5\text{O}_8$ particles.

3.2.2. Pure-phase manganese oxide particles

The synthesis of the Mn(II) glycolate precursor was modified by a decrease of the synthesis temperature and an increase of the heating rate in order to obtain smaller precursor particles for the calcination to nanostructured manganese oxides (Mn_xO_y).

In a typical reaction, 1 mmol (0.246 g) manganese(II) acetate tetrahydrate (MnAc_2) was mixed with 3 mmol (3 mL) tetraethyleneglycol (TEG) and added to 30 mL ethyleneglycol (EG) in a three-neck round-bottom flask. The

stirred solution was heated up to 170°C with a heating rate of about 7.5 K/min. Upon heating, the solution started to turn brown at a temperature of about 110°C, and after further heating for about 1 h at 170°C a white precipitate appeared, which disappeared again after 1 h (for an XRD analysis of the intermediate product, see Figure 4.4). The solution was stirred for another 4 h at 170°C until a white precipitate appeared again, which indicated the formation of the Mn(II) glycolate particles. The product was stirred for another hour at 170°C to complete the reaction and subsequently cooled down to room temperature. The white powder was centrifuged and washed at least five times with ethanol to remove any impurities. Subsequently, the white product was dried at room temperature for 2 h in an Ar flow.

The obtained Mn(II) glycolate powder was calcined at 350°C and at 550°C for 2 h in an Ar flow of 50 NL/h to yield Mn₃O₄ nanoparticles and mesoporous α -Mn₂O₃ particles, respectively. Nanoparticles of Mn₅O₈ were obtained by precursor calcination at 400°C for 5 h in an O₂ flow of 50 NL/h.

3.3. Morphological and structural analysis

3.3.1. Electron microscopy

The sizes and morphologies of the precursor as well as Mn_xO_y particles were characterized by transmission electron microscopy (TEM) using a Tecnai G2 microscope with an acceleration voltage of 200 kV and a Zeiss EM 902A microscope with an acceleration voltage of 80 kV. The samples for TEM measurements were prepared by depositing a drop of an ethanol dispersion of the powder on a carbon-coated copper grid and drying at room temperature.

3.3. Morphological and structural analysis

Scanning electron microscopy (SEM) was carried out with an Oxford INCA system employing a PentaFET Precision INCA X-act detector integrated into the Hitachi S-3200N microscope. The sample was prepared by depositing an ethanol dispersion of the sample onto an Al substrate and drying at room temperature.

3.3.2. X-ray diffraction (XRD) and *in situ*-XRD

For X-ray diffraction (XRD), a PANalytical X'Pert Pro MPD diffractometer was used operating with Cu K_α radiation (wavelength $\lambda_{\text{Cu}} = 0.15418$ nm), Bragg-Brentano θ - 2θ geometry and a goniometer radius of 240 mm. Samples for XRD measurements were prepared by placing the powder onto low-background silicon sample holders. The XRD measurements were conducted in ambient atmosphere. The crystallite sizes $d_{\text{crystallite}}$ of the samples were calculated from all assigned reflections with the Scherrer equation:

$$d_{\text{crystallite}} = \frac{K \cdot \lambda_{\text{Cu}}}{B \cdot \cos\theta} \quad (3.1)$$

with the Bragg angle θ and the dimensionless Scherrer constant K , which is dependent on the particle shape. For rectangular and spherical particles values of $K = 0.83$ and $K = 1.20$ were used, respectively[122]. B is the broadening of the reflection at half the maximum intensity (**full width at half maximum**, FWHM) in radians after subtracting the instrumental reflection broadening B_i :

$$B = \sqrt{\text{FWHM}^2 - B_i^2} \quad (3.2)$$

The instrumental reflection broadening of the employed diffractometer B_i was determined on the basis of the Caglioti/Paoletti/Ricci model[123,124] by other members of the group as given by:

$$B_i = \sqrt{-0.005260679 \cdot \tan^2\theta + 0.012269341 \cdot \tan\theta + 0.018837553} \quad (3.3)$$

The lattice constants were obtained from assigned diffraction reflections with the Bragg equation, as given in eqs. (3.4)-(3.8):

$$n\lambda_{\text{Cu}} = 2d \cdot \sin\theta \quad (3.4)$$

with an integer n and the interplanar distance of the lattice planes, at which the X-rays are scattered, d . The lattice constants (a , b , c) of the different compounds were calculated with the following equations for the respective compound structures (space groups):

$$d = \sqrt[3]{\frac{4}{3} \cdot \left(\frac{h^2+hk+k^2}{a^2}\right) + \frac{l^2}{c^2}} \quad (3.5)$$

for the trigonal structure of Mn(II) glycolate ($P\bar{3}m1$),

$$d = \sqrt{\frac{h^2+k^2}{a^2} + \frac{l^2}{c^2}} \quad (3.6)$$

for the tetragonal structure of Mn_3O_4 ($I4_1/amd$),

$$d = \sqrt{\left(\frac{h^2}{a^2} + \frac{l^2}{c^2} - \frac{2 \cdot hl \cdot \cos\beta}{a \cdot c}\right)^{-1} \cdot \sin\beta + \frac{k^2}{b^2}} \quad (3.7)$$

for the monoclinic structure of Mn_5O_8 ($C2/m$), and

$$d = \sqrt{\frac{h^2+k^2+l^2}{a^2}} \quad (3.8)$$

for the cubic structure of $\alpha\text{-Mn}_2\text{O}_3$ ($Ia\bar{3}$).

In situ-XRD measurements were carried out with the same experimental setup using a high temperature chamber from Anton Paar (HTK 1200N). The temperature profile measurements were recorded in an O_2 flow during the heating of the powder sample from 25°C to 700°C with a heating rate of

3.3. Morphological and structural analysis

2 K/min. The time profile measurements were conducted during constant heating of the powder sample at 400°C for 350 min in an O₂ flow, which had previously been heated from 25°C to 400°C with a heating rate of 18 K/min in an O₂ flow. For these experiments the powder samples were placed on a corundum sample holder. The thermal expansion was corrected automatically during the measurements.

3.3.3. Thermogravimetric analysis (TGA) and differential scanning calorimetry (DSC)

Thermogravimetric analysis (TGA) and differential scanning calorimetry (DSC) were carried out with a Netzsch STA 449 F3 Jupiter thermo-analysis system. The samples were deposited in Al₂O₃ crucibles and heated from 35°C to 700°C with a heating rate of 2 K/min in an O₂/Ar (1:2) and an Ar gas flow of 40 NmL/min, respectively.

3.3.4. N₂ adsorption-desorption

The porosity of the Mn_xO_y powders was determined by N₂ adsorption-desorption measurements. Prior to the measurement, the material was kept under vacuum at 180°C for 18 h to remove any residual gas and moisture from the sample. The adsorption-desorption isotherms were measured with a Quantachrome Nova 2000E at 77 K. The Brunauer-Emmet-Teller (BET) method was used to determine the complete inner surfaces and the Barrett-Joyner-Halenda (BJH) method for the mesopore surface analysis as well as for the determination of the pore size distributions.

3.4. Electrochemical analysis of the catalytic activity

3.4.1. Electrode preparation

The catalyst/carbon ink for the powder electrodes was prepared by mixing and grinding 90 mg Vulcan[®] XC72R carbon powder (VC) with 10 mg of the respective Mn_xO_y powder. 14.4 mg of this active material was dispersed in 2.5 mL ethanol and ultrasonicated for 20 min. As binder material, 0.5 mL of a 0.1wt.% Nafion[®]/water solution were added to 2.5 mL of the catalyst/carbon dispersion and ultrasonicated for another 20 min. Subsequently, a 10 µl drop of the ink was applied on a glassy carbon (GC) disc and dried at 80°C for 12 h. The 10wt.% catalyst loading of the prepared Mn_xO_y/C electrodes equals 4.8 µg per electrode and 24.4 µg/cm².

3.4.2. Electrochemical measurements

For electrochemical measurements Reference 600 and Reference 3000 (Gamry Instruments) potentiostats were used. The measurements were carried out with a rotating disc electrode (RDE) setup in a glove box with Ar atmosphere at ambient temperature (see Figure 3.1 on the next page).

For the electrochemical setup GC discs ($d = 0.5$ cm, Pine Research Instrumentation, electrode model no. AFE3T050GC) and VC-coated GC discs as well as 10% Mn_xO_y/C-coated GC discs served as working electrodes (WE). Polished Ag wires and Pt discs were used as reference electrodes (RE) and counter electrodes (CE), respectively.

3.4. Electrochemical analysis of the catalytic activity

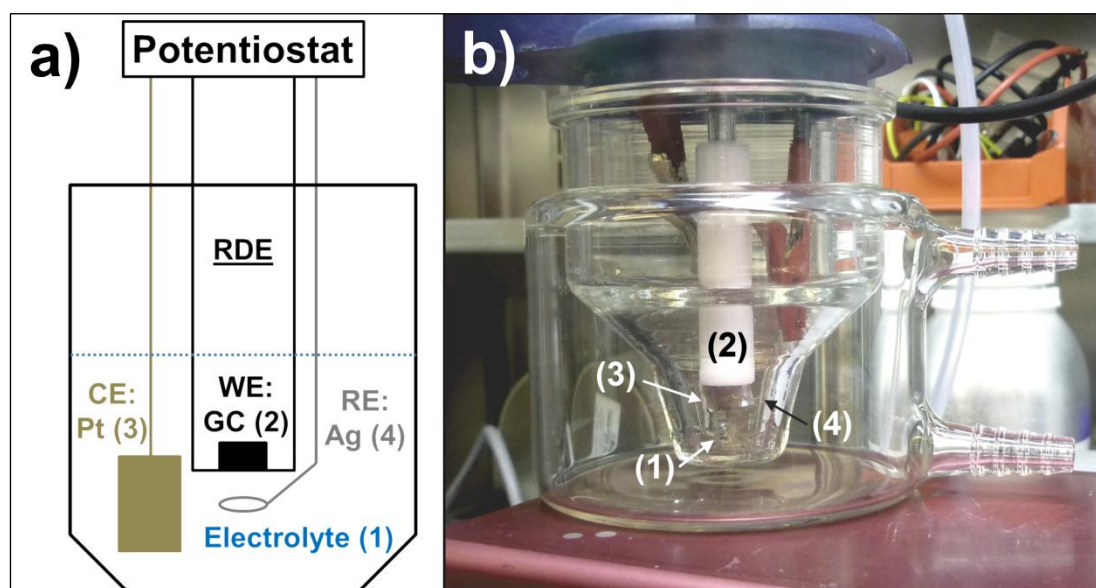


Figure 3.1: (a) Schematic representation and (b) photo of the setup in the Ar-filled glove box. (1) Glass container with the electrolyte, (2) WE: the RDE finger with the working electrode (GC disc), (3) CE: the counter electrode (Pt disc), and (4) RE: the reference electrode (Ag wire).

The investigation of the various electrolytes were carried out with 1 M LiTFSI solutions of MeCN, TEGDME, BMPTFSI, DMSO and a solvent mixture of BMPTFSI/DMSO (1:100). All other electrochemical measurements were conducted with 1 M LiTFSI/DMSO as electrolyte.

For all electrochemical experiments an amount of 5 mL electrolyte was used, which was saturated with Ar or O₂ for 25 min prior to the start of the measurement.

The linear sweep voltammetry (LSV) and cyclic voltammetry (CV) measurements were recorded at potentials within the range of -1 V vs. Ag/Ag⁺ in the cathodic direction to 1.1 V vs. Ag/Ag⁺ in the anodic direction. The experiments were conducted at scan rates in the range of 1 mV/s to 1000 mV/s with rotational frequencies of 0 rpm, 200 rpm and 1000 rpm. The parameters used for the different investigations are given in sections 4.2 to 4.4 for the respective experiments. All data, which are subject

to discussion in these sections, were obtained from the voltammetry measurements after subtracting the capacitive currents obtained in Ar-saturated electrolyte for the respective electrode materials.

Each electrochemical measurement was carried out with a newly prepared electrode and repeated at least five times. All data calculated from electrochemical measurements are given as mean values in this work, as electrochemical data obtained with non-noble materials are known to show significant deviations in different measurements[125].

3. Experimental part

4. Results & Discussion

4.1. Synthesis and characterization of the manganese oxides

In order to obtain different nanostructured Mn_xO_y compounds by calcination, suitable precursor nanoparticles were synthesized. Here, polyol processes provide access to a wide range of particle diameters and morphologies by several adjustable synthesis parameters, e.g., reaction time and temperature, which has already been shown for Mn-Fe, Co and Mn alkoxides[117,126]. Therefore, a polyol process reported by Liu *et al.* was used to generate Mn(II) glycolate precursor particles[108]. This section contains results already published elsewhere[105,127].

4.1.1. Mixed-phase manganese oxides

4.1.1.1. *Mn(II) glycolate precursor by polyol synthesis*

The Mn(II) glycolate particles synthesized in ethylene glycol at 200°C for 50 min were obtained as a white powder, which was characterized by XRD and TEM analysis.

Figure 4.1.a (see next page) depicts the XRD pattern of the obtained product. The low-angle reflections at $2\theta \approx 11^\circ$ and $2\theta \approx 22^\circ$ (see red lines in Figure 4.1.a) are typical for the trigonal brucite-type structure of Mn(II) glycolate (space group $P\bar{3}m1$) and were also observed by Liu *et al.*[108].

The TEM image in Figure 4.1.b depicts the Mn(II) glycolate particles, of which the majority shows circular shapes with diameters in the range of 40 nm to 80 nm (examples are highlighted blue in Figure 4.1.b).

4.1.1. Mixed-phase manganese oxides

Furthermore, elongated particles with nanorod-like shapes and diameters between 20 nm and 30 nm as well as lengths between 100 nm and 180 nm are visible in the TEM image (examples are highlighted green in Figure 4.1.b).

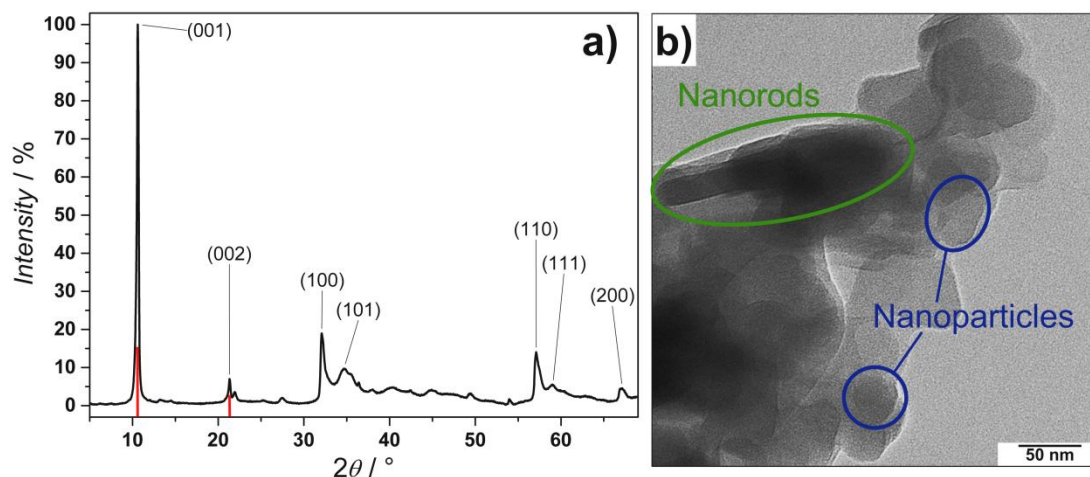


Figure 4.1:(a) XRD pattern and (b) TEM image of the Mn(II) glycolate particles after synthesis at 200°C for 50 min. Red lines in (a) denote reflections previously reported by Liu *et al.*[108]; the reflections in (a) are assigned according to data from the literature[128].

The particles observed in Figure 4.1.b are by more than one order of magnitude smaller compared to those of the Mn(II) glycolate precursor obtained by Liu *et al.*[108]. As no detailed information about the heating conditions during the precursor synthesis was given by Liu *et al.*, a possible explanation for the smaller particle sizes obtained here might be a larger heating rate. As Liu *et al.* reported the formation of Mn_2O_3 particles in the μm range by precursor calcination[108], the smaller Mn(II) glycolate nanoparticles obtained here are considered promising precursors for the generation of Mn_xO_y compounds in the *nm* range.

4.1.1.2. *Mixed-phase Mn₃O₄/Mn₅O₈ by calcination*

The precursor nanoparticles were calcined in O₂ atmosphere at 400°C for 2 h to yield Mn_xO_y particles, which were characterized by XRD and TEM analysis.

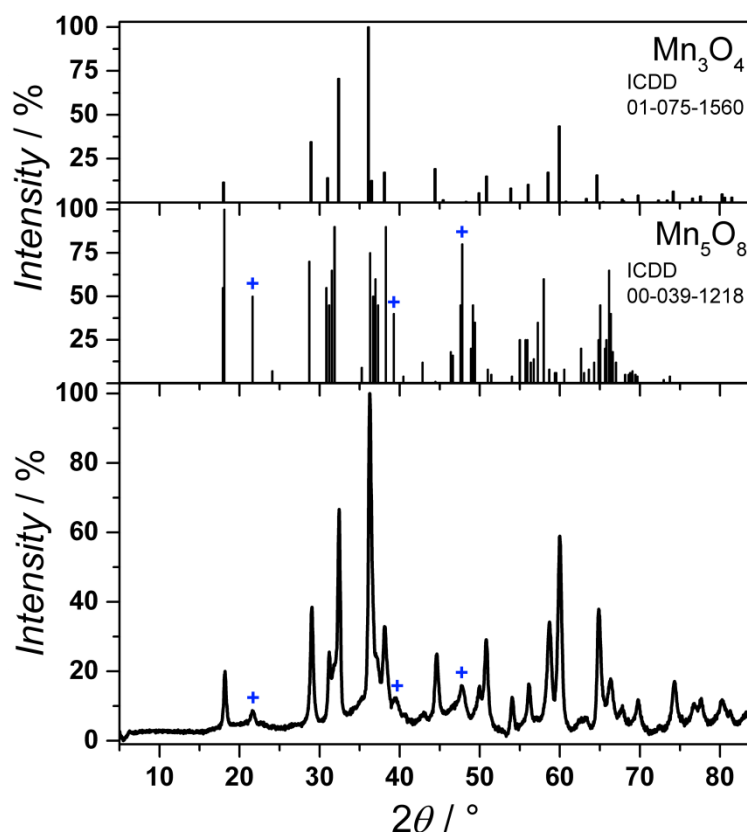


Figure 4.2: XRD pattern of the mixed-phase Mn_xO_y product obtained after calcination at 400°C for 2 h in O₂ atmosphere. The literature patterns of Mn₃O₄ and Mn₅O₈, which are present in the product, are depicted at the top; blue crosses (+) denote reflections confirming the presence of Mn₅O₈.

Figure 4.2 (bottom) depicts the X-ray diffractogram of the product obtained after calcination at 400°C for 2 h in O₂ atmosphere. The literature XRD patterns of Mn₃O₄ and Mn₅O₈ show that the obtained Mn_xO_y product consists of these two compounds (see Figure 4.2). Here, the phase of Mn₅O₈ is

4.1.1. Mixed-phase manganese oxides

only detected by the comparably low intensities of the reflections at 21.7° , 39° and 47° (see blue crosses in Figure 4.2). An explanation for the obtained phase mixture might be (i) the complete oxidation of the Mn(II) glycolate precursor to Mn_3O_4 with (ii) a subsequent incomplete oxidation of Mn_3O_4 to Mn_5O_8 . Feitknecht proposed the oxidation to Mn_5O_8 to proceed *via* a two-phase seed growth mechanism[118]. This is an oxidation process, which starts at the Mn_3O_4 particle edges and proceeds along the $\text{Mn}_3\text{O}_4/\text{Mn}_5\text{O}_8$ phase boundary, until the Mn_3O_4 phase is completely oxidized. The low intensities of the Mn_5O_8 reflections hence could derive from an incomplete particle oxidation due to the short calcination time. The time-dependence of this oxidation process is investigated with *in situ*-XRD measurements in section 4.1.2.4.

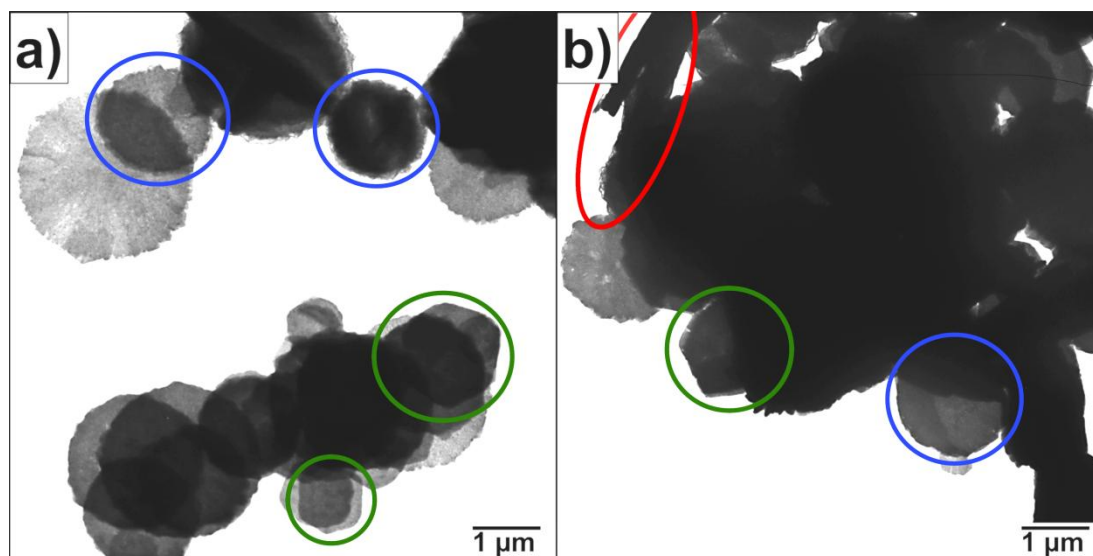


Figure 4.3: TEM images of the $\text{Mn}_3\text{O}_4/\text{Mn}_5\text{O}_8$ particles. Highlighted areas: examples for nanorods (red), circular (blue) and hexagonally shaped particles (green).

Figure 4.3 depicts TEM images of the $\text{Mn}_3\text{O}_4/\text{Mn}_5\text{O}_8$ particles, which exhibit plate-like (highlighted green and blue) and to some extent rod-like structures (highlighted red). Some of the plate-like particles have hexagonal shapes (highlighted green), but mostly circular plates were obtained

(highlighted blue). Most of the particles in both TEM images have diameters and/or lengths in the μm range. Hence, the desired generation of Mn_xO_y nanoparticles by calcination of the nanosized Mn(II) glycolate precursor was not achieved. However, the different particle morphologies of the precursor material (e.g., circular and rod-like shapes) are still observed in the oxide product.

As an influence of the heating conditions during the Mn(II) glycolate synthesis on the precursor particle diameters was suggested in the previous section, a modification of the polyol process is presented in the next section. Furthermore, the subsequent calcination of the Mn(II) glycolate particles yielding different Mn_xO_y compounds is discussed in combination with an extensive study on the influence of different calcination temperatures and gas atmospheres on the obtained products.

4.1.2. Nanostructured pure-phase manganese oxides

The polyol synthesis of the Mn(II) glycolate precursor presented in section 4.1.1.1 was modified in order to obtain smaller precursor particles. For the modified procedure the reaction temperature was decreased from 200°C to 170°C by a simultaneous increase of the heating rate from 6 K/min to 7.5 K/min.

Subsequent to the characterization of the Mn(II) glycolate particles in this section, the formation of several Mn_xO_y species by precursor calcination at different temperatures and in different atmospheres is discussed in order to obtain information about Mn_xO_y phase formations and transformations. Furthermore, this section presents an investigation of the structural and

4.1.2. Nanostructured pure-phase manganese oxides

morphological properties of the pure-phase Mn_xO_y compounds, which are investigated as ORR electrocatalysts in section 4.3.

4.1.2.1. *Mn(II) glycolate precursor by a modified polyol synthesis*

The polyol process reported by Liu *et al.* was modified to yield suitable Mn(II) glycolate precursor particles for the thermal decomposition to nanostructured Mn_xO_y by calcination[108].

After constant heating at 170°C for 1 h a white precipitate appeared. This product was identified by X-ray diffraction as Mn(II) glycolate containing large impurities of the dehydrated educt (Mn(II) acetate dihydrate) and the side product manganese oxalate (MnC_2O_4 , see Figure 4.4.a on the next page). In order to obtain the pure Mn(II) glycolate precursor, constant heating was continued at 170°C until a white precipitate appeared again. The XRD pattern of the product obtained after 7 h is depicted in Figure 4.4.b (see next page), which can be assigned to the trigonal brucite-type structure ($P\bar{3}m1$) of Mn(II) glycolate[108,117,128]. A mean Scherrer crystallite size of $17 \text{ nm} \pm 8 \text{ nm}$ was calculated for the Mn(II) glycolate particles (eq. (3.1)). Inorganic compounds with the same (brucite-type) crystal structure, such as $\text{Mg}(\text{OH})_2$, $\text{Co}(\text{OH})_2$, $\text{Ca}(\text{OH})_2$ and $\text{Ni}(\text{OH})_2$, exhibit lattice constants $a = 3.1 \text{ \AA} \dots 3.6 \text{ \AA}$ and $c = 4.6 \text{ \AA} \dots 4.9 \text{ \AA}$. For the Mn(II) glycolate presented here, the Mn-Mn distance (corresponding to lattice constant a) was calculated to be 3.2 \AA from the (110) reflection (eq. (3.5)), which is in good agreement with the findings of Sun *et al.*[128]. The interlayer distance along the [001] direction is 8.2 \AA (eq. (3.5)). This value corresponds to the lattice constant c and is consistent with literature studies, which reported lattice constants of $c = 8.3 \text{ \AA}$ and $c = 8.27 \text{ \AA}$ for Mn glycolate and Co glycolate, respectively[128,129].

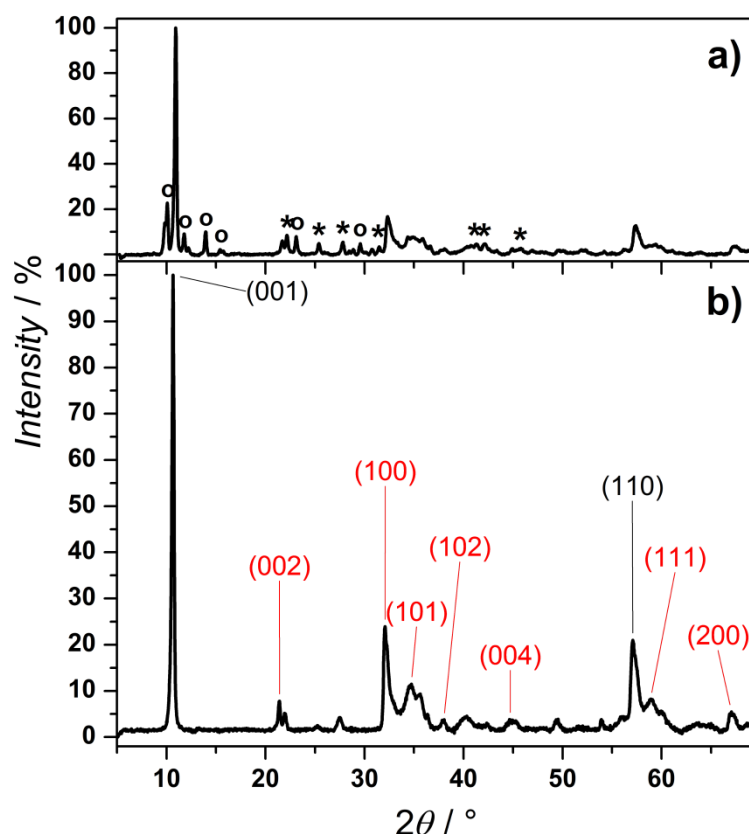


Figure 4.4: Powder XRD pattern of Mn(II) glycolate particles after synthesis at 170°C for (a) 1 h and (b) 7 h. In (a) reflections of the side products manganese acetate dihydrate (ICDD 00-056-0183) and manganese oxalate (ICDD 00-032-0646) are denoted by circles (o) and asterisks (*), respectively; in (b) black labels denote literature assignments[128] and red labels calculated reflection assignments for the brucite-type structure with lattice constants $a = b = 3.2 \text{ \AA}$ and $c = 8.2 \text{ \AA}$.

Sun *et al.* proposed that the Mn(II) glycolate structure widening in the c direction (the distance between the Mn-O sheets in the ab planes) is due to the long-chain ethylene glycolate anions interconnecting the ab planes of the unit cell[128]. In contrast to the synthesis presented here, however, Sun *et al.* did not use tetraethyleneglycol (TEG) in their polyol process[128]. As TEG anions being part of the structure would result in lattice constants $c > 8.2 \text{ \AA}$ for the Mn(II) glycolate presented in this work, it is assumed that TEG molecules only act as stabilizing ligands to the Mn(II) glycolate particles. This stabilization and the modified synthesis conditions (temperature and

4.1.2. Nanostructured pure-phase manganese oxides

heating rate) are considered to be the reasons for the by one order of magnitude smaller crystallite sizes compared to those of the Mn(II) glycolate particles presented in the previous section and reported in other studies[117,128].

The morphology of the as-synthesized Mn(II) glycolate was investigated by SEM and TEM analysis.

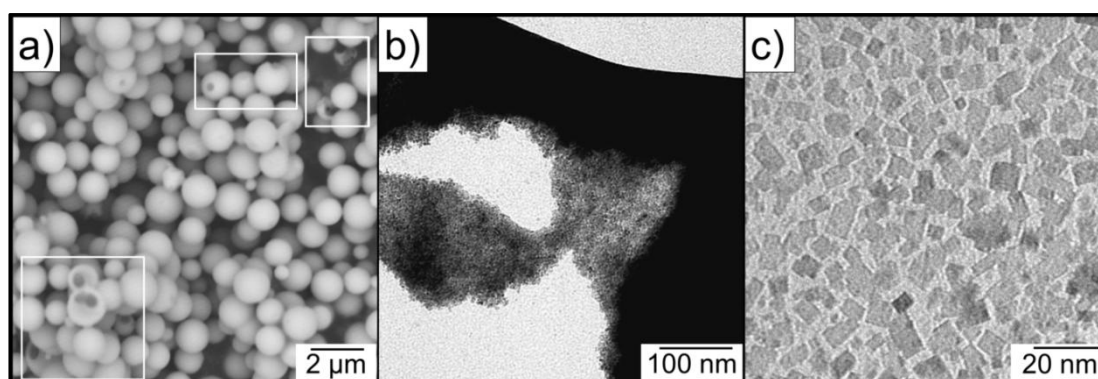


Figure 4.5: (a) SEM and (b), (c) TEM images of the Mn(II) glycolate precursor synthesized at 170°C for 7 h. (a) shows hollow spheres held by ligand shells, which can be seen in (b) to break open and contain (c) the Mn(II) glycolate nanoparticles.

Figure 4.5.a depicts SEM images of spherical Mn(II) glycolate particles with diameters $\leq 1 \mu\text{m}$. The broken outer shells of some spheres visible in the SEM image (highlighted by white frames) show, that the spherical particles are hollow. Such a broken sphere is depicted in the TEM image in Figure 4.5.b, which reveals that the spheres are in fact agglomerates of rectangular Mn(II) glycolate nanoparticles with diameters below 15 nm (Figure 4.5.c). The observed particle sizes are in good agreement with the calculated Scherrer crystallite sizes obtained from the XRD pattern (see Figure 4.4.b).

The impact of the reduction of the precursor particle sizes by another order of magnitude (compared to those obtained in section 4.1.1.1) on the

morphologies of the Mn_xO_y compounds produced by thermal decomposition processes is presented in the following sections.

4.1.2.2. The formation of various Mn_xO_y phases during heating

The temperature dependence of Mn_xO_y phase formation and transformation processes was investigated by *in situ*-X-ray diffraction in O_2 atmosphere during heating of the Mn(II) glycolate precursor particles from 35°C to 700°C with a heating rate of 2 K/min (see Figure 4.6).

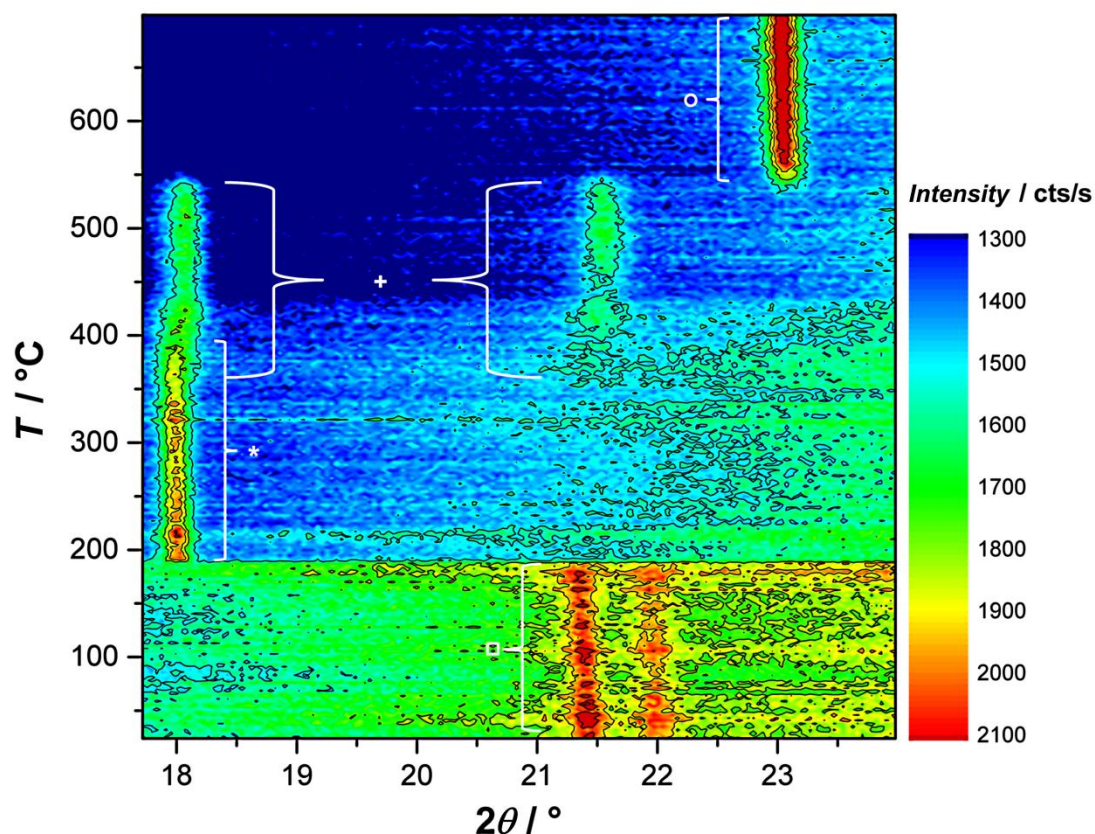


Figure 4.6: *In situ*-XRD patterns recorded during the heating of the Mn(II) glycolate precursor from 35°C to 700°C in an O_2 flow. The denoted reflections indicate the presence of Mn(II) glycolate (\square), Mn_3O_4 (*), Mn_5O_8 (+) and α - Mn_2O_3 (o); heating rate: 2 K/min.

4.1.2. Nanostructured pure-phase manganese oxides

All species expected to be generated during the oxidation process show reflections in the 2θ region from 17.6° to 23.8° , which was monitored during the measurement: 21.5° (Mn(II) glycolate, \square)[108], 18.0° (Mn_3O_4 , $*$)[130], 18.1° and 21.7° (Mn_5O_8 , $+$)[119], and 23.2° ($\alpha\text{-Mn}_2\text{O}_3$, o)[131].

The reflection of Mn(II) glycolate at 21.5° is observed in the temperature range between 35°C and 185°C . At this temperature a simultaneous decrease of the background intensity is observed in the diffraction patterns (visible as a horizontal line with a change of the background color from green to blue in Figure 4.6). This intensity decrease is attributed to the temperature-dependent decomposition of the organic ligands and anions by oxidation. The Mn_3O_4 reflection at 18.0° evolves at about 185°C immediately after the Mn(II) glycolate reflection has vanished. The decreasing intensity of the Mn_3O_4 reflection at 18.0° is accompanied by the appearance of the Mn_5O_8 reflection at 21.7° at about 350°C . Simultaneously, the intensity of the Mn_5O_8 reflection at 18.1° increases. These observations are attributed to a slow oxidation process of Mn_3O_4 to Mn_5O_8 . The Mn_3O_4 reflection at 18.0° disappears at about 440°C , indicating the complete oxidation of Mn_3O_4 to Mn_5O_8 . Both reflections assigned to Mn_5O_8 (at 18.1° and 21.7°) disappear at 550°C , subsequent to the appearance of the intense $\alpha\text{-Mn}_2\text{O}_3$ reflection at 23.2° at a temperature of about 530°C . This observation is attributed to the phase transformation of Mn_5O_8 to $\alpha\text{-Mn}_2\text{O}_3$.

Hence, in O_2 atmosphere Mn_3O_4 is present at temperatures between 185°C and 440°C , Mn_5O_8 between 350°C and 550°C and $\alpha\text{-Mn}_2\text{O}_3$ at temperatures above 530°C .

The oxidation of Mn_3O_4 to the metastable Mn_5O_8 phase rather than to Mn_2O_3 has previously been suggested to take place during the heating of Mn_3O_4 particles at temperatures between 250°C and 550°C in atmospheres containing $> 5\%$ O_2 [118]. The reduction process of Mn_5O_8 to $\alpha\text{-Mn}_2\text{O}_3$ in O_2 -

containing atmospheres was observed by several groups at temperatures $> 500^{\circ}\text{C}$ [113,120,131].

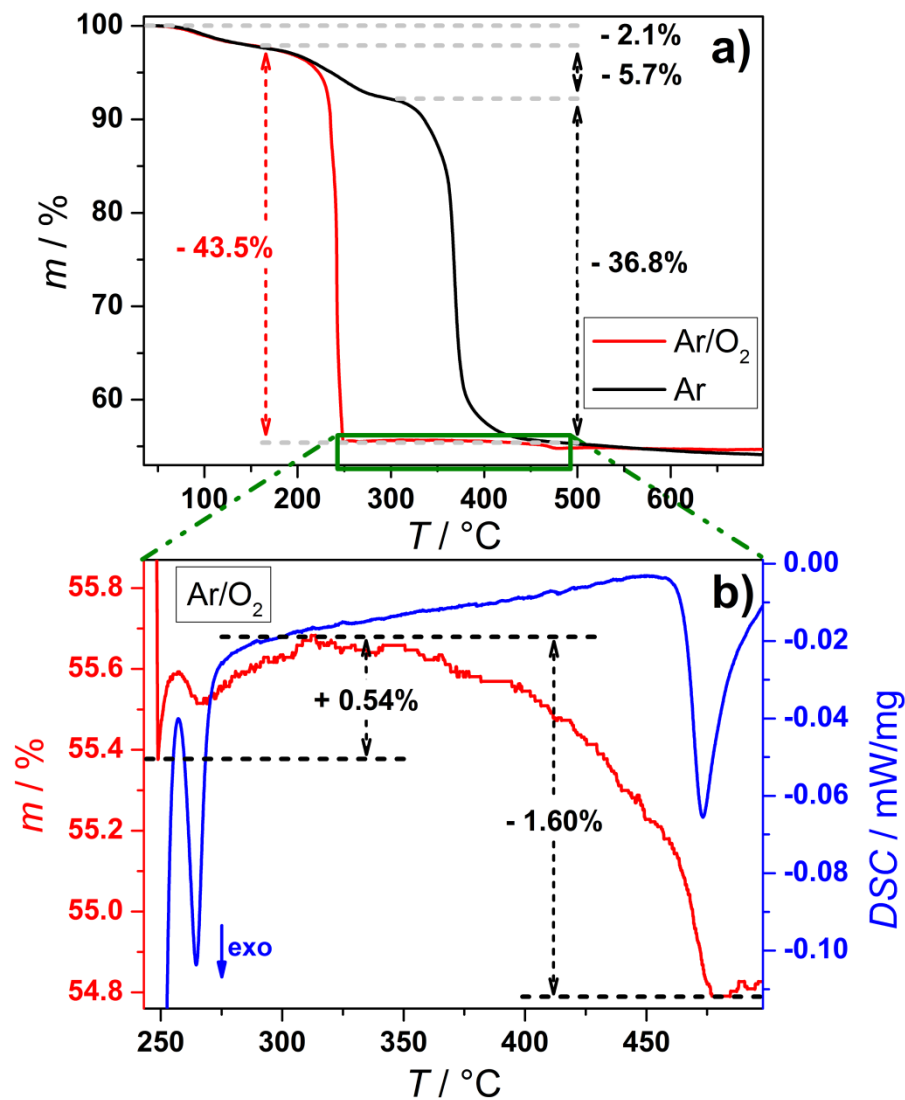


Figure 4.7: TGA/DSC measurements recorded during the heating of the Mn(II) glycolate precursor to 700°C in Ar and O_2/Ar (1:2) atmospheres. Gas atmospheres: Ar (black) and O_2/Ar (1:2) (red); heating rate: 2 K/min; gas flow: 40 Nml/min; (b) detailed view of the TGA (red) and DSC measurements (blue) in an O_2/Ar (1:2) atmosphere in a temperature range of 230°C to 500°C .

The temperature-dependent oxidation processes of Mn(II) glycolate to the various Mn_xO_y species observed in the *in situ*-XRD patterns in (oxidizing) O_2

4.1.2. Nanostructured pure-phase manganese oxides

atmosphere (see Figure 4.6) were further investigated by thermogravimetric analysis (TGA) and differential scanning calorimetry (DSC). Figure 4.7 (see previous page) shows a comparison of TGA/DSC measurements recorded during the heating of the Mn(II) glycolate samples to 700°C in an O₂/Ar (1:2) flow (red) to those recorded in a pure Ar flow (black).

A summary of the processes concluded from the observations made in the TGA/DSC measurements (Figure 4.7) and *in situ*-XRD patterns (Figure 4.6) is given in Table 4.1.

Table 4.1: Loss of sample masses detected during the TGA measurements and attributed processes in Ar and O₂/Ar atmospheres.

$T / ^\circ\text{C}$	$m / \%$		Processes	
	Ar	O ₂ /Ar (1:2)	Ar	O ₂ /Ar (1:2)
30 – 150		- 2.1	Water loss from the sample	
150 – 200	- 5.7	- 44	Ligand decomposition	Ligand & anion
200 – 250				decomposition
250 – 300		+ 0.5	Organic anion decomposition	Mn ₃ O ₄ oxidation to
300 – 350				Mn ₅ O ₈ & α -Mn ₂ O ₃
350 – 400	- 36.8	-1.6	(& Mn _x O _y formation)	Mn ₅ O ₈ reduction to
400 – 450				α -Mn ₅ O ₈
450 – 500				

Ar atmosphere. Subsequent to the initial water loss, the mass loss of 5.7% detected during the heating to a temperature of 320°C is attributed to the decomposition of organic TEG and EG ligands, whose boiling points are in the temperature range of 150°C to 320°C. A further mass loss of about 37% up to 450°C is probably due to the decomposition of the organic EG anions of the Mn(II) glycolate, which was suggested for Ti(IV) glycolate by Jiang *et al.*[132]. During this decomposition process Mn(II) glycolate is

assumed to be oxidized to Mn_xO_y similar to the proposal made in the aforementioned study on TiO_2 [132].

O_2/Ar atmosphere. A mass loss of about 44% attributed to the decomposition of the organic species of the precursor is observed at much lower temperatures between 150°C and 250°C (see Figure 4.7.a). This process was observed at 185°C in the *in situ*-XRD measurement in combination with an immediate oxidation to Mn_3O_4 in O_2 atmosphere (see Figure 4.6). The temperature delay of this process with respect to the results from the *in situ*-XRD measurements is most probably due to the smaller O_2 partial pressure in the gas atmosphere used for the TGA measurement. Hence, a clear assignment of the weight loss to specific processes cannot be made, as the decomposition of organic ligands and anions from the precursor and the oxidation to Mn_3O_4 take place simultaneously.

For the investigation of the processes occurring subsequent to the large mass loss a detailed view of the temperature region from 230°C to 500°C is depicted in Figure 4.7.b. Here, a small mass increase of 0.54% detected between 250°C and 330°C is accompanied by a DSC signal of an exothermal phase transformation at 270°C, which indicates an oxidation of Mn_3O_4 to Mn_5O_8 . This is in good agreement with the formation of the Mn_5O_8 phase observed at about 350°C in the *in situ*-XRD measurements (see Figure 4.6). The expected mass gain of 5.59% resulting from a complete oxidation of Mn_3O_4 to Mn_5O_8 , however, is ten times larger, which means that Mn_3O_4 is only partially oxidized to Mn_5O_8 . This assumption is supported by a recent study, which suggested that heating rates between 1.2 K/min and 2.5 K/min could lead to a direct oxidation of Mn_3O_4 to $\alpha\text{-Mn}_2\text{O}_3$ rather than to Mn_5O_8 in an O_2 atmosphere[114].

However, the subsequent mass loss of 1.60% from 330°C to 480°C as well as the DSC signal of an exothermal phase transformation at 480°C indicate the

4.1.2. Nanostructured pure-phase manganese oxides

reduction of Mn_5O_8 to $\alpha\text{-Mn}_2\text{O}_3$. This mass loss is lower than the calculated value of 2.03% for a complete conversion of Mn_5O_8 to $\alpha\text{-Mn}_2\text{O}_3$, which indicates that less $\alpha\text{-Mn}_2\text{O}_3$ is formed from Mn_5O_8 than expected. Hence, it is concluded that in an O_2/Ar atmosphere $\alpha\text{-Mn}_2\text{O}_3$ is generated partially from Mn_5O_8 and partially by direct oxidation from Mn_3O_4 .

The mass increase and decrease in oxidizing atmospheres between 250°C and 500°C was proposed to be due to slow seed crystal oxidation[118]. Here, Mn_3O_4 nanoparticles with surface areas of more than $10\text{ m}^2/\text{g}$ are suggested to be oxidized to Mn_5O_8 with a subsequent formation of $\alpha\text{-Mn}_2\text{O}_3$ [117,118]. Therefore, these observations give first indications of a formation of Mn_3O_4 nanoparticles by annealing of the Mn(II) glycolate particles.

4.1.2.3. Mn_xO_y species by calcination at different temperatures

In order to obtain different Mn_xO_y compounds the precursor was calcined at temperatures between 320°C and 550°C in pure Ar or O_2 atmospheres for 2 h. X-ray diffractograms of the resulting Mn_xO_y compounds and the respective reference patterns are shown in Figure 4.8 (see next page).

The dependence of the low-angle reflection intensities of the different Mn_xO_y species (blue marks in Figure 4.8) on the calcination temperature in oxidizing and neutral gas atmospheres is depicted in Figure 4.9 (see p. 48). It has to be pointed out, however, that the reflection intensities do not give quantitative insight, but only indicate the formation and presence of the different Mn_xO_y compounds in the products.

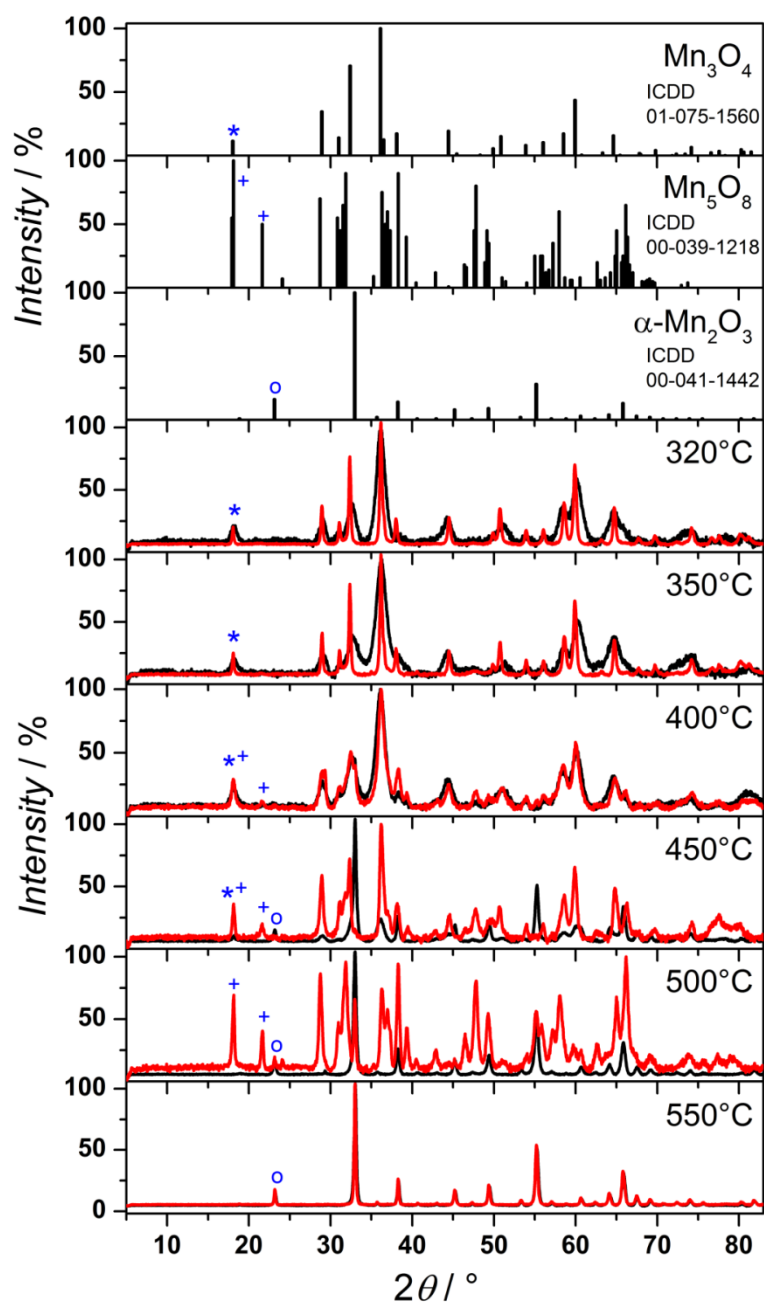


Figure 4.8: Powder XRD patterns of the Mn_xO_y products obtained after calcination at temperatures between 320°C and 550°C for 2 h. Gas atmospheres: Ar (black) and O_2 (red); gas flow: 50 NL/h; reference patterns are depicted at the top for Mn_3O_4 , Mn_5O_8 and $\alpha\text{-Mn}_2\text{O}_3$; asterisk (*), cross (+) and circle (o) mark the respective low-angle reflections observed in the *in situ*-XRD measurements (see Figure 4.6).

The low-angle reflection intensities of the different Mn_xO_y species obtained at different calcination temperatures (see Figure 4.9) show that at low

4.1.2. Nanostructured pure-phase manganese oxides

calcination temperatures of 320°C and 350°C Mn_3O_4 is the only species present in both atmospheres. In an Ar atmosphere this does not change up to a calcination temperature of 400°C. The presence of Mn_5O_8 , however, is indicated at 400°C in an oxidizing atmosphere by the appearance of a reflection at 21.7° and a simultaneous stronger intensity increase of the reflection at about 18° (assigned to Mn_3O_4 and Mn_5O_8) compared to that observed in an Ar atmosphere.

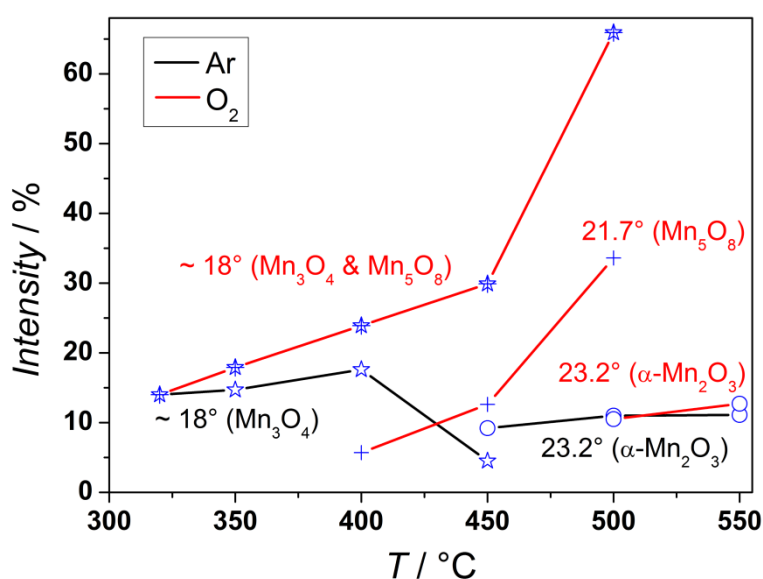


Figure 4.9: Mn_xO_y low-angle reflection intensities detected at different calcination temperatures in Ar (black) and O_2 atmospheres (red). Intensities of the reflections, which indicate the presence of Mn_3O_4 (*), Mn_5O_8 (+) and $\alpha\text{-Mn}_2\text{O}_3$ (o) (taken from Figure 4.8).

The Mn_5O_8 phase is obtained up to a calcination temperature of 500°C only in O_2 atmospheres. It is, however, not present as a pure phase at any of the temperatures between 400°C and 500°C. At a calcination temperature of 500°C a product mixture of Mn_5O_8 and $\alpha\text{-Mn}_2\text{O}_3$ (identified by the reflection at 23.2°) is obtained in an O_2 atmosphere. After calcination at 450°C in an Ar atmosphere $\alpha\text{-Mn}_2\text{O}_3$ is present in a product mixture with Mn_3O_4 . A pure

phase of α -Mn₂O₃ is obtained by annealing at 500°C and 550°C in Ar atmospheres as well as at 550°C in an O₂ atmosphere.

Table 4.2: Crystalline Mn_xO_y phases obtained after calcination at temperatures between 320°C and 550°C in Ar and O₂ atmospheres. Mean Scherrer crystallite sizes $d_{\text{crystallite}}$ (calculated from all assigned reflections with eq. (3.1)) and lattice parameters (calculated from the (101) and (004) reflections of Mn₃O₄ with eq. (3.6) as well as the (400) reflection of α -Mn₂O₃ with eq. (3.8)) are given for the pure-phase products.

$T / ^\circ\text{C}$	Gas	Mn _x O _y phases	Lattice constants / Å	$d_{\text{crystallite}} / \text{nm}$
320	Ar	Mn ₃ O ₄	$a = 5.72$ $c = 9.38$	11 ± 3
	O ₂	Mn ₃ O ₄	$a = 5.75$ $c = 9.47$	38 ± 11
350	Ar	Mn ₃ O ₄	$a = 5.69$ $c = 9.44$	10 ± 3
	O ₂	Mn ₃ O ₄	$a = 5.74$ $c = 9.47$	35 ± 10
400	Ar	Mn ₃ O ₄	$a = 5.73$ $c = 9.39$	9 ± 2
	O ₂	Mn ₃ O ₄ , Mn ₅ O ₈		
450	Ar	α -Mn ₂ O ₃ , Mn ₃ O ₄		
	O ₂	Mn ₃ O ₄ , Mn ₅ O ₈		
500	Ar	α -Mn ₂ O ₃	$a = 9.41$	27 ± 4
	O ₂	Mn ₅ O ₈ , α -Mn ₂ O ₃		
550	Ar	α -Mn ₂ O ₃	$a = 9.40$	34 ± 5
	O ₂	α -Mn ₂ O ₃	$a = 9.41$	44 ± 12

The influence of the calcination temperatures and gas atmospheres on the structural properties of the different Mn_xO_y products obtained under the different calcination conditions are discussed below. The lattice constants and

4.1.2. Nanostructured pure-phase manganese oxides

crystallite sizes presented in Table 4.2 (see previous page) were obtained from the XRD patterns depicted in Figure 4.8.

Mn₃O₄. The tetragonal Mn₃O₄ phase (ICDD 01-075-1560, *I4₁/amd*) is observed in the powder XRD patterns after calcination at temperatures between 320°C and 450°C in both atmospheres. It is, however, obtained as a pure phase only at temperatures up to 400°C in Ar and up to 350°C in O₂ (see Figure 4.8 and Table 4.2).

The lattice parameters and crystallite sizes of the pure Mn₃O₄ samples obtained by calcination at 320°C and 350°C (see Table 4.2) seem to be independent of the calcination *temperature* but dependent on the calcination *atmosphere*. The Mn₃O₄ phases generated in neutral atmospheres exhibit crystallite sizes of only about 30% compared to those obtained in the presence of O₂. Furthermore, the lattice constants of the Mn₃O₄ products calcined in Ar atmospheres are smaller at all temperatures compared to those obtained by calcination in oxidizing atmospheres. This is suggested to be due to oxygen vacancies, as in a neutral atmosphere the oxygen for the precursor oxidation to Mn₃O₄ can only be supplied by the decomposing organic species of the Mn(II) glycolate particles.

The smaller standard deviations of the lattice constants of pure-phase Mn₃O₄ obtained at calcination temperatures of 320°C and 350°C in oxidizing atmospheres (see Table 4.2) indicate completely occupied oxygen sites in the Mn₃O₄ structure. The contraction of the lattice constants proposed for Mn₃O₄ obtained by calcination in Ar, has previously also been attributed to oxygen vacancies and disorders in the structure of TiO₂, which has the same space group as Mn₃O₄[91].

α-Mn₂O₃. Cubic α-Mn₂O₃ (ICDD 00-041-1442, *Ia $\bar{3}$*) is obtained after calcination at temperatures between 450°C and 550°C in Ar and between 500°C and 550°C in O₂. Pure-phase α-Mn₂O₃, however, is only obtained after

calcination at temperatures of 500°C and 550°C in Ar and at 550°C in O₂ atmospheres (see Table 4.2). The observation of the α -Mn₂O₃ phase after calcination at 500°C in the presence of O₂ supports the results of the TGA/DSC measurements (see Figure 4.7.b), which show a generation of α -Mn₂O₃ from Mn₅O₈ in an O₂ atmosphere at a temperature of about 480°C. This is attributed to an additional time dependence of the phase transformation of Mn₅O₈ to α -Mn₂O₃, which was also suggested by Dimesso *et al.*[116]. In their report, α -Mn₂O₃ was proposed to be the minor phase next to that of Mn₅O₈ after calcination at 400°C in air for 1 h but the major phase after a prolonged calcination time of 5 h.

The lattice constants of the pure-phase α -Mn₂O₃ products obtained by calcination at 500°C and 550°C seem to be independent of the calcination temperature and the calcination atmosphere (see Table 4.2). Hence, the absence of O₂ in the calcination atmosphere does not lead to an amount of oxygen vacancies in the α -Mn₂O₃ structure, which is large enough to significantly change the lattice constants. The Scherrer crystallite sizes, however, indicate a *temperature* dependence of the α -Mn₂O₃ particle sizes in Ar atmospheres, which was not the case for Mn₃O₄. At 550°C the crystallite diameter of the pure-phase α -Mn₂O₃ obtained in an oxidizing atmosphere is about 30% larger compared to that of the α -Mn₂O₃ phase obtained in the absence of O₂ (see Table 4.2).

Hence, an oxidizing calcination atmosphere is suggested to result in larger Mn₃O₄ as well as α -Mn₂O₃ crystallites.

Mn₅O₈. No pure phase of monoclinic Mn₅O₈ (ICDD 00-039-1218, *C2/m*) is obtained by calcination at temperatures between 320°C and 550°C in Ar and O₂ atmospheres for 2 h. However, after calcination at temperatures between 400°C and 500°C in oxidizing atmospheres Mn₅O₈ is detected as a fraction of the obtained product mixtures.

4.1.2. Nanostructured pure-phase manganese oxides

The calcination process of the Mn(II) glycolate precursor yielding pure-phase Mn_5O_8 , which has not yet been investigated as an ORR electrocatalyst in aprotic media, is presented in the next section.

4.1.2.4. *The formation of pure-phase Mn_5O_8 by calcination*

The results discussed in the preceding sections show that the conditions to obtain pure-phase Mn_5O_8 are (i) an O_2 -containing calcination atmosphere (see TGA measurements in Figure 4.7) and (ii) calcination temperatures between 350°C and 530°C (see *in situ*-XRD patterns in Figure 4.6). In order to investigate the time dependence of the Mn_5O_8 formation from Mn_3O_4 , which was already proposed in section 4.1.1.2, time profile *in situ*-XRD measurements were conducted at 400°C in an O_2 atmosphere.

The *in situ*-XRD patterns depicted in Figure 4.10 (see next page) show the time-dependent oxidation of Mn_3O_4 (reflection at 18.0° , *) [130] to Mn_5O_8 (reflections at 18.1° and 21.7° , +) [119]. After an initial heating of Mn(II) glycolate to 400°C at 18 K/min in an O_2 flow the temperature was kept constant for 350 min.

The reflection at 18.0° observed in Figure 4.10 and the absence of a reflection at 21.5° indicate an already complete oxidation of Mn(II) glycolate to Mn_3O_4 at the start of the measurement. The Mn_5O_8 reflection at 21.7° appears after about 40 min. The oxidation process of Mn_3O_4 to Mn_5O_8 is also observed by a steady shift of the reflection at 18.0° to 18.1° , which starts after 25 min and ends after about 150 min of the measurement (see the white arrow in the red square in Figure 4.10). This is due to decreasing Mn_3O_4 (18.0°) and increasing Mn_5O_8 reflection intensities (18.1°), until the reflection at 18.0° (Mn_3O_4) disappears completely after about 150 min of constant

heating at 400°C. This observation is in good agreement with the mixed-phase $\text{Mn}_3\text{O}_4/\text{Mn}_5\text{O}_8$ products obtained after calcination at 400°C for 2 h in O_2 flows presented in sections 4.1.1.2 and 4.1.2.3 (see XRD patterns in Figure 4.2 and Figure 4.8).

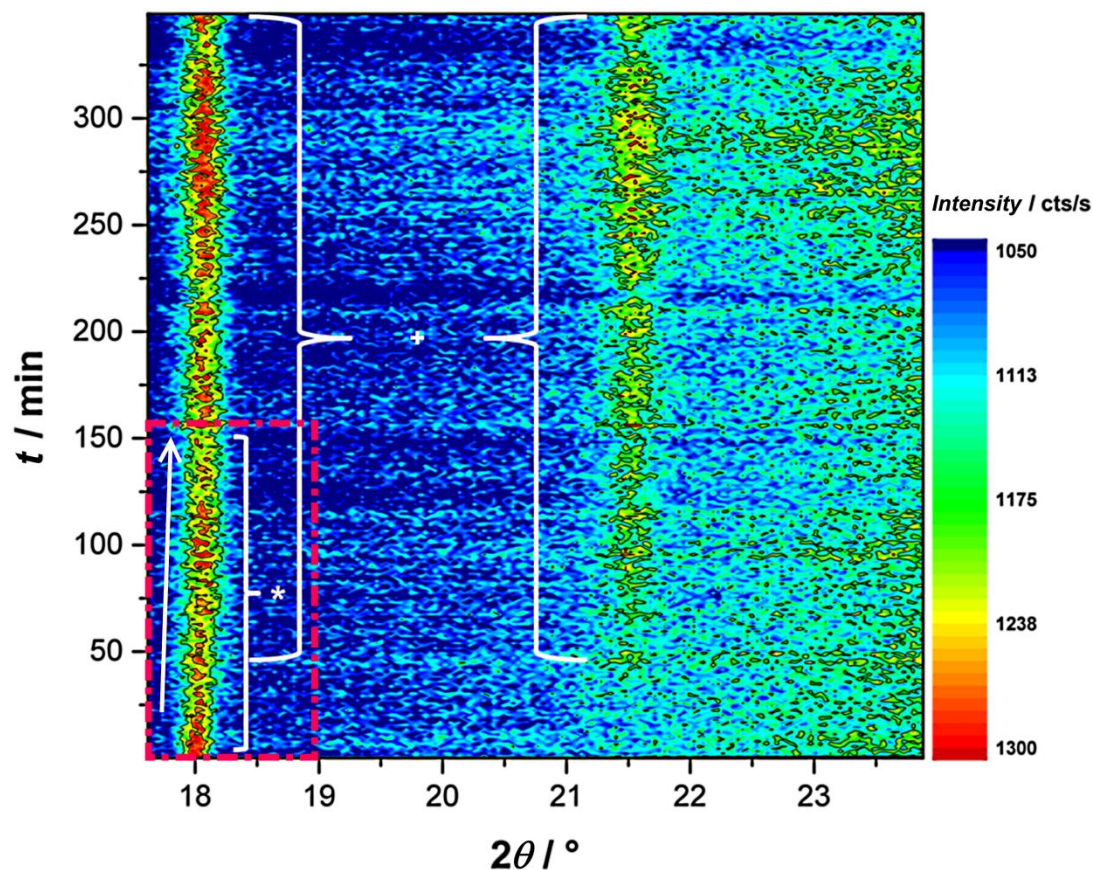


Figure 4.10: *In situ*-XRD patterns during constant heating of the Mn(II) glycolate precursor at 400°C for 350 min in an O_2 flow. From the start until the end of the measurement the denoted reflections indicate the presence of Mn_3O_4 (*) and Mn_5O_8 (+); the white arrow indicates the shift of the reflection at 18.0° to 18.1° ; for further information, see text.

Starting at 150 min until the end of the measurement the reflection is constantly detected at 18.1° indicating the end of the oxidation process. The presence of $\alpha\text{-Mn}_2\text{O}_3$ was observed by the intense reflection at 23.2° in the *temperature*-dependent *in situ*-XRD measurements (see Figure 4.6) despite

4.1.2. Nanostructured pure-phase manganese oxides

increasing background reflection intensities with increasing 2θ (see the background color shift from blue to green in Figure 4.6 and Figure 4.10). In the *time*-dependent *in situ*-XRD patterns recorded at 400°C, however, a reflection of α -Mn₂O₃ at 23.2° is not detected (see Figure 4.10). The results presented here show that calcination at 400°C in an oxidizing atmosphere for 150 min to 350 min yields pure Mn₅O₈ phase without any α -Mn₂O₃ formation.

Based on these observations the Mn(II) glycolate precursor was calcined at 400°C for 300 min in O₂ atmosphere to yield pure-phase Mn₅O₈. The XRD pattern of the obtained product is depicted in Figure 4.11.

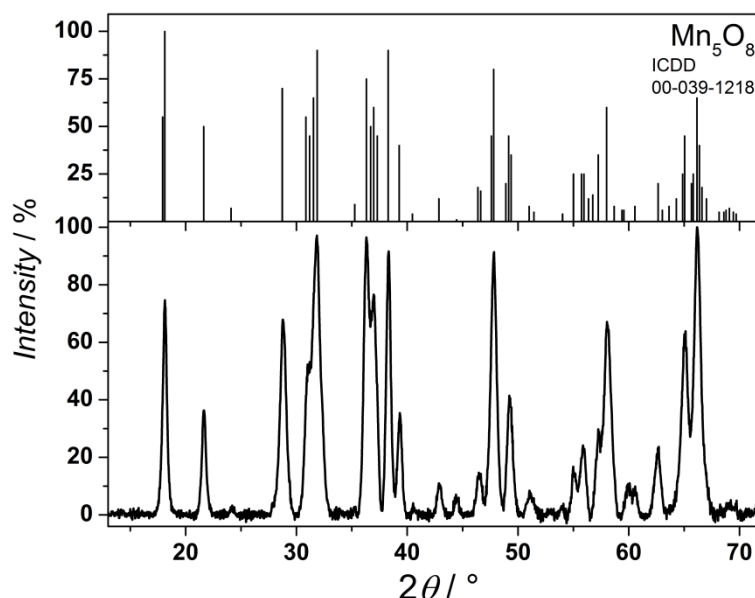


Figure 4.11: XRD pattern of Mn₅O₈ obtained by calcination at 400°C for 5 h in an O₂ atmosphere. Gas flow: 50 NL/h; the reference pattern of Mn₅O₈ is depicted at the top.

From the XRD pattern mean Scherrer crystallite sizes of 22 nm ± 5 nm were calculated for Mn₅O₈ with eq. (3.1). The lattice parameters obtained for the monoclinic product (ICDD 00-039-1218) are $a = 10.40$ Å, $b = 5.73$ Å and $c = 4.87$ Å with $\beta = 109.6^\circ$ (eq. (3.7)), which is in good agreement with data

from the literature ($a = 10.34 \text{ \AA}$, $b = 5.72 \text{ \AA}$ and $c = 4.85 \text{ \AA}$ with $\beta = 109.25^\circ$)[119].

4.1.2.5. Morphological and structural characterization of the Mn_3O_4 , Mn_5O_8 and α - Mn_2O_3 compounds

This section investigates the morphological properties of the pure Mn_5O_8 compound presented in the previous section as well as those of Mn_3O_4 and α - Mn_2O_3 obtained by calcination in Ar atmospheres at 350°C and at 550°C (see section 4.1.2.3), respectively. These Mn_3O_4 and α - Mn_2O_3 compounds are of interest for catalytic investigations because of their small crystallite sizes calculated from the XRD reflections (see Table 4.2). The presence of structural oxygen vacancies deduced from the comparably small lattice constants (see section 2.4.3) might further increase the catalytic activity of Mn_3O_4 . The unit cells of the above-mentioned Mn_xO_y species constructed by using the respective lattice constants are depicted in Figure 4.12 (see next page).

For the analysis of the morphologies, particle sizes and active surface areas of the Mn_xO_y compounds TEM and N_2 adsorption-desorption measurements were carried out, which are discussed in the following.

4.1.2. Nanostructured pure-phase manganese oxides

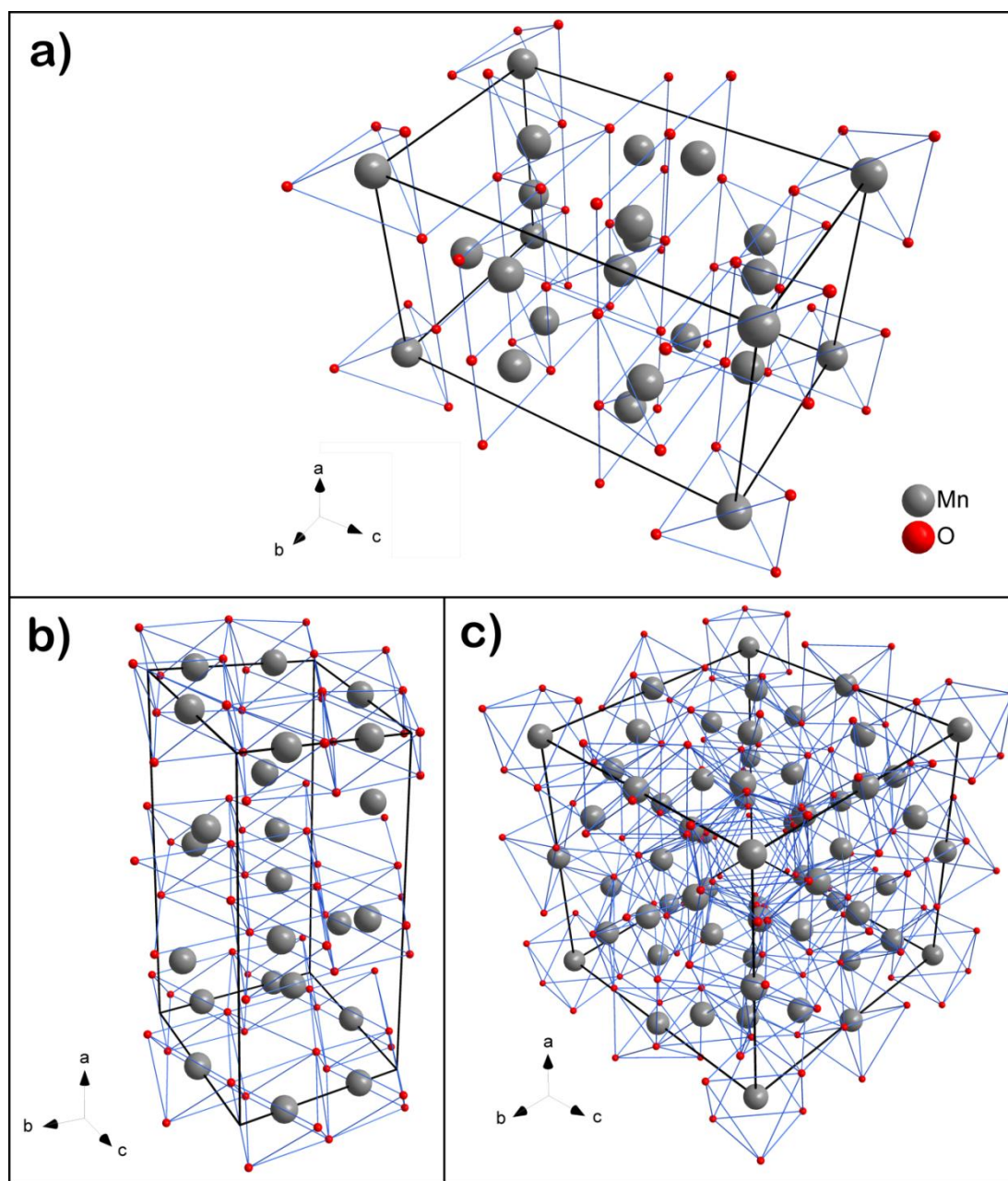


Figure 4.12: Schemes of the unit cells of the Mn_xO_y species of interest for the ORR investigations. The unit cells represent (a) Mn_3O_4 (Ar, 350°C, 2 h), (b) Mn_5O_8 (O_2 , 400°C, 5 h) and (c) $\alpha\text{-Mn}_2\text{O}_3$ (Ar, 550°C, 2 h) and were constructed from the lattice parameters obtained from XRD measurements (given in Table 4.2).

The particle sizes of the Mn_3O_4 and Mn_5O_8 compounds observed in the TEM images (see Figure 4.13.a and b on the next page, respectively) are in

good agreement with the Scherrer crystallite sizes calculated from the XRD patterns (see Table 4.2 for comparison).

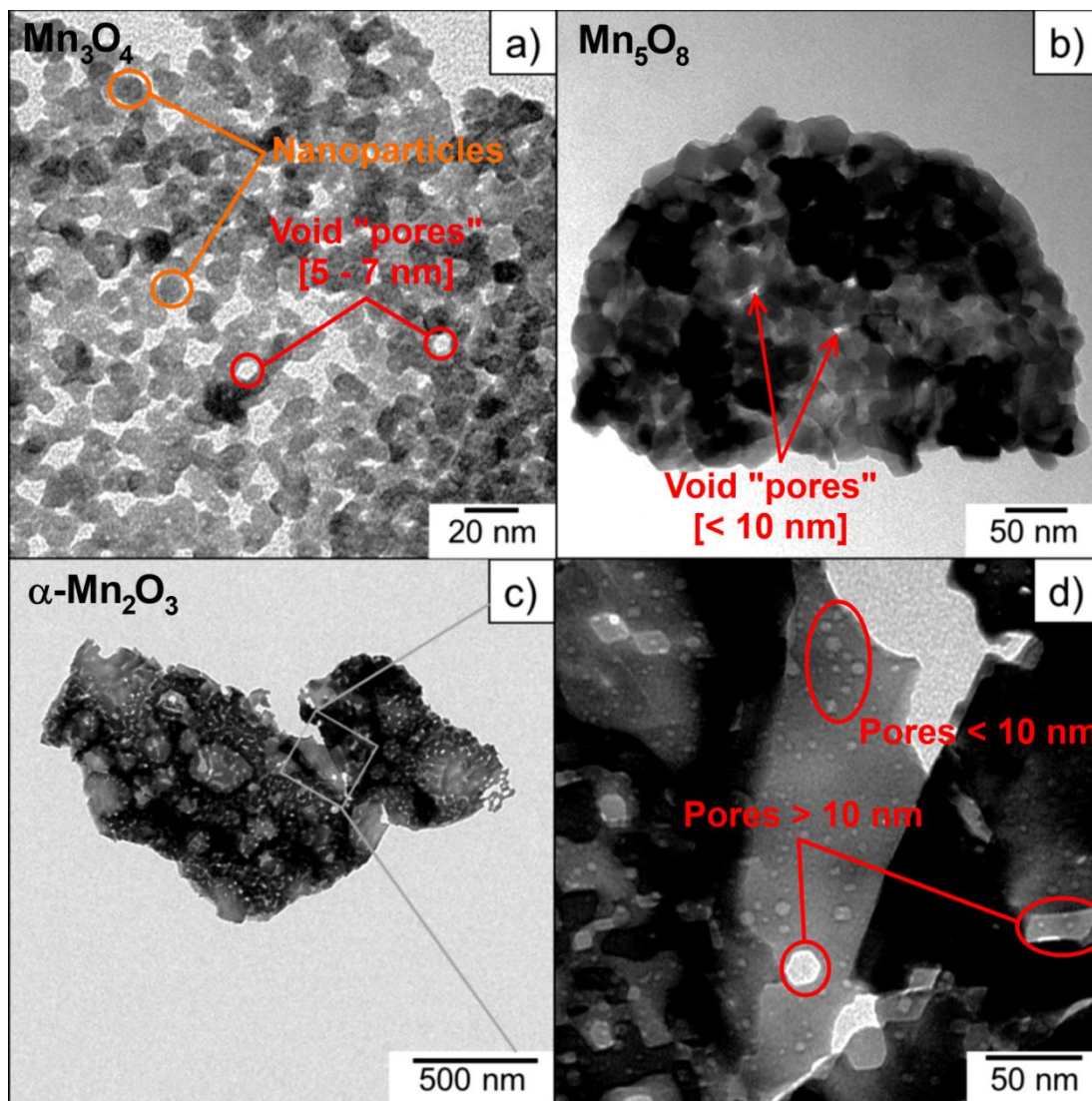


Figure 4.13: TEM images of the (a) Mn_3O_4 , (b) Mn_5O_8 and (c), (d) $\alpha\text{-Mn}_2\text{O}_3$ particles. The different types of pores detected in N_2 adsorption-desorption measurements (see Figure 4.14) are highlighted by red circles, nanoparticles of the Mn_3O_4 sample in (a) are highlighted by orange circles.

Mn_3O_4 consists of a network of nanoparticles with diameters below 10 nm (see orange circles in Figure 4.13.a) and voids between the particles of about the same size (see red circles in Figure 4.13.a).

4.1.2. Nanostructured pure-phase manganese oxides

A comparable observation is made for Mn_5O_8 . Here, however, the nanoparticles with diameters of up to 40 nm are stacked in layers, which results in a densely packed agglomerate with small voids (< 10 nm) between the particles (see red arrows in Figure 4.13.b). This is attributed to the increased temperature and duration of the calcination process. Here, the particle growth resulting from oxidizing calcination atmospheres, which was discussed for the Mn_3O_4 and $\alpha\text{-Mn}_2\text{O}_3$ species in section 4.1.2.3, might be another reason for the formation of Mn_5O_8 particle agglomerates.

$\alpha\text{-Mn}_2\text{O}_3$, on the other hand, consists of splinter-like particles in the μm range (ca. $0.5 - 2 \mu\text{m}$ in Figure 4.13.c and d) with a large amount of pores. These pores show (at least) two size distributions with diameters (i) in the range of 2 nm to 8 nm and (ii) larger than 15 nm (see red circles in Figure 4.13.d). The Scherrer crystallite sizes of $34 \text{ nm} \pm 5 \text{ nm}$ calculated from the XRD patterns of $\alpha\text{-Mn}_2\text{O}_3$ (see Table 4.2 and Figure 4.8) are obviously not in good agreement with the large particle diameters. Considering the large amount of pores observed in the particles, the calculated Scherrer crystallite sizes are suggested to result from the crystallite domains between the pore walls, i.e., are attributed to the *mean distances* between the pores. This assumption is in good agreement to the pore distances observed in the TEM images (see Figure 4.13.d).

From the isotherms obtained by N_2 adsorption-desorption measurements specific BET surface areas of $302 \text{ m}^2/\text{g}$, $30 \text{ m}^2/\text{g}$ and $20 \text{ m}^2/\text{g}$ were calculated for Mn_3O_4 , Mn_5O_8 and $\alpha\text{-Mn}_2\text{O}_3$, respectively (see Figure 4.14.a on the next page). The porosity of the $\alpha\text{-Mn}_2\text{O}_3$ particles observed in the TEM images (see Figure 4.13.c and d) is confirmed by the adsorption-desorption hysteresis behavior of the corresponding N_2 adsorption-desorption isotherms (blue in Figure 4.14.a). Hysteresis behavior is also detected for the Mn_3O_4 and Mn_5O_8

nanoparticles, although no pores are observed in the TEM images of these compounds (see Figure 4.13.a and b). Therefore, two different definitions of porosity have to be applied for the different Mn_xO_y species, which will be discussed in the following.

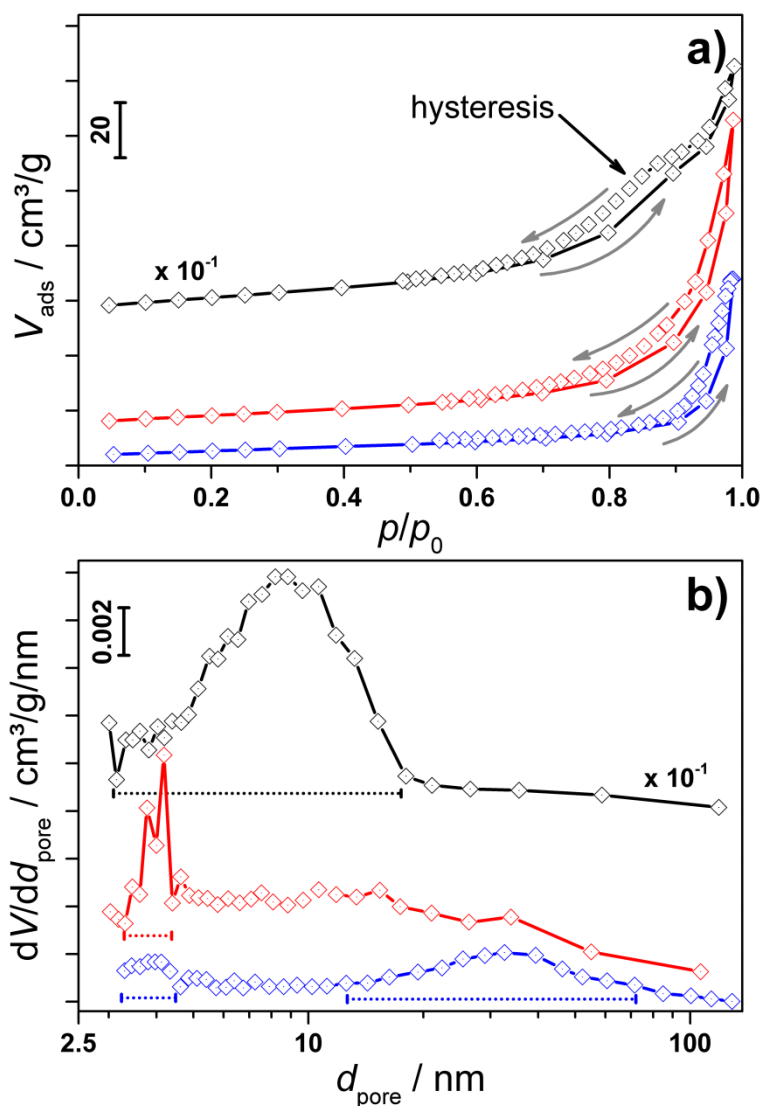


Figure 4.14: (a) N_2 adsorption-desorption isotherms and (b) the corresponding pore size distributions of Mn_3O_4 , Mn_5O_8 and $\alpha\text{-Mn}_2\text{O}_3$. Mn_3O_4 (black), Mn_5O_8 (red) and $\alpha\text{-Mn}_2\text{O}_3$ (blue); in (a) the black arrow denotes adsorption-desorption hysteresis behavior for the example of the Mn_3O_4 sample, which indicates porosity; in (b) the ranges of the most prominent pore size distributions are denoted by dotted lines.

4.1.2. Nanostructured pure-phase manganese oxides

Mn₃O₄ and Mn₅O₈. For the Mn₃O₄ compound the pore size distribution is in the range of 3 nm to 20 nm with a mean pore diameter of 8.2 nm (see dotted black line in Figure 4.14.b). The porosity of the Mn₃O₄ nanoparticles can be explained by considering the voids observed in the particle network (see red circles in the TEM image given in Figure 4.13.a) as the “pores” detected in the N₂ adsorption-desorption measurements. The same “void pore” definition can be applied to the Mn₅O₈ sample exhibiting pore sizes between 3 nm and 5 nm with a comparably small mean pore size of 4.2 nm (see dotted red line in Figure 4.14.b). For this compound, void diameters < 10 nm between the particles are observed in the particle agglomerate (see red arrows in the TEM image in Figure 4.13.b).

α-Mn₂O₃. Pore size distributions between 3 nm and 5 nm as well as 10 nm and 80 nm with a mean diameter of 32.6 nm are obtained for the α-Mn₂O₃ compound (see dotted blue lines in Figure 4.14.b), which is in good agreement with observation two pore size distributions in the TEM images (see Figure 4.13.d). Because α-Mn₂O₃ does not consist of nanoparticles, these pores are attributed to a mesoporosity of the splinter-like particles rather than to voids in a nanoparticle network.

Mesoporosity has previously been reported for circular and hexagonally shaped Mn₂O₃ particles obtained by calcination at temperatures above 600°C[131,133]. Ren *et al.* suggested the mesopores to derive from a sequence of processes, which include Mn₅O₈ nanoparticle growth, re-arrangement and merging during the transformation to α-Mn₂O₃[131]. As the Mn₅O₈ phase was not observed after calcination in a Ar atmosphere used for the synthesis of the α-Mn₂O₃ particles, the pores in the α-Mn₂O₃ compound presented here are attributed to derive from comparable growth, re-arrangement and merging processes of Mn₃O₄ nanoparticles.

4.1.3. Conclusion

In summary, a polyol synthesis yielded rectangular Mn(II) glycolate nanoparticles with diameters of $17 \text{ nm} \pm 8 \text{ nm}$, which is the first time that particles of this compound with sizes below 100 nm have been reported. This is attributed to the use of the stabilizing TEG ligands in combination with modified reaction conditions, i.e., a larger heating rate and a decreased temperature compared to those used in other reports.

In situ-XRD measurements showed a sequence of time- and temperature-dependent phase transformations during the heating of the Mn(II) glycolate particles in O_2 atmosphere, which results in the formation of $\alpha\text{-Mn}_2\text{O}_3$ by oxidation of Mn_3O_4 *via* Mn_5O_8 . Structural and morphological investigations revealed the dependence of the lattice constants and particle sizes of the Mn_xO_y species on the presence of O_2 in the calcination atmosphere as well as on the calcination temperatures. Based on the insights obtained from these measurements several manganese oxides could be synthesized by the calcination of Mn(II) glycolate particles in neutral and oxidizing atmospheres at different temperatures. The calcination process yielded Mn_3O_4 and Mn_5O_8 nanoparticles as well as mesoporous $\alpha\text{-Mn}_2\text{O}_3$ particles with large surface areas as a result of the small precursor particle diameters.

The most promising species for an electrocatalytic investigation are the Mn_3O_4 and $\alpha\text{-Mn}_2\text{O}_3$ particles due to the presence of oxygen vacancies in the former compound and the mesoporous character of the latter.

A summary of the structural and morphological properties of the different Mn_xO_y species is given in Table 4.3.

4.1.3. Conclusion

Table 4.3: Summary of the properties of the Mn_xO_y samples of interest for the ORR investigations in section 4.3; bulk material conductivities σ_{bulk} of the different species (taken from the literature) are given for use in section 4.3.

	Mn_3O_4	Mn_5O_8	$\alpha\text{-Mn}_2\text{O}_3$
Treatment	Ar, 2 h, 350 °C	O_2 , 5 h, 400 °C	Ar, 2 h, 550 °C
$d_{\text{crystallite}} / \text{nm}$	10 ± 3	22 ± 5	500 – 2000
$d_{\text{pore}} / \text{nm}$	3 – 20 (voids)	3 – 5 (voids)	3 – 5; 10 – 80
$A_{\text{BET}} / \text{m}^2/\text{g}$	302	30	20
Lattice const. / Å	$a = 5.69;$ $c = 9.44$	$a = 10.40;$ $b = 5.73;$ $c = 4.87;$ $\beta = 109.6^\circ$	$a = 9.40$
Space group	$I4_1/amd$	$C2/m$	$Ia\bar{3}$
$\sigma_{\text{bulk}} / (\Omega \cdot \text{cm})^{-1}$	$1.56 - 6.25 \cdot 10^{-9}$ [134]	n.a.	$\sim 2.5 \cdot 10^{-6}$ [134]

As catalytic activity can be enhanced by a larger active area resulting from small particle diameters and/or mesoporosity, the combination of polyol and calcination processes is proposed to be a suitable synthesis for active Mn_xO_y materials. Furthermore, the synthesis of different Mn_xO_y species *via* one route has the substantial advantage that any synthesis-caused impact on the catalytic activities can be excluded, so that the electrochemical investigation captures only the material properties of the different manganese oxides.

4.2. Characterization of the electrochemical system

Prior to the investigation of the catalytic ORR activities of the Mn_xO_y compounds presented in section 4.3, preliminary linear sweep voltammetry (LSV) and cyclic voltammetry (CV) measurements are presented in this section. These investigations concern (i) the suitability of various electrolytes for the electrochemical measurements based on their electrochemical stabilities and ORR/OER reversibilities, and the impact of (ii) the electrode preparation as well as (iii) the application of different experimental setup parameters.

4.2.1. Electrolyte characterization

This section presents the investigation various aprotic liquids being commonly used as solvents in aprotic electrolytes for the Li/air system. Furthermore, a solvent mixture of BMPTFSI/DMSO (1:100) is investigated with the intention of utilizing the ionic liquid's advantages by decreasing its high viscosity. The different solvents are tested with lithium bis(trifluoromethylsulfonyl)imide (LiTFSI) as conducting salt for their applicability in the experimental setup with regard to their electrochemical stabilities in the required potential window as well as their reversibility properties regarding the ORR/OER processes.

The LSV measurements depicted in Figure 4.15 (see next page) show the electrochemical stabilities of the different electrolytes in the potential window of 2 V ... 4 V vs. Li/Li⁺ (dashed grey lines), which is required for the observation of ORR and OER processes. In this potential range similar stabilities are observed for all investigated electrolytes with only slightly

4.2.1. Electrolyte characterization

increasing currents at potentials beyond the boundaries of the required potential window.

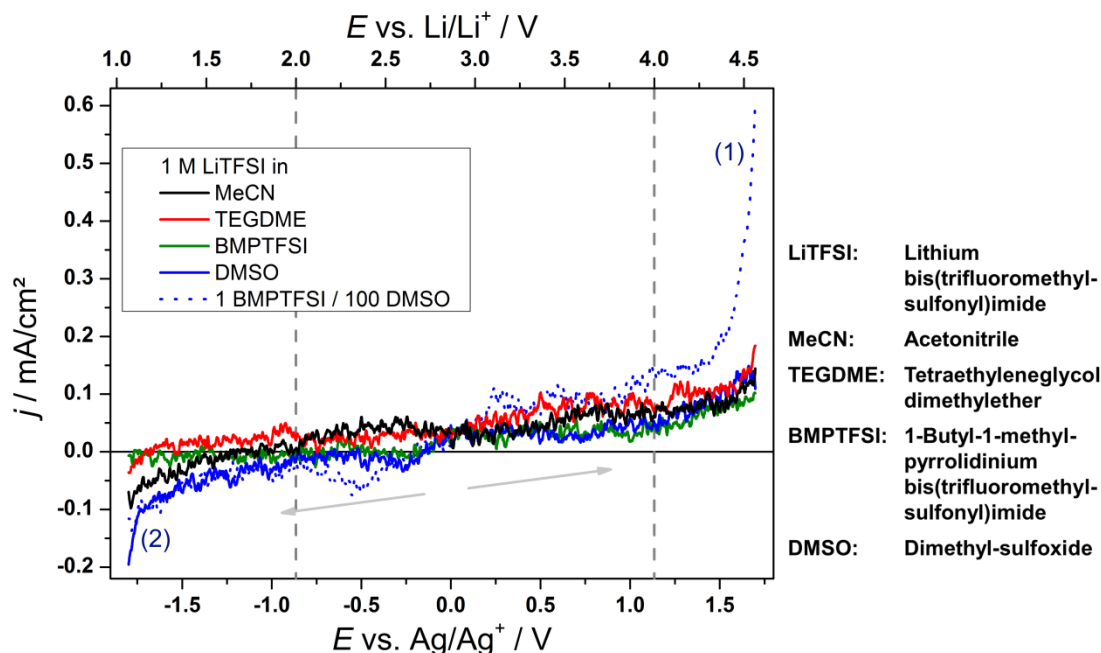


Figure 4.15: LSV measurements recorded in different Ar-saturated electrolytes. WE: GC; $\nu = 100$ mV/s; electrolytes (1 M LiTFSI in): MeCN (black line), TEGDME (red line), BMPTFSI (green line), DMSO (blue line) and BMPTFSI/DMSO (1:100) (dotted blue line); the potential window vs. Li/Li⁺ required for the ORR/OER processes is marked by the dashed grey lines. (Note: the comparably high current densities in the potential range of 2 V ... 4 V vs. Li/Li⁺ are most probably due to a slight contamination with oxygen.)

An exception to the observation of an only slight current density increase at $E > 4$ V vs. Li/Li⁺ is the BMPTFSI/DMSO-based electrolyte, for which decomposition processes are observed by exponentially increasing positive currents at potentials ≥ 4.2 V vs. Li/Li⁺ (anodic scan, marked by (1) in Figure 4.15). This might be due to a decomposition of DMSO in the solvent mixture, as it is in good agreement with a study reporting DMSO₂ formation during galvanostatic cycling at potentials > 4.2 V[45]. For the pure DMSO-based electrolyte, however, such a strong current density increase is not

observed during anodic LSV. These observations indicate a negative influence of BMPTFSI on the stability of DMSO in the solvent mixture. During the cathodic LSV scans exponentially increasing *negative* currents at $E \leq 1.3$ V vs. Li/Li⁺ are observed for the BMPTFSI/DMSO-, pure DMSO- and MeCN-based electrolytes (marked by (2) in Figure 4.15).

Hence, the potential window of 1.3 V ... 4.2 V vs. Li/Li⁺ is the largest possible range for the electrochemical measurements with these electrolytes. The potentials were kept within a range of 1.7 V ... 4 V vs. Li/Li⁺ for the investigation of the ORR processes in this work. Thus, any decomposition of the aforementioned electrolytes during the measurements can be excluded in the discussion of the following sections.

The CV measurements recorded with the same O₂-saturated electrolytes at different scan rates are depicted in Figure 4.16 (see next page). Examples of the observed onset and peak potentials, E_{onset} and E_{peak} , are given in Figure 4.16.a for the MeCN-based electrolyte. The potential of reversible Li₂O₂ formation is indicated by the dashed grey line. An electrode rotational frequency of $\omega = 1000$ rpm was applied to enhance the reactant transport to and from the electrode surface. Nevertheless, a limitation of the observed ORR/OER processes by mass transport is observed for all electrolytes by significant shifts of the peak potentials E_{peak} in the negative (ORR) and the positive directions (OER) with increasing scan rate (see dotted grey arrows in Figure 4.16). This effect is caused by fast potential sweeps in systems with insufficient reactant transport properties to the reactive site, e.g., low Li⁺ ion mobility and/or O₂ solubility.

4.2.1. Electrolyte characterization

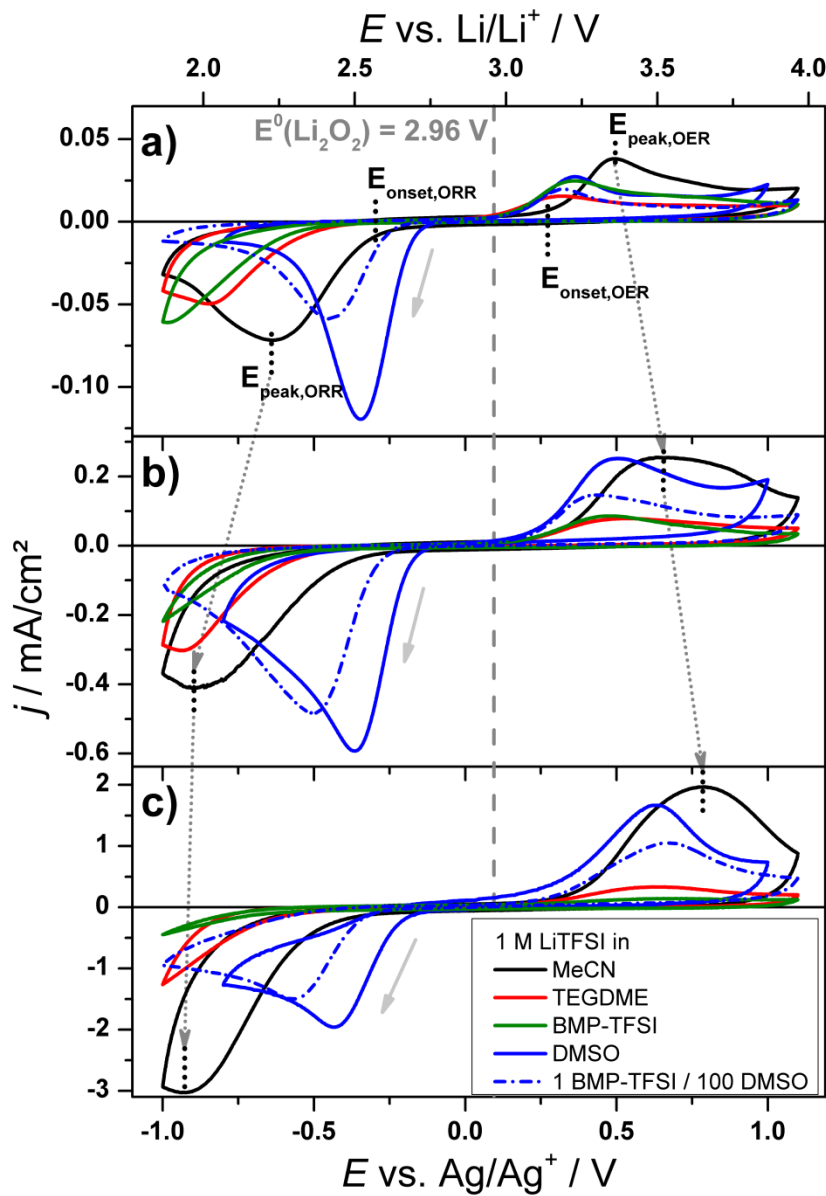


Figure 4.16: CV measurements recorded in different O_2 -saturated electrolytes. 1 M LiTFSI in: MeCN (black line), TEGDME (red line), BMPTFSI (green line), DMSO (blue line) and BMPTFSI/DMSO (1:100) (dotted blue line); scan rates ν : (a) 10 mV/s, (b) 100 mV/s and (c) 1000 mV/s; $\omega = 1000$ rpm; the dashed grey line denotes the reversible formation potential of Li_2O_2 E^0 [7]; in (a) examples for onset and peak potentials E_{onset} and E_{peak} are given for MeCN by dotted black lines; the shift of E_{peak} with increasing scan rates is indicated by dotted grey arrows.

Another result of fast potential sweeps is the increase of the cathodic current densities with the scan rate (compare scales of the y axes in

Figure 4.16), resulting from more reduction processes, which take place during the same period of measurement time. Furthermore, owing to the short scan time, the relatively slow *chemical* reactions of the ORR processes are suppressed in favor of the faster *reduction* processes, which leads to the detection of increasing current with increasing scan rates.

Table 4.4 (see next page) gives a summary of the ORR potentials and ORR/OER potential gaps observed for the various electrolytes at different scan rates. These potentials indicate the start of kinetically controlled reactions (E_{onset}) and the start of diffusion-controlled, i.e., mass transport-limited, potentials (E_{peak}). From these values a general trend of decreasing ORR potentials with increasing scan rate is observed for all electrolytes (see also dotted grey arrows in Figure 4.16). This is due to an insufficient reactant transport to the active electrode surface at high scan rates.

Regarding the different solvents, the DMSO-based electrolyte exhibits the highest ORR potentials, i.e., lowest overpotentials η , at every scan rate (highlighted yellow in Table 4.4). Furthermore, the smallest scan rate dependence of the ORR processes is observed for this solvent with a shift of E_{onset} and E_{peak} of about -0.06 V and -0.10 V, respectively, from 10 mV/s to 1000 mV/s. This indicates the best reactant transport properties of DMSO in comparison to all other solvents. The lowest ORR onset potentials are observed for the BMPTFSI-based electrolyte at every scan rate (highlighted grey in Table 4.4). For this solvent E_{peak} was not obtained at $E > 1.9$ V vs Li/Li⁺ during the CV measurements at any scan rate. This is proposed to be due to the high viscosity in combination with a too strong Li⁺ ion coordination by the large solvent anions, which decreases the Li⁺ ion mobility and leads to a limitation of the reactant transport to the reaction site.

4.2.1. Electrolyte characterization

Table 4.4: Comparison of the ORR potentials and ORR/OER potential gaps for the different electrolytes obtained from the CV measurements depicted in Figure 4.16. Important values concerning the discussion of the ORR processes are highlighted yellow (favorable) and grey (unfavorable).

ν / mV/s	1 M LiTFSI in	E_{onset} E vs. Li/Li ⁺ / V	E_{peak} E vs. Li/Li ⁺ / V	ΔE_{onset} / V	ΔE_{peak} / V
10	MeCN	2.52 ± 0.01	2.22 ± 0.01	0.62 ± 0.03	1.13 ± 0.03
	TEGDME	2.44 ± 0.02	2.02 ± 0.01	0.59 ± 0.03	1.16 ± 0.01
	BMPTFSI	2.42 ± 0.04	< 1.90	0.64 ± 0.08	-
	DMSO	2.69 ± 0.01	2.53 ± 0.01	0.36 ± 0.01	0.69 ± 0.01
	BMPTFSI/ DMSO (1:100)	2.62 ± 0.01	2.43 ± 0.01	0.40 ± 0.01	0.75 ± 0.01
100	MeCN	2.44 ± 0.01	1.98 ± 0.04	0.73 ± 0.03	1.48 ± 0.14
	TEGDME	2.37 ± 0.03	1.93 ± 0.01	0.75 ± 0.07	1.45 ± 0.05
	BMPTFSI	2.35 ± 0.03	< 1.90	0.75 ± 0.07	-
	DMSO	2.69 ± 0.02	2.43 ± 0.05	0.42 ± 0.02	0.95 ± 0.07
	BMPTFSI/ DMSO (1:100)	2.56 ± 0.01	2.36 ± 0.01	0.51 ± 0.01	0.93 ± 0.04
1000	MeCN	2.36 ± 0.05	1.94 ± 0.01	0.81 ± 0.14	1.58 ± 0.10
	TEGDME	2.27 ± 0.08	< 1.90	0.87 ± 0.11	-
	BMPTFSI	2.27 ± 0.05	< 1.90	1.01 ± 0.26	-
	DMSO	2.63 ± 0.01	2.43 ± 0.01	0.52 ± 0.03	1.00 ± 0.05
	BMPTFSI/ DMSO (1:100)	2.51 ± 0.01	2.29 ± 0.01	0.56 ± 0.08	1.12 ± 0.12

As a result of the highest scan rate dependence of E_{peak} (with a shift of more than -0.2 V from $\nu = 10$ mV/s to $\nu = 1000$ mV/s), which was obtained for TEGDME and MeCN (see dotted grey arrows in Figure 4.16), the ORR peak for the TEGDME-based electrolyte was not detected at $E > 1.9$ V during the CV measurement at $\nu = 1000$ mV/s. The ORR potentials obtained for the electrolyte based on BMPTFSI/DMSO are larger than those observed for the MeCN-, TEGDME- and BMPTFSI-based electrolytes, but lower than those

obtained for pure LiTFSI/DMSO. Hence, the addition of BMPTFSI to DMSO seems to have a negative impact on the ORR kinetics.

The ORR/OER peak and onset potential gaps ΔE_{peak} and ΔE_{onset} show a similar trend regarding the above discussion of the different electrolytes. Here, the DMSO-based electrolyte shows the best ORR/OER reversibility (highlighted yellow in Table 4.4), with ΔE being smaller by ≥ 0.28 V compared to those obtained for the MeCN-, TEGDME- and BMPTFSI-based electrolytes at all scan rates. The BMPTFSI/DMSO mixture exhibits ORR/OER reversibilities superior to those obtained for MeCN, TEGDME and pure BMPTFSI and comparable to those observed in DMSO-based electrolyte at high scan rates (highlighted yellow in Table 4.4). This result is surprising, as the largest scan rate dependence of the potential gaps, i.e., the least ORR/OER reversibility with increasing scan rates, is observed for the pure BMPTFSI-based electrolyte. As discussed before, this is most probably also due to the coordination of the Li^+ ions by the large TFSI anions, which limits the Li^+ ion mobility in the BMPTFSI solvent.

In conclusion, the DMSO-based electrolyte exhibits (i) the most favorable ORR kinetics due to the best reactant transport properties (based on the scan rate dependence of E_{onset} and E_{peak}) and (ii) the highest reversibility of the ORR/OER processes (based on the potential gaps ΔE). An addition of BMPTFSI to DMSO does not have the desired positive effect on the ORR kinetics and/or the ORR/OER reversibility, which is most probably due to a too low Li^+ ion mobility in the presence of BMPTFSI.

4.2.2. The impact of model electrode properties on the ORR processes

4.2.2. The impact of model electrode properties on the ORR processes

For a correct interpretation of the electrochemical measurements, the preparation of the electrodes is investigated in more detail. Therefore, the influence of Nafion[®], which was used as binder material for the preparation of the powder electrodes is discussed in this section.

Figure 4.17 (see next page) shows the influence of Nafion[®] on the ORR and OER processes by CV measurements recorded in O₂-saturated LiTFSI/DMSO at different scan rates without electrode rotation. Here, the results obtained with a Nafion[®]-coated GC disc (GC-N) are compared to those observed with an untreated GC electrode. An obvious influence of Nafion[®] on the ORR processes is observed at scan rates of 10 mV/s and 100 mV/s, at which lower current densities are obtained with GC-N. This is attributed to the insulating layer of Nafion[®] on the surface of the GC-N electrode. At an increased scan rate of 1000 mV/s the current densities of the reduction and oxidation processes are similar for both electrodes. This observation indicates that the electrode surface does not influence the number of transferred electrons during the reaction (j_{peak}). Hence, CV measurements recorded at large scan rates without electrode rotation detect reactant transport-limited ORR processes.

A comparison of the peak potentials E_{peak} shows that, whereas the ORR peaks observed for GC-N are located at lower potentials than those for GC, the OER peak potentials are comparable for both electrodes. Hence, the Nafion[®] binder only influences the ORR processes. At $\nu = 1000$ mV/s the difference between the ORR peak potentials for GC and GC-N is comparably small, which is another indication of a reaction limitation by a too slow mass transport to the electrode surface at large scan rates.

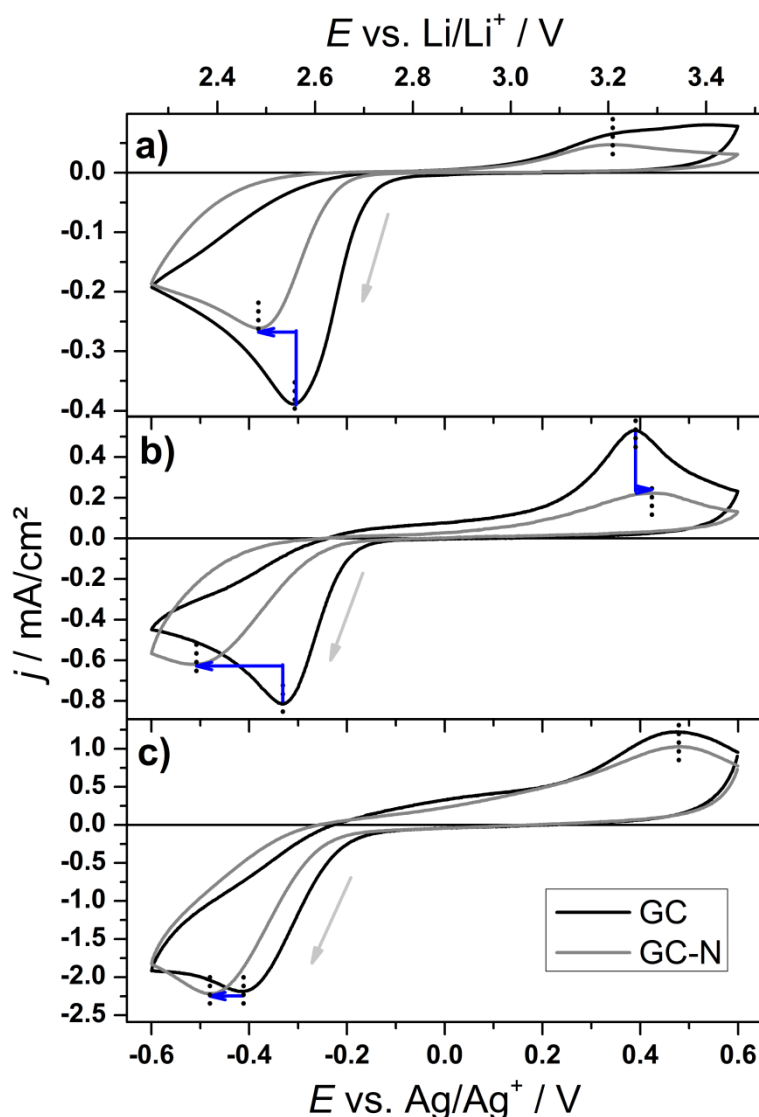


Figure 4.17: CV measurements recorded with GC and Nafion[®]-coated GC. GC (black) and Nafion[®]-coated GC (GC-N, grey); electrolyte: O₂-saturated 1 M LiTFSI/DMSO; $\omega = 0$ rpm; scan rates ν : (a) 10 mV/s, (b) 100 mV/s and (c) 1000 mV/s; dotted black lines denote peak potentials, blue arrows show the differences between the peak potentials of GC and GC-N.

Further data obtained from the CV are given in Table 4.5 (see next page). The onset potentials (E_{onset}) shown in Table 4.5 are relatively constant at all scan rates for both electrodes. However, E_{onset} for GC-N is significantly lower compared to those for GC at all scan rates. This is reflected in the apparent rate constants k_{app}^0 obtained for GC (highlighted yellow in Table 4.5), which

4.2.2. The impact of model electrode properties on the ORR processes

are seven- and threefold larger than those for GC-N at $\nu = 10$ mV/s and $\nu = 1000$ mV/s, respectively. Only at $\nu = 100$ mV/s the k_{app}^0 is twofold larger for GC-N (highlighted yellow in Table 4.5), which can be explained by the detection of different initial electron transfers indicated by the Tafel slopes at $\nu = 100$ mV/s.

The Tafel slope of 115 mV/dec obtained for GC (highlighted yellow in Table 4.5) is close to the theoretical value of an ideal electrode surface with 118 mV/dec for a one-electron transfer. A comparable Tafel slope was also presented in a recent study on the ORR in aprotic media and proposed to indicate a one-electron reduction of O_2 to LiO_2 , which is subsequently solvated by DMSO molecules[10].

Table 4.5: Comparison of ORR potentials and kinetic parameters for GC and GC-N. The data were obtained from Tafel plots of the CV measurements shown in Figure 4.17; important values concerning the discussion of the ORR activity and mechanism are highlighted yellow (favorable) and grey (unfavorable).

		10 mV/s	100 mV/s	1000 mV/s
E_{onset} vs. Li/Li ⁺ / V	GC	2.70 ± 0.01	2.67 ± 0.01	2.66 ± 0.01
	GC-N	2.64 ± 0.03	2.62 ± 0.01	2.63 ± 0.01
E_{peak} vs. Li/Li ⁺ / V	GC	2.56 ± 0.01	2.53 ± 0.01	2.46 ± 0.01
	GC-N	2.48 ± 0.03	2.37 ± 0.01	2.39 ± 0.01
Tafel slope / mV/dec	GC	88 ± 2	115 ± 1	164 ± 4
	GC-N	76 ± 1	171 ± 2	166 ± 2
αn	GC	0.67 ± 0.01	0.51 ± 0.01	0.36 ± 0.01
	GC-N	0.78 ± 0.01	0.35 ± 0.01	0.36 ± 0.01
$k_{\text{app}}^0 / 10^{-5}$ cm/s	GC	0.37 ± 0.01	0.54 ± 0.05	18.97 ± 0.13
	GC-N	0.05 ± 0.01	1.24 ± 0.04	6.18 ± 0.05

The Tafel slope of 171 mV/dec for GC-N is significantly larger at $\nu = 100$ mV/s (highlighted grey in Table 4.5). Possible explanations for this

observation are the detection of rate-determining electron transfers (i) through an oxide layer, (ii) preceding chemical steps or (iii) following chemical steps[49]. As this is only the case for GC-N and not for GC, the apparent rate constants k_{app}^0 at $\nu = 100$ mV/s describe activities for different ORR pathways and thus are hardly comparable.

The discussion of these results is continued below with the observations made in the Nicholson/Shain plots for GC and GC-N (see Figure 4.18).

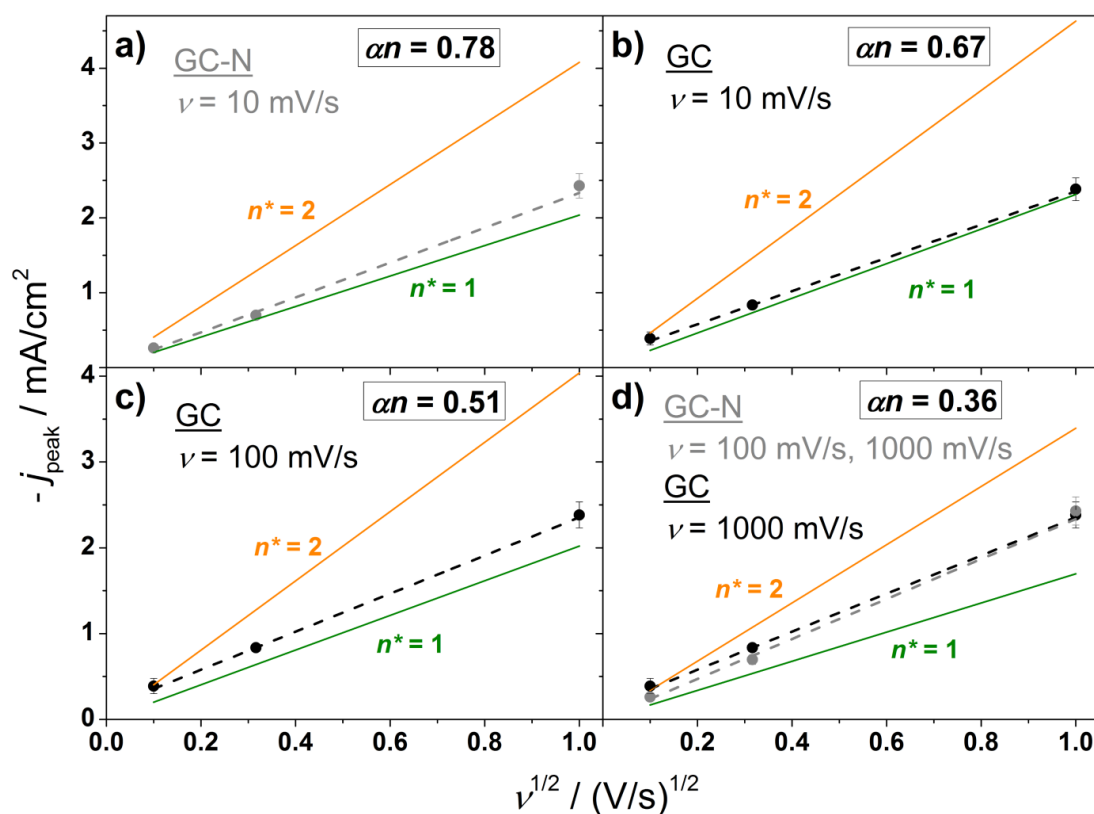


Figure 4.18: Nicholson/Shain plots for GC and GC-N. GC-N (grey circles) and GC (black circles); the plots show the influence of Nafion[®] on the rate limitation of the ORR processes (n^*) given in the respective diagrams; the different values of αn obtained from CV measurements on GC and GC-N at different scan rates are taken from Table 4.5.

From the Nicholson/Shain plots depicted in Figure 4.18 the n^* values – indicating the rate limitation of the ORR process – can be determined.

4.2.2. The impact of model electrode properties on the ORR processes

$\nu = 10$ mV/s. The very low Tafel slope of GC-N (76 mV/dec, highlighted grey in Table 4.5) points to the detection of consecutive two-electron transfers. The low current densities compared to those obtained for GC observed in the CV (see Figure 4.17.a) and the value of $n^* \approx 1.2$ from the Nicholson/Shain plot (see Figure 4.18.a) indicate the detection of a minor contribution of electron transfers with preceding chemical steps. Hence, the major part of the ORR is proposed to generate Li_2O_2 by reduction and chemical disproportionation of LiO_2 (eqs. (2.1)-(2.3)), whereas the dissociative mechanism yielding $[\text{LiO}]_{\text{n,ads}}$ species (eqs. (2.5)-(2.7)) only plays a minor role in the observed ORR processes.

For GC, the larger Tafel slope of 88 mV/dec compared to that obtained for GC-N (see Table 4.5) indicates less detection of two-electron transfers. The Nicholson/Shain plot gives $n^* = 1$ (see Figure 4.18.b), i.e., an ORR process with a fast electron transfer, which is not preceded by any chemical reactions. Hence, a Li_2O_2 formation from LiO_2 is also proposed to take place on GC at $\nu = 10$ mV/s, whereas the generation of $[\text{LiO}]_{\text{n,ads}}$ by the dissociative ORR mechanism observed for GC-N does not take place.

$\nu = 100$ mV/s. The Tafel slope of GC-N (171 mV/dec, highlighted grey in Table 4.5) as well as the low cathodic current densities observed in the CV (see Figure 4.17.b) indicate initial electron transfers including chemical steps. The Nicholson/Shain plot depicted in Figure 4.18.d (grey circles) gives $n^* \approx 1.4$, i.e., mixed diffusion-controlled and diffusionless ORR processes. This leads to the conclusion, that beside the O_2 reduction to LiO_2 and its further reduction (and chemical disproportionation) to Li_2O_2 (eqs. (2.1)-(2.3)), a dissociative adsorption of O_2 and the formation of $[\text{LiO}]_{\text{n,ads}}$ products (eqs. (2.5)-(2.7)) takes place on the surface of GC-N.

For GC the almost ideal Tafel slope of 115 mV/dec (highlighted yellow in Table 4.5) and the larger current densities in the CV (see Figure 4.17.b)

point to a formation of LiO_2 and a further reduction to Li_2O_2 (eqs. (2.1)-(2.2)). This assumption is confirmed by $n^* = 1$ obtained from the Nicholson/Shain plot (see Figure 4.18.c) indicating fast electron transfers and a diffusion control of the ORR processes. Also at this scan rate no formation of $[\text{LiO}]_{\text{n,ads}}$ species is detected.

$\nu = 1000 \text{ mV/s}$. For both electrodes – GC and GC-N – (i) comparable Tafel slopes of $\sim 165 \text{ mV/dec}$ indicate similar initial electron transfers (highlighted grey in Table 4.5), (ii) comparable current densities point to similar reactant transport limitations (see Figure 4.17.c) and (iii) similar n^* values of ~ 1.3 (GC) and ~ 1.4 (GC-N) show mixed diffusion-controlled and diffusionless ORR processes (see Nicholson/Shain plots in Figure 4.18.d). Hence, it is suggested that LiO_2 and Li_2O_2 (eqs. (2.1)-(2.3)) are generated next to $[\text{LiO}]_{\text{n,ads}}$ (eqs. (2.5)-(2.7)) on both electrodes. As this observation was already made for GC-N at $\nu = 100 \text{ mV/s}$, the Nafion[®] coating is proposed to increase the probability of the undesired $[\text{LiO}]_{\text{n,ads}}$ formation at low scan rates.

The results discussed in the above section show the formation of LiO_2 by an initial one-electron transfer on GC at $\nu = 100 \text{ mV/s}$. Therefore, further measurements were conducted at this scan rate, which is commonly used for CV measurements and thus allows comparison with data from the literature[10,52,55].

However, as the Nafion[®] binder was found to have a significant impact on the ORR kinetics and the ORR mechanism, the kinetic activities of the different $\text{Mn}_x\text{O}_y/\text{C}$ electrodes are hardly comparable to that of GC. Because commercially available Vulcan[®] carbon powder (VC) is used as substrate material for the catalytic investigations, pure VC/Nafion[®] electrodes are used as reference material in addition to GC for a better comparison of the electrocatalytic ORR activities investigated in sections 4.3 and 4.4.

4.2.3. The impact of electrode rotation on the ORR processes

4.2.3. The impact of electrode rotation on the ORR processes

The results discussed in the previous section showed that without electrode rotation at large scan rates the influence of the electrode surface on the ORR processes becomes negligible due to a mass transport limitation of the reactions. Therefore, the influence of the rotational frequency ω on the ORR processes observed during the CV measurements is investigated in this section. The rotational frequencies commonly used in the literature are around $\omega = 1000$ rpm. However, the powder electrodes used for the investigation of the catalytic activities of the manganese oxides in this work only allow the use of $\omega = 200$ rpm without any material leaching upon rotation. Therefore, CV measurements were conducted with GC electrodes at $\nu = 100$ mV/s with rotational frequencies of 0 rpm, 200 rpm and 1000 rpm. The potentials and parameters obtained from the Tafel plots of the CV measurements are summarized in Table 4.6.

Table 4.6: Potentials and kinetic parameters obtained from CV measurements recorded with a GC at $\nu = 100$ mV/s with different rotational frequencies. Important values concerning the discussion of the ORR activity and mechanism are highlighted yellow (favorable) and grey (unfavorable).

ω / rpm	$E_{\text{onset}} / \text{V}$	$E_{\text{peak}} / \text{V}$	Tafel slope / mV/dec	αn	$k_{\text{app}}^0 / 10^{-5} \text{ cm/s}$
0	2.67 ± 0.01	2.53 ± 0.01	115 ± 1	0.51 ± 0.01	0.54 ± 0.01
200	2.77 ± 0.03	2.56 ± 0.03	104 ± 2	0.57 ± 0.02	3.30 ± 2.14
1000	2.79 ± 0.02	2.43 ± 0.05	109 ± 3	0.54 ± 0.02	6.40 ± 1.62

The data given in Table 4.6 show the influence of the rotational frequency on the parameters of the ORR processes observed during CV measurements. Here, a by ca. 0.12 V lower onset potential E_{onset} is observed with $\omega = 0$ rpm (highlighted grey in Table 4.6) in comparison to that obtained with

$\omega = 1000$ rpm (highlighted yellow in Table 4.6), which is the rotational frequency commonly used for CV studies. Hence, the activity of comparable electrode surfaces (i.e., comparably active electrodes) seems lower, when the electrode is not rotated, i.e., the reactant transport is not enhanced. This is reflected in the by one order of magnitude smaller apparent reaction rate constant k_{app}^0 obtained during the measurement with $\omega = 0$ rpm (highlighted grey in Table 4.6) compared to that calculated for $\omega = 1000$ rpm (highlighted yellow in Table 4.6).

The CV recorded with $\omega = 200$ rpm, on the other hand, results in E_{onset} and k_{app}^0 values, which are comparable to those obtained with $\omega = 1000$ rpm. As the results of the CV measurements without electrode rotation (highlighted grey in Table 4.6) are considerably influenced by the mass transport limitation, the discussion of the impact of the rotational frequency will be continued only for the measurements conducted with electrode rotation.

The αn values given in Table 4.6 were used for Nicholson/Shain plots to determine the rate limitation of the ORR processes observed with rotational frequencies of $\omega = 200$ rpm and $\omega = 1000$ rpm (see Figure 4.19 on the next page).

The Nicholson/Shain plot for GC with $\omega = 1000$ rpm is depicted in Figure 4.19.a. Here, a value of $n^* = 1$ for a fast electron transfer is observed indicating a diffusion-controlled formation of LiO_2 and Li_2O_2 compounds (eqs. (2.1)-(2.3)). This was also reported by Laoire *et al.* with $\alpha = 0.5$ for a one-electron transfer ($n = 1$), during CV measurements with GC under the same reaction conditions[10].

Figure 4.19.b depicts the Nicholson/Shain plot for GC with $\omega = 200$ rpm, from which also a diffusion control of the ORR processes is observed with $\alpha = 0.57$, $n = 1$ and $n^* = 1$.

4.2.3. The impact of electrode rotation on the ORR processes

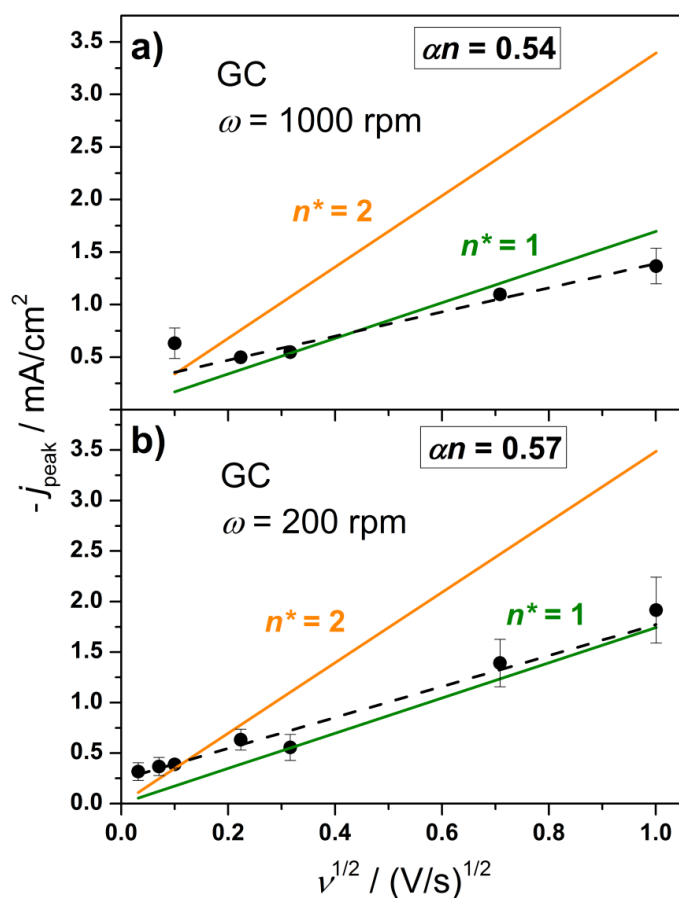


Figure 4.19: Nicholson/Shain plots for GC with (a) $\omega = 1000$ rpm and (b) $\omega = 200$ rpm. The plots show the influence of the rotational frequency on the rate-determining factor of the ORR (given by n^*); the different values of αn obtained from CV measurements at $\nu = 100$ mV/s are taken from Table 4.6.

In summary, the electrochemical results obtained with a rotational frequency of 200 rpm used for the investigations of the electrocatalytic ORR activities of the Mn_xO_y compounds are proposed to be comparable to those reported in literature CV studies using $\omega = 1000$ rpm.

4.2.4. Conclusion

LiTFSI/DMSO is the electrolyte of choice for the CV investigations of the electrocatalytic ORR activities presented in the next section. Compared to other electrolyte solvents, DMSO shows (i) good electrochemical stability in the required potential window, (ii) the most favorable ORR kinetics and (iii) the best efficiency regarding the ORR/OER overpotentials.

Different reaction mechanisms were deduced from CV measurements for GC and Nafion[®]-coated GC (GC-N), which showed a considerable influence of the Nafion[®] binder used for powder electrode preparation on the observed ORR processes. Therefore, GC and additionally Vulcan[®] carbon powder (VC, which also serves as substrate material for the Mn_xO_y catalysts) are used as reference materials for the discussion of the ORR processes observed for the Mn_xO_y/C electrodes.

Further CV measurements showed that the application of the maximum rotational frequency for the use of Mn_xO_y/C and VC powder electrodes ($\omega = 200$ rpm) and the rotational frequency commonly used in the literature ($\omega = 1000$ rpm) result in comparable ORR activities and mechanisms. This allows a relation of the measurements presented in the next sections to data from the literature.

4. Results & Discussion

4.3. The effect of the Mn_xO_y catalysts on the ORR processes

This section presents the investigation of the electrocatalytic ORR activities of the Mn_xO_y compounds by CV measurements. These were conducted with 10wt% Mn_xO_y /carbon powder electrodes in 1 M LiTFSI/DMSO with a rotational frequency of $\omega = 200$ rpm in a potential range of 2.2 V ... 3.9 V vs. Li/Li⁺. The ORR activities (obtained from the onset and peak potentials observed in the CV as well as from the kinetic evaluation of the Tafel plots) are compared to those of the carbon reference materials GC and Vulcan[®] carbon powder (VC). The CV measurements were recorded with a scan rate of $\nu = 100$ mV/s, which is fast enough to detect both, the (potential-dependent) electrochemical and (time-dependent) chemical formation of the desired Li₂O₂ product from LiO₂.

As most of the research on catalysts for the Li/air system is done by galvanostatic cycling, from which mechanistic insight can only be obtained by simultaneous *in situ* detection of the products, e.g., *in situ*-DEMS or -IR spectroscopy, information about the ORR processes generating these products is rare. Here, a discussion of the ORR mechanisms concluded from the CV measurements gives further insight into the origins of the kinetic activities of the different electrode materials. This chapter contains results already published elsewhere[135].

4.3.1. The ORR activities at a scan rate of 100 mV/s

The potential scan rate of 100 mV/s is the scan rate commonly used for CV measurements in aqueous systems and was most recently used in a study on noble metal catalysts in Li⁺/DMSO[52,55]. This section investigates the ORR activities of the Mn_xO_y catalysts by CV measurements recorded at

4.3.1. The ORR activities at a scan rate of 100 mV/s

$\nu = 100$ mV/s. Examples of cyclic voltammograms are shown in Figure 4.20 comparing the 10wt% $\text{Mn}_x\text{O}_y/\text{C}$ electrodes to the GC and VC reference materials.

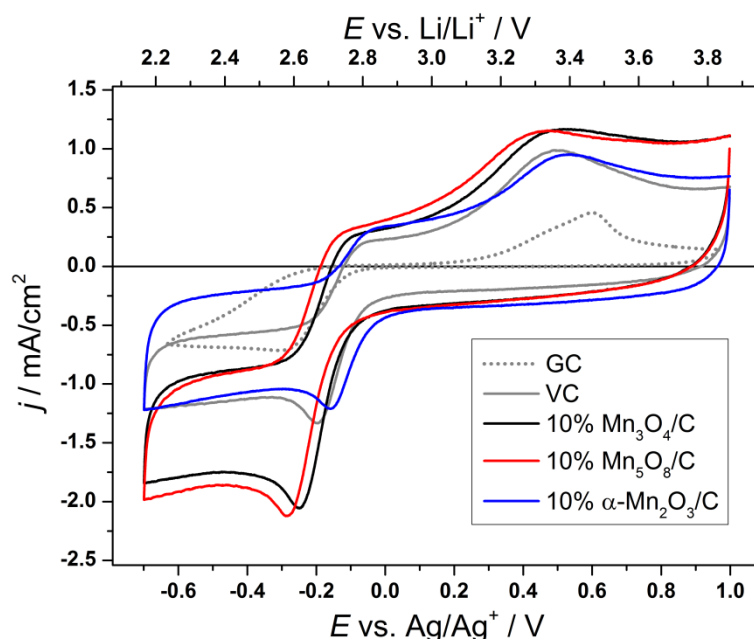


Figure 4.20: CV measurements recorded with different working electrodes. GC (dotted grey line), VC (solid grey line) as well as 10wt% catalyst/C powder mixture electrodes of Mn_3O_4 (black line), Mn_5O_8 (red line) and $\alpha\text{-Mn}_2\text{O}_3$ (blue line); $\nu = 100$ mV/s; $\omega = 200$ rpm.

It has to be mentioned here, that the discussion of the catalytic activities will be done on the basis of the peak and onset potentials. The obtained current densities strongly depend on the composition of the electrode surface. In general, it is likely that the different particle diameters of the Mn_xO_y catalysts result in different electrode compositions. This, however, has no influence on the potentials, as the presented CV curves exhibit similar behavior regarding the ORR as well as the OER processes (see Figure 4.20). The ORR peak potentials for all electrodes are observed in a potential range from 2.5 V to 2.8 V vs. Li/Li^+ . The OER peaks for all electrodes are observed at potentials ranging from 3.3 V to 3.5 V vs. Li/Li^+ (see Figure 4.20), which

is within the potential range for Li_2O_2 oxidation in aprotic media[10,43,136]. Considering the used electrolyte (LiTFSI/DMSO), a decomposition of DMSO can be excluded, as DMSO_2 formation is proposed to take place at potentials $> 4 \text{ V vs. Li/Li}^+$ [45]. A summary of the ORR onset and peak potentials for the different electrode materials is given in Table 4.7.

Table 4.7: ORR peak and onset potentials for the different electrode materials obtained from the CV measurements recorded at $\nu = 100 \text{ mV/s}$. The increased ORR potentials for $\alpha\text{-Mn}_2\text{O}_3/\text{C}$ are highlighted yellow.

	E_{peak}	E_{onset}
	$E \text{ vs. Li/Li}^+ / \text{V}$	
GC	2.56 ± 0.03	2.76 ± 0.03
VC	2.65 ± 0.04	2.78 ± 0.04
$\text{Mn}_3\text{O}_4/\text{C}$	2.57 ± 0.10	2.71 ± 0.10
$\text{Mn}_5\text{O}_8/\text{C}$	2.65 ± 0.04	2.78 ± 0.04
$\alpha\text{-Mn}_2\text{O}_3/\text{C}$	2.74 ± 0.05	2.87 ± 0.06

Table 4.7 shows the onset and peak potentials E_{onset} and E_{peak} for $\alpha\text{-Mn}_2\text{O}_3/\text{C}$, which are significantly larger by $\geq 0.09 \text{ V}$ compared to those obtained for the other electrode materials (highlighted yellow in Table 4.7). This indicates a considerably increased ORR activity. Whereas $\text{Mn}_5\text{O}_8/\text{C}$ shows no change of the potentials with respect to pure VC, the presence of the Mn_3O_4 catalyst seems to be counterproductive regarding the ORR activity, as the obtained potentials are lower by $\geq 0.07 \text{ V}$ compared to those for VC.

The reversibility of the ORR process is discussed for the different electrode materials based on the values given in Table 4.8 (see next page).

The impact of carbon powder on the ORR/OER reversibility is observed from the decreased ORR/OER onset and peak potential gaps ΔE_{onset} and

4.3.1. The ORR activities at a scan rate of 100 mV/s

ΔE_{peak} in the presence of VC substrate (see Table 4.8). The potential gaps are smaller by ≥ 100 mV for the VC-based electrodes compared to those for GC (highlighted grey in Table 4.8). In addition, the re-oxidation efficiencies $Q_{\text{OER}}/Q_{\text{ORR}}$ obtained from the electric charges of the ORR and OER peaks are increased from $< 50\%$ for GC (highlighted grey in Table 4.8) to significantly higher values of $> 70\%$ for all VC-containing electrodes. These results demonstrate the increased ORR/OER efficiency of carbon powder compared to the smooth GC surface, which is attributed to the larger active area of the VC substrate, whose porous character results in more active sites.

Table 4.8: ORR/OER potential differences and electric charge ratios for the different electrode materials obtained from the CV measurements recorded at $\nu = 100$ mV/s. The values indicating a low ORR/OER reversibility for GC are highlighted grey.

	$\Delta E_{\text{peak}} / \text{V}$	$\Delta E_{\text{onset}} / \text{V}$	$Q_{\text{OER}}/Q_{\text{ORR}} / \%$
GC	0.88 \pm 0.04	0.43 \pm 0.02	47 \pm 24
VC	0.73 \pm 0.03	0.30 \pm 0.01	77 \pm 21
Mn ₃ O ₄ /C	0.78 \pm 0.04	0.31 \pm 0.02	74 \pm 13
Mn ₅ O ₈ /C	0.74 \pm 0.03	0.30 \pm 0.02	73 \pm 17
α -Mn ₂ O ₃ /C	0.73 \pm 0.04	0.30 \pm 0.01	79 \pm 11

Compared to data from the literature, the charge efficiencies $Q_{\text{ORR}}/Q_{\text{OER}}$ for the GC ($\sim 47\%$) and VC electrodes ($\sim 77\%$) are very close to those obtained during galvanostatic recharges of a carbon substrate electrode in LiTFSI/DMSO (51%) and a VC electrode in a DME-based electrolyte (78%)[12,20]. Furthermore, the charge efficiency of 69% for a VC-supported Au catalyst obtained during galvanostatic cycling in a DME-based electrolyte[20] is comparable to those for all VC-based electrodes investigated in this section (see Table 4.8).

For the investigation of the kinetic ORR activities the Tafel plots of the CV measurements were evaluated for the different electrode materials. Examples of the linear Tafel regions at overpotentials $\eta = -0.10 \text{ V} \dots -0.30 \text{ V}$ are depicted in Figure 4.21.

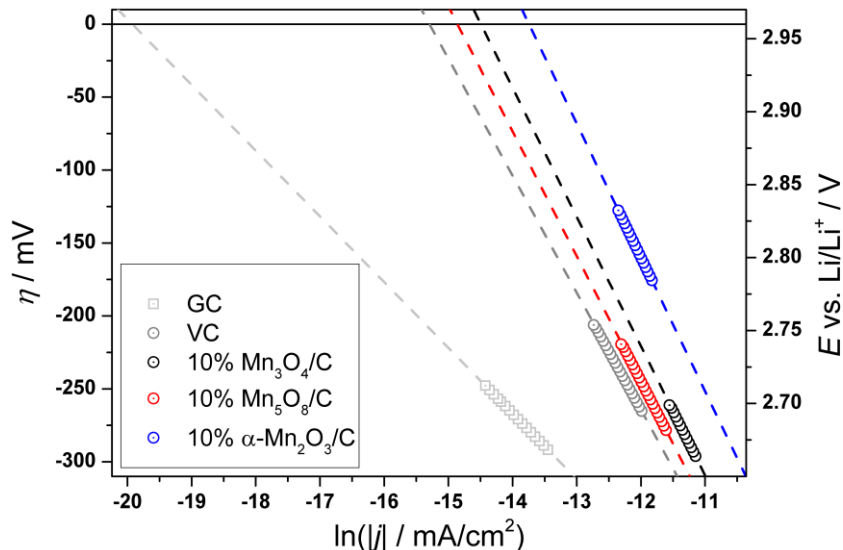


Figure 4.21: Representative Tafel plots for different working electrodes. The diagram shows the overpotential range from -0.10 V to -0.30 V , to which the respective linear Tafel slopes were fitted (indicated by dashed lines); GC (light grey), VC (dark grey), $\text{Mn}_3\text{O}_4/\text{C}$ (black), $\text{Mn}_5\text{O}_8/\text{C}$ (red) and $\alpha\text{-Mn}_2\text{O}_3/\text{C}$ (blue).

The partial current densities j_0 obtained from the intercept of the linear Tafel fit with $\eta = 0 \text{ V}$ are listed in Table 4.9 for the different electrode materials (see next page). From j_0 the apparent reaction rate constants k_{app}^0 for the initial electron transfers of the ORR were determined by eq. (2.11); a value of $C_{\text{O}_2} = 2.1 \cdot 10^{-6} \text{ mol/cm}^3$ (the solubility of O_2 in DMSO) was used according to the literature[10,55,137].

Table 4.9 shows the partial current densities j_0 and the apparent rate constants k_{app}^0 for the different electrode materials. All electrodes exhibit k_{app}^0 values between 10^{-5} cm/s and 10^{-3} cm/s , which identifies the observed ORR processes as quasireversible[52]. Here, GC shows a k_{app}^0 value (highlighted

4.3.1. The ORR activities at a scan rate of 100 mV/s

grey in Table 4.9) within the same order of magnitude as the one reported by Laoire *et al.* for the ORR in a Li⁺/MeCN electrolyte[9].

Table 4.9: Partial current densities j_0 and apparent reaction rate constants k_{app}^0 for the different electrode materials obtained from the CV recorded at $\nu = 100$ mV/s. Values concerning the discussion of the ORR activity are highlighted yellow (favorable) and grey (unfavorable).

	$j_0 / \mu\text{A}/\text{cm}^2$	$k_{\text{app}}^0 / 10^{-5} \text{ cm/s}$
GC	6.68 ± 4.34	3.30 ± 2.14
VC	160.5 ± 81.6	79.2 ± 40.2
Mn ₃ O ₄ /C	182.7 ± 95.4	90.2 ± 47.1
Mn ₅ O ₈ /C	192.0 ± 56.4	94.8 ± 27.8
α -Mn ₂ O ₃ /C	373.3 ± 79.4	184.2 ± 39.2

Among the carbon powder-containing electrodes only α -Mn₂O₃/C shows a significant increase of k_{app}^0 , i.e., a larger activity for the initial electron transfer of the ORR (highlighted yellow in Table 4.9). Mn₃O₄/C and Mn₅O₈/C show activities, which are comparable to that obtained for pure VC. An increase of the ORR activity for α -Mn₂O₃/C was already deduced from the increased onset and peak potentials (see Table 4.7).

The investigation of the ORR mechanisms resulting in the different activities of the respective electrode materials is presented in the next section.

4.3.2. The ORR mechanisms at a scan rate of 100 mV/s

For the investigation of the ORR mechanism, the “cathodic quantities” αn [47], which consist of the charge transfer coefficient α and the number of electrons transferred during the rate-determining step n , were calculated from the Tafel slopes depicted in Figure 4.21 by eq. (2.10). The values of the Tafel slopes and αn for the different electrode materials are given in Table 4.10. The αn value obtained for GC is 0.57, which was already discussed in section 4.2.3. For the VC-based electrodes αn values of about 0.3 were obtained (see Table 4.10), which is an indication for a comparable decrease of the energy barriers of the initial electron transfers by all VC-based materials.

Table 4.10: Tafel slopes and αn values derived thereof for the different electrode materials obtained from the CV recorded at $\nu = 100$ mV/s. The values closest to the ideal values for a one-electron transfer for GC are highlighted yellow; for a further discussion, see text.

	Tafel slope / mV/dec	αn
GC	103.8 \pm 2.3	0.57 \pm 0.02
VC	185.3 \pm 21.0	0.32 \pm 0.04
Mn ₃ O ₄ /C	204.3 \pm 16.0	0.29 \pm 0.02
Mn ₅ O ₈ /C	198.7 \pm 19.1	0.30 \pm 0.03
α -Mn ₂ O ₃ /C	223.2 \pm 51.9	0.28 \pm 0.06

Table 4.10 shows the Tafel slope values for the different electrode materials. The Tafel slope obtained for GC (highlighted yellow) has already been discussed in section 4.2.3. For the VC-based electrodes Tafel slope values considerably larger compared to that for GC are observed. As mentioned before, these can be attributed to electron transfers (i) through an oxide layer, (ii) with preceding or (iii) with subsequent chemical steps.

4.3.2. The ORR mechanisms at a scan rate of 100 mV/s

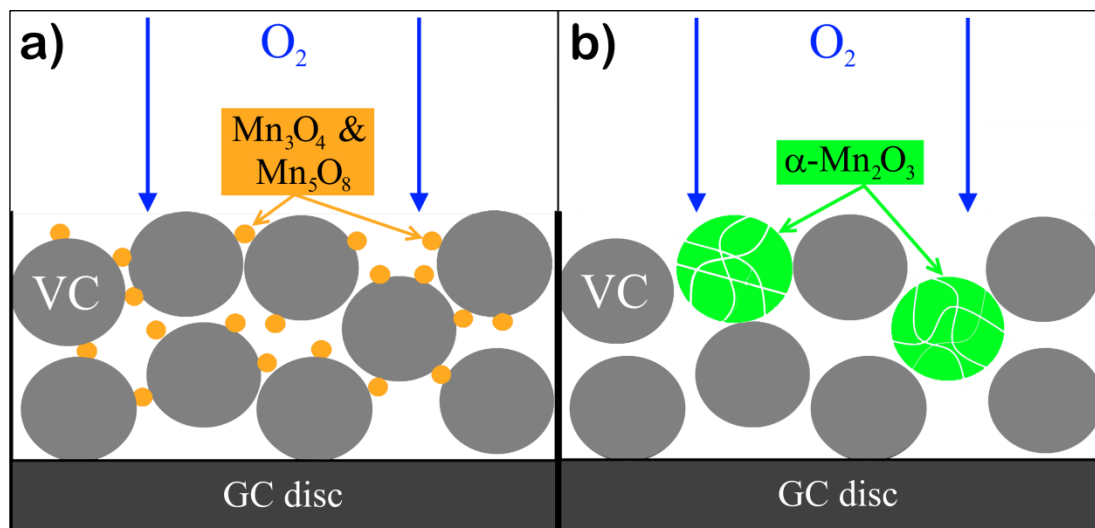
Hence, the increased Tafel slopes obtained for the VC-containing electrodes indicate a different mechanism of the rate-determining electron transfer. The increased ORR activity of the VC substrate discussed in the previous section will lead to a fast accumulation of Li_xO_y intermediates and/or final products on the electrode surface. Therefore, the considerably larger Tafel slopes are most probably the result of initial electron transfers through oxide layers.

Furthermore, the larger active surface of the porous VC and the presence of more reactive sites, e.g., kinks and edges, in contrast to the smooth GC surface have to be considered. Here, the model proposed by Dathar *et al.* can be applied[19]. GC with its relatively low oxygen adsorption strength and the absence of active adsorption sites will exhibit the one-electron reduction of O_2 to LiO_2 as rate-determining step (rds) with a subsequent formation of Li_2O_2 (eqs. (2.1)-(2.3)), as was already suggested in several studies[19,23,28]. The larger number of active sites on the VC-based electrode surfaces, on the other hand, might lead to the alternate reaction pathway, which results in the formation of $[\text{LiO}]_{n,\text{ads}}$ species (eqs. (2.5)-(2.7))[19,138].

Increasing Tafel slopes were found by Calegario *et al.* for carbon electrodes with increasing catalyst loadings during an investigation of the ORR processes in aqueous media and attributed to the low conductivities of the Mn_xO_y catalysts[139]. Considering this aspect, an additional reason for the large Tafel slopes obtained for the VC-based electrodes might be the significantly lower electric conductivities σ of the materials used for powder electrode preparation in comparison to that of GC ($180 (\Omega\cdot\text{cm})^{-1}$ [140]): Nafion[®] ($\leq 0.1 (\Omega\cdot\text{cm})^{-1}$ [141]), VC ($4.5 (\Omega\cdot\text{cm})^{-1}$ [142]) and especially the Mn_xO_y catalysts ($10^{-7} - 10^{-5} (\Omega\cdot\text{cm})^{-1}$, see Table 4.3 for the respective bulk conductivities of the Mn_xO_y compounds).

Furthermore, recent reports about catalysts for the ORR in aqueous media attribute small Tafel slopes to an increased participation of the VC support

in the observed ORR processes[143,144]. The Tafel slopes of the VC-based electrodes given in Table 4.10 might be influenced to a certain degree by this effect, which is discussed below based on the idealized model of the powder electrodes depicted in Scheme 4.1.



Scheme 4.1: Idealized model for the investigated Mn_xO_y/C electrodes.

From Scheme 4.1 it becomes apparent, that for a discussion of the ORR mechanisms taking place on the electrode surfaces, the different catalyst and VC particle diameters have to be considered: In the Mn_xO_y/C electrodes the VC particles ($d = 0.8 - 9 \mu\text{m}$)[145] will have less contact to the $\alpha\text{-Mn}_2\text{O}_3$ particles of comparable sizes ($d = 0.5 - 2 \mu\text{m}$, see Scheme 4.1.b) than to the nanometer-sized Mn_3O_4 and Mn_5O_8 catalysts (see Scheme 4.1.a). In good agreement to this assumption, the Tafel slope obtained for $\alpha\text{-Mn}_2\text{O}_3/C$ ($\sim 223 \text{ mV/dec}$) shows the largest difference with respect to that of VC ($\sim 185 \text{ mV/dec}$). The Tafel slopes for the Mn_xO_y/C electrodes with nanosized catalyst particles are considerably closer to that for VC (Mn_3O_4/C ($\sim 204 \text{ mV/dec}$) and Mn_5O_8/C ($\sim 199 \text{ mV/dec}$)). Here, the small diameters of the Mn_3O_4 and Mn_5O_8 nanoparticles result in a large

4.3.2. The ORR mechanisms at a scan rate of 100 mV/s

catalyst/carbon contact area and thus an increased contribution of the VC substrate to the ORR processes.

In addition, the conductivity of the α -Mn₂O₃/C electrode will be considerably influenced by the large α -Mn₂O₃ particles due to less α -Mn₂O₃ – VC particle contact, which additionally leads to a further increase of the Tafel slope for α -Mn₂O₃/C compared to that for pure VC (see Table 4.10).

As the k_{app}^0 values given in Table 4.9 indicate quasireversible reactions for all electrode materials, eq. (2.12) could be applied, which describes the Nicholson/Shain relationship of current density and scan rate. The resulting plots (see Figure 4.22) exhibit the rate limitation of the ORR processes n^* [9,10,27,59]. For this evaluation, the αn values calculated from the Tafel slopes were used; the diffusion coefficient of O₂ in Li⁺/DMSO ($D_{O_2} = 1.67 \cdot 10^{-5}$ cm²/s) was taken from the literature[10].

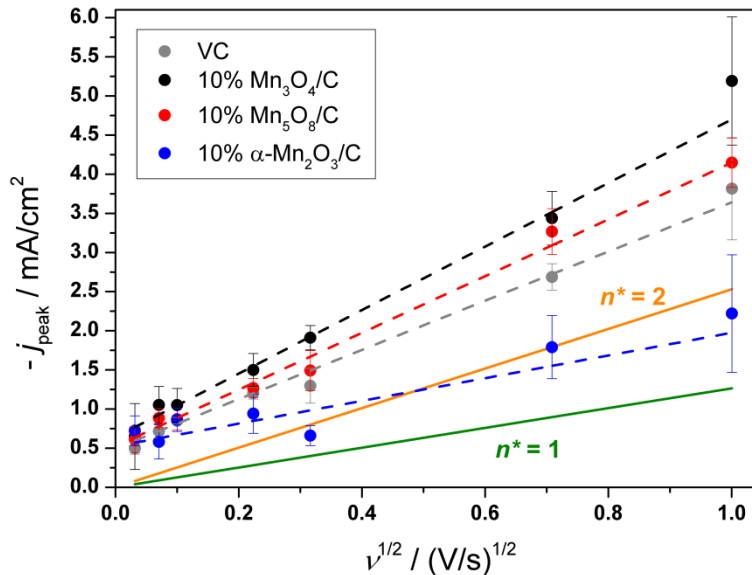


Figure 4.22: Nicholson/Shain plots for the VC-based electrodes. VC (grey), Mn₃O₄/C (black), Mn₅O₈/C (red) and α -Mn₂O₃/C (blue) with $\alpha n = 0.3$ indicating the rate limitation of the ORR mechanism by the value of n^* .

The Nicholson/Shain plot for GC (presented in section 4.2.3) revealed a diffusion-controlled process with $n^* = 1$ (see Figure 4.19). That result supported the assumption of LiO_2 formation by a fast initial electron transfer, which was already proposed by Calvo *et al.* based on RRDE measurements in a similar electrolyte[28].

The Nicholson/Shain plots of the VC-based electrodes with $\alpha n = 0.3$ (obtained from the Tafel slopes) are depicted in Figure 4.22. An indication for the presence of chemical steps in the ORR processes is observed for all VC-containing electrodes. According to eq. (2.12) the peak current densities at the intercept $v^{1/2} = 0$ (V/s)^{1/2} should equal zero. Here, however, the linear regressions of all electrode materials show values of $j_{\text{peak}} > 0$ mA/cm^2 , which indicates electron transfers including chemical processes[146].

For pure VC a value of $n^* = 2$ is obtained, indicating an ORR process, which is not hindered by diffusion and/or preceded by a chemical reaction. Hence, the carbon reference materials GC and VC are active for different ORR pathways, which was already suggested for the initial electron transfers based on the Tafel slopes.

The Nicholson/Shain plots for the different $\text{Mn}_x\text{O}_y/\text{C}$ electrodes (see Figure 4.22) exhibit $n^* = 2$ in the presence of the Mn_3O_4 and Mn_5O_8 compounds. Both catalysts therefore do not influence the reaction mechanism observed for VC, which might be due to the large contribution of the VC substrate to the ORR process (resulting from large catalyst/carbon contact areas) as discussed previously.

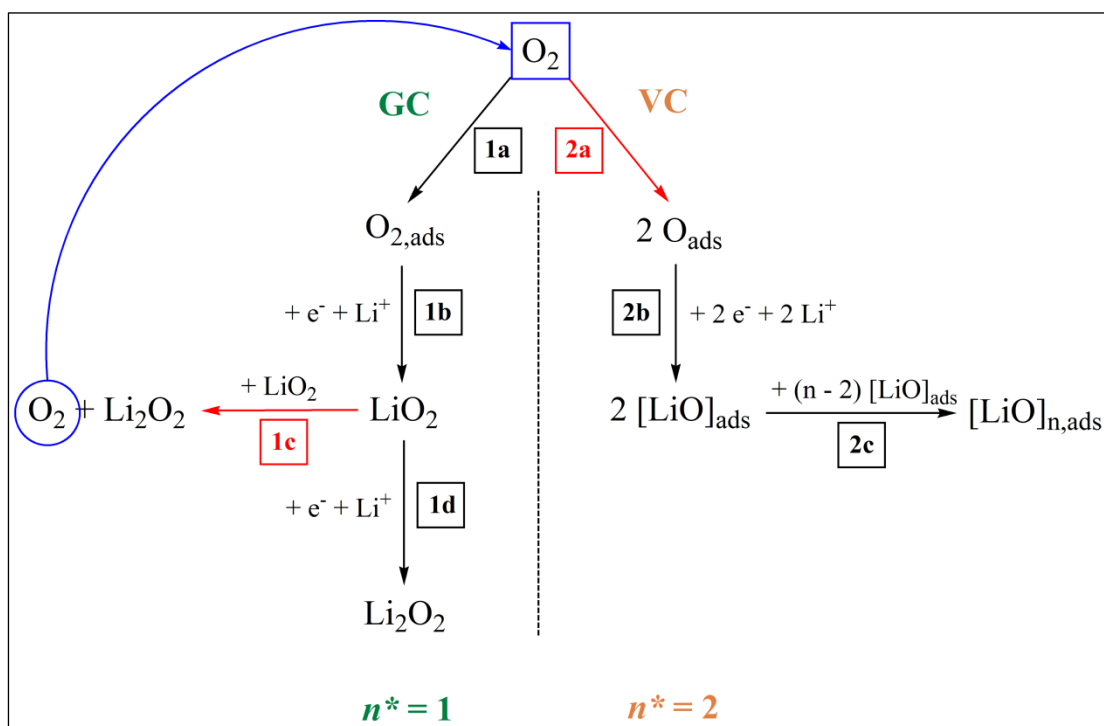
For $\alpha\text{-Mn}_2\text{O}_3/\text{C}$ a value of $n^* = 1$ is observed from the Nicholson/Shain plot (see Figure 4.22). This value corresponds to a diffusion-controlled ORR mechanism, i.e., a fast electron transfer limited by reactant diffusion to the active electrode surface. Here, the ORR mechanism observed for VC is changed in the presence of $\alpha\text{-Mn}_2\text{O}_3$.

4.3.2. The ORR mechanisms at a scan rate of 100 mV/s

The different ORR mechanisms suggested for the different electrode materials will be discussed in more detail below.

4.3.2.1. The ORR processes on the carbon electrode surfaces

The ORR mechanisms suggested for the two carbon reference materials based on the findings from the Tafel and Nicholson/Shain plots are depicted in Scheme 4.2.



Scheme 4.2: Different ORR mechanisms detected for different working electrodes at $v = 100 \text{ mV/s}$. Chemical reactions, which can be deduced from the CV measurements, are given in red; for a further discussion, see text.

The increased Tafel slopes obtained for the VC-based electrodes can be attributed to chemical steps preceding or following the one-electron transfer. As both, the Tafel slope and the Nicholson/Shain plot for VC indicate

possible chemical reactions involved in the ORR, pure VC is suggested to promote the ORR mechanism *via* dissociative chemisorption of O_2 with a subsequent reduction to $[LiO]_{n,ads}$ species (rcts. 2a-2c in Scheme 4.2). Thus, VC shows a CE mechanism, i.e., a pathway of subsequent chemical and electrochemical steps, which results in a kinetic limitation of the electron transfer by the reaction rate of the chemical O_2 dissociation[48].

For the GC electrode, on the other hand, an ORR pathway resulting in the generation of LiO_2 and Li_2O_2 is proposed (rcts. 1a-1d in Scheme 4.2).

Further indications for different ORR mechanisms taking place on the active surfaces of the carbon reference materials are obtained by a comparison of the ORR potentials and kinetic parameters observed during CV measurements with $\omega = 0$ rpm to those obtained with $\omega = 200$ rpm (see Table 4.11). The parameters of the diffusion-controlled ORR processes proposed for GC should be considerably influenced by the absence of reactant transport ($\omega = 0$ rpm). The ORR activity of VC for diffusionless processes, on the other hand, should be comparable with and without rotation of the electrode.

Table 4.11: Potentials and kinetic parameters for GC and VC at $\nu = 100$ mV/s with $\omega = 0$ rpm and $\omega = 200$ rpm. Important values concerning the discussion of the ORR mechanism and activity are highlighted yellow and grey, respectively; for a further discussion, see text.

	<i>GC</i>		<i>VC</i>	
	0 rpm	200 rpm	0 rpm	200 rpm
E_{onset} vs. Li/Li ⁺ / V	2.67 ± 0.01	2.77 ± 0.03	2.67 ± 0.10	2.78 ± 0.04
Tafel slope / mV/dec	115 ± 1	104 ± 2	185 ± 24	185 ± 21
αn	0.51 ± 0.01	0.57 ± 0.02	0.32 ± 0.04	0.32 ± 0.04
k_{app}^0 / 10 ⁻⁴ cm/s	0.05 ± 0.00	0.33 ± 0.21	3.1 ± 2.3	7.9 ± 4.0

4.3.2. The ORR mechanisms at a scan rate of 100 mV/s

The αn values obtained for VC and GC with $\omega = 0$ rpm (highlighted yellow in Table 4.11) are comparable to those obtained with $\omega = 200$ rpm, i.e., the decrease of the energy barriers for the initial electron transfers by both carbon materials is comparable with and without electrode rotation.

As expected, the onset potentials E_{onset} obtained for GC with $\omega = 0$ rpm are significantly lower compared to those obtained with enhanced reactant transport. This is reflected in the by one order of magnitude lower apparent rate constant k_{app}^0 with $\omega = 0$ rpm (highlighted grey in Table 4.11). Here, the limited reactant transport shows a considerable negative influence on the kinetics of GC for the diffusion-controlled ORR processes.

Although a comparable decrease of E_{onset} without electrode rotation is observed for VC (highlighted grey in Table 4.11), the mean value of k_{app}^0 for the diffusionless ORR processes is reduced only by about 60% compared to the value obtained with $\omega = 200$ rpm.

4.3.2.2. The ORR processes in the presence of $\alpha\text{-Mn}_2\text{O}_3$

For $\alpha\text{-Mn}_2\text{O}_3/\text{C}$ a diffusion-controlled ORR mechanism was deduced from $n^* = 1$ observed in the Nicholson/Shain plot (see Figure 4.22), which indicates an ORR mechanism comparable to that taking place on the surface of GC rather than VC. This observation can be explained by the porous character of the catalyst and thus a large concentration of coordinatively unsaturated Mn^{3+} surface ions. Several publications on Mn_2O_3 and MnOOH catalysts for the ORR in aqueous media proposed that O_2 is associatively adsorbed on the Mn_xO_y catalyst surfaces. These $\text{O}_{2,\text{ads}}$ species are subsequently reduced accompanied by a simultaneous oxidation of surface Mn^{3+} to Mn^{4+}

ions[143,147,148], which is also proposed here to take place in aprotic media on the α -Mn₂O₃ catalyst surface:

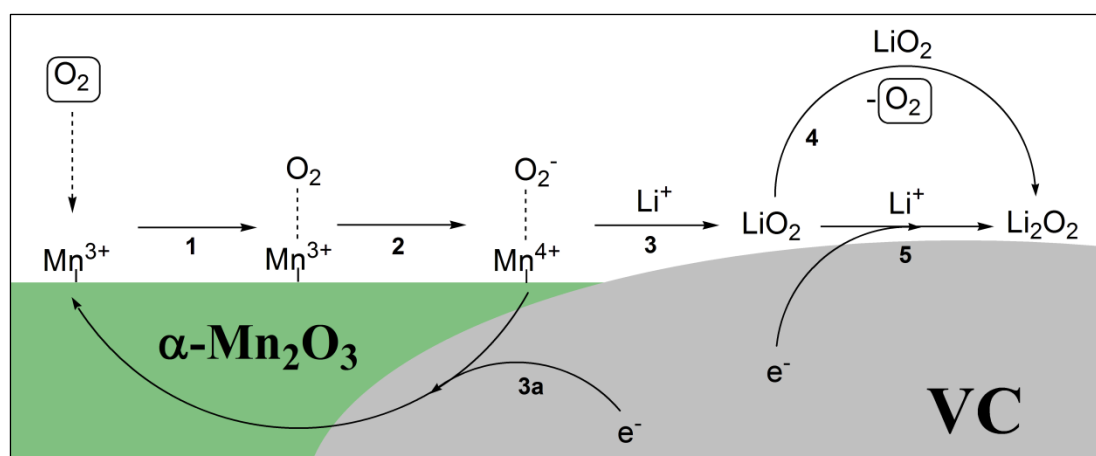


In order to prevent a complete oxidation of the α -Mn₂O₃ catalyst by rcts. (4.1) and (4.2) during the ORR, a re-reduction of the Mn⁴⁺ ions to Mn³⁺ has to take place. This is proposed to take place in a reaction step equivalent to that of rct. 1b in Scheme 4.2. Here, the adsorbed O₂⁻ reacts with Li⁺ to form LiO₂ and Mn⁴⁺ will be re-reduced to Mn³⁺ by an electron transfer. Therefore, the ORR processes should take place at active sites as close as possible to the comparably well-conducting carbon substrate in order to exclude a kinetic limitation by electronic conductivity. This was also suggested by Zhou *et al.* based on electrochemical and impedance measurements on carbon-supported Mn₂O₃ electrocatalysts for ORR in aqueous media[148]. For the α -Mn₂O₃ catalyst investigated here, the reactant transport to active catalyst sites close to the VC substrate might be facilitated by the mesopores of the relatively large α -Mn₂O₃ particles. These provide efficient diffusion paths for O₂ and Li⁺ ions inside the catalyst structure and thus minimize the distance between surface Mn³⁺ ions and carbon. Hence, the diffusion limitation of the process is probably due to the diffusion of the educts through the pores to the active sites. For the electron transport between the carbon substrate and α -Mn₂O₃, the low conductivity of the catalyst might be circumvented by electron transfers *via* internal Mn³⁺/Mn⁴⁺ redox reactions.

Scheme 4.3 depicts the ORR pathways suggested for the α -Mn₂O₃ electrode (see next page): After the formation of the surface species Mn⁴⁺ ⋯ O_{2,ads}⁻ (rct. 2 in Scheme 4.3), LiO₂ is generated by rct. 3 and a simultaneous reduction of Mn⁴⁺ by an electron transfer through the electrode structure (rct. 3a in Scheme 4.3). In a subsequent reaction, LiO₂ either

4.3.2. The ORR mechanisms at a scan rate of 100 mV/s

disproportionates chemically (rct. 4) or is reduced by a further one-electron transfer to Li_2O_2 (rct. 5 in Scheme 4.3). Based on the results of the Nicholson/Shain plots, which indicated the detection of chemical reactions also for $\alpha\text{-Mn}_2\text{O}_3/\text{C}$ (see Figure 4.22), and the comparably low ORR current densities observed in the CV measurements (see Figure 4.20), Li_2O_2 is suggested to be mainly formed by the chemical disproportionation of LiO_2 . During this reaction O_2 is formed (rct. 4 in Scheme 4.3), so that the educt for a further reduction is generated.



Scheme 4.3: ORR mechanisms suggested to take place on the surface of $\alpha\text{-Mn}_2\text{O}_3/\text{C}$.

Hence, the dissociative O_2 adsorption pathway *via* the critical O_{ads} , which is observed not only for $\text{Mn}_3\text{O}_4/\text{C}$ and $\text{Mn}_5\text{O}_8/\text{C}$ but also for pure VC, is at least partially circumvented by the presence of the $\alpha\text{-Mn}_2\text{O}_3$ catalyst. Because this is proposed to be due to the large catalyst particles as well as active O_2 adsorption and redox sites on the $\alpha\text{-Mn}_2\text{O}_3$ surface, the ORR will only partially proceed on the VC substrate. This is in good agreement to the discussion of the large Tafel slopes, where the small $\alpha\text{-Mn}_2\text{O}_3 - \text{VC}$ contact area was suggested to result in less participation of the substrate in the ORR processes.

A comparison of the ORR potentials and kinetic parameters obtained from CV measurements with $\omega = 0$ rpm compared to those with $\omega = 200$ rpm should theoretically show a kinetic limitation of the diffusion-controlled ORR processes by less reactant transport to the active surface electrocatalytic (see Table 4.12).

Table 4.12: Potentials and kinetic parameters for $\alpha\text{-Mn}_2\text{O}_3/\text{C}$ at $\nu = 100$ mV/s with $\omega = 0$ rpm and $\omega = 200$ rpm. Important values concerning the discussion of the ORR mechanism and activity are highlighted yellow and grey, respectively; for a further discussion, see text.

	0 rpm	200 rpm
E_{onset} vs. Li/Li ⁺ / V	2.72 ± 0.04	2.87 ± 0.06
Tafel slope / mV/dec	236 ± 11	223 ± 52
αn	0.25 ± 0.01	0.28 ± 0.06
k_{app}^0 / 10 ⁻⁴ cm/s	7.4 ± 2.7	18.4 ± 3.9

The αn value with $\omega = 0$ rpm given in Table 4.12 is comparable to that obtained with $\omega = 200$ rpm, i.e., the decrease of the energy barrier for the initial electron transfer by $\alpha\text{-Mn}_2\text{O}_3/\text{C}$ is comparable for both experimental conditions.

The onset potential E_{onset} obtained without electrode rotation is decreased by about 0.15 V compared to that observed with $\omega = 200$ rpm. Furthermore, a limited kinetic activity is indicated by the significantly lower apparent rate constant k_{app}^0 obtained with $\omega = 0$ rpm compared to that obtained with electrode rotation. Hence, the proposal that in the presence of the $\alpha\text{-Mn}_2\text{O}_3$ catalyst the ORR proceeds *via* a diffusion-controlled mechanism is validated by a limitation of the ORR processes caused by a restriction of the O₂ transport toward the electrode surface.

4.3.2. The ORR mechanisms at a scan rate of 100 mV/s

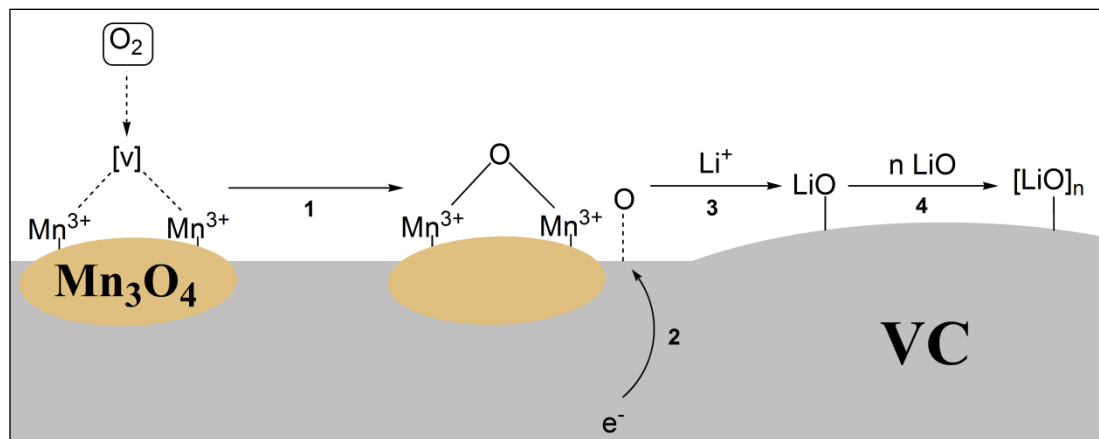
The assumption that the ORR mechanism taking place on the VC surface is changed in the presence of α - Mn_2O_3 due to active redox centers in the catalyst structure is supported by a recent report on Zr-doped ceria catalysts in a TEGDME-based electrolyte[149]. In that study surface Ce^{3+} ions were proposed to act as active centers for O_2 adsorption and O_2^- formation similar to the reactions shown in Scheme 4.3 for α - $\text{Mn}_2\text{O}_3/\text{C}$. The positive impact of different oxidation states in catalyst structures is further supported by X-ray absorption spectroscopy (XAS) and *in situ*-infrared (IR) spectroscopy studies. Here, the presence of different oxidation states of transition metals in Cr , Cr_2O_3 and LaCrO_3 as well as IrO_2 catalysts has been shown to positively influence their catalytic activities in ether-based and aqueous electrolytes[68,76].

4.3.2.3. The ORR processes in the presence of Mn_3O_4 or Mn_5O_8

O_2 adsorption and reduction sites provided by Mn^{z+} ions are also assumed to play a considerable role for the ORR mechanism observed in the presence of the Mn_3O_4 and Mn_5O_8 catalysts. For these compounds diffusionless ORR processes were indicated by $n^* = 2$ obtained from the Nicholson/Shain plots (see Figure 4.22). This means, that the ORR processes are limited by the electron transfers and/or include chemical reactions, which has also been suggested for pure VC (see rcts. 2a-2c in Scheme 4.2).

The Mn_3O_4 catalyst exhibits Mn^{3+} ions in its structure, which were already proposed to be the reason for the higher activity of the α - Mn_2O_3 catalyst. Furthermore, oxygen vacancies are suggested to be present in the Mn_3O_4 structure, which is based on the observation of decreased lattice constants as discussed in section 4.1.2.3. The conclusions drawn for the ORR pathways taking place on the electrode surface of $\text{Mn}_3\text{O}_4/\text{C}$ by considering the

structural features of Mn_3O_4 and the results from the electrochemical measurements are shown in Scheme 4.4.



Scheme 4.4: ORR mechanisms suggested to take place on the surface of $\text{Mn}_3\text{O}_4/\text{C}$. [v] in denotes an oxygen vacancy in the structure of the Mn_3O_4 nanoparticles.

The ORR mechanism for Mn_3O_4 depicted in Scheme 4.4.a is based on suggestions for TiO_2 catalysts and TiO_2 -supported Au catalysts for CO oxidation[87,150]. The oxygen vacancies [v] in the Mn_3O_4 structure increase the activity for a dissociative O_2 adsorption resulting in 2O_{ads} . This reaction proceeds by an uptake of an O atom into the structure of the Mn_3O_4 catalyst and the adsorption of another O atom at adjacent carbon sites (ret. 1 in Scheme 4.4.a). O_{ads} is subsequently reduced and reacts with Li^+ to LiO_{ads} (ret. steps 2 and 3), thus generating $[\text{LiO}]_{\text{n,ads}}$ compounds by further reduction *via* ret. 4 according to the reaction mechanism proposed by Dathar *et al.* for noble metals like Pd and Pt[19]. This ORR pathway proceeds *via* the generation of the undesired highly active O_{ads} intermediates.

Because structural and catalytic studies on the metastable Mn_5O_8 phase are rare, a specific ORR mechanism, which might take place in the presence of this compound, can hardly be suggested. An explanation, however, could be the presence of Mn^{4+} ions in the catalyst structure[151]. Here, the energy

4.3.2. The ORR mechanisms at a scan rate of 100 mV/s

input resulting from the ORR processes might coincide with $\text{Mn}^{4+}/\text{Mn}^{3+}$ redox reactions inside the catalyst structure and lead to an irreversible change of the metastable Mn_5O_8 phase.

However, a further indication for the ORR processes discussed for $\text{Mn}_3\text{O}_4/\text{C}$ and $\text{Mn}_5\text{O}_8/\text{C}$ are the comparably large current densities observed during the CV measurements (see Figure 4.20). Here, the product of O_{ads} reduction ($[\text{LiO}]_{\text{n,ads}}$, rct. 2b in Scheme 4.2) will only result in a stoichiometric equivalent of Li_2O_2 by another one-electron reduction (rct. 2c in Scheme 4.2), hence the increase of the detected current.

A comparison of the potentials and kinetic parameters obtained from CV measurements with $\omega = 0$ rpm and with $\omega = 200$ rpm for $\text{Mn}_3\text{O}_4/\text{C}$ and $\text{Mn}_5\text{O}_8/\text{C}$ should result in comparable activities for the diffusionless ORR processes with and without electrode rotation (see Table 4.13).

Table 4.13: Potentials and kinetic parameters for $\text{Mn}_3\text{O}_4/\text{C}$ and $\text{Mn}_5\text{O}_8/\text{C}$ at $\nu = 100$ mV/s with $\omega = 0$ rpm and $\omega = 200$ rpm. Important values concerning the discussion of the ORR activity and mechanism are highlighted yellow and grey; for a further discussion, see text.

	$\text{Mn}_3\text{O}_4/\text{C}$		$\text{Mn}_5\text{O}_8/\text{C}$	
	0 rpm	200 rpm	0 rpm	200 rpm
E_{onset} vs. Li/Li ⁺ / V	2.73 ± 0.04	2.71 ± 0.10	2.76 ± 0.02	2.78 ± 0.04
Tafel slope / mV/dec	246 ± 49	204 ± 16	202 ± 14	199 ± 19
αn	0.24 ± 0.05	0.29 ± 0.02	0.29 ± 0.02	0.30 ± 0.03
$k_{\text{app}}^0 / 10^{-4}$ cm/s	8.7 ± 1.8	9.0 ± 4.7	9.7 ± 1.5	9.5 ± 2.8

The αn values for both catalysts show no significant differences (highlighted yellow in Table 4.13), i.e., the initial electron transfers are comparable for both experimental conditions. However, the mean value of the Tafel slope obtained for $\text{Mn}_3\text{O}_4/\text{C}$ without electrode rotation indicates an increased

build-up of an oxide layer on the electrode surface compared to that indicated by the Tafel slope obtained with $\omega = 200$ rpm (highlighted grey in Table 4.13).

For both electrode materials the mean values of E_{onset} and k_{app}^0 for the diffusionless ORR processes obtained without electrode rotation differ by only 0.02 V to 0.03 V and 3% to 4%, respectively, to those obtained with $\omega = 200$ rpm (highlighted yellow in Table 4.13). The fact that the decreased mass transport does not result in decreased ORR kinetics – contrary to the results obtained for pure VC (see Table 4.11) – indicates catalytic activities of the Mn_3O_4 and Mn_5O_8 for the formation of $[\text{LiO}]_{\text{n,ads}}$. As the diffusionless processes obtained for $\text{Mn}_3\text{O}_4/\text{C}$ and $\text{Mn}_5\text{O}_8/\text{C}$ proceed *via* a CE (chemical/electrochemical) pathway, for which the kinetics are controlled by the initial chemical step, these Mn_xO_y compounds are proposed to be (slightly) active *chemical* catalysts.

4.3.3. Conclusion

The catalytic activities of the Mn_xO_y compounds were compared to those of the carbon reference materials glassy carbon (GC) and carbon powder (VC) by CV measurements recorded at $\nu = 100$ mV/s. One of the main findings is that the carbon reference materials are active for two different ORR mechanisms. The CV measurements confirmed the formation of LiO_2 and Li_2O_2 on the GC surface, which has previously been suggested in the literature. The porous VC (also used as support material for the catalysts), on the other hand, was found to enhance the ORR processes *via* a formation of the undesired adsorbed oxygen atoms (O_{ads}). Recent literature suggested these intermediate species to be one reason for the decomposition of ether-based electrolytes.

4.3.3. Conclusion

The Mn_5O_8 and especially the Mn_3O_4 catalyst show activity for the chemical step of this chemical-electrochemical (CE) ORR pathway resulting in the formation of $[\text{LiO}]_{\text{ads}}$ *via* highly reactive O_{ads} species. Catalytic activities for the dissociative O_2 adsorption pathway (comparable to that observed for VC, $\text{Mn}_3\text{O}_4/\text{C}$ and $\text{Mn}_5\text{O}_8/\text{C}$) was also reported for several noble metals with large oxygen adsorption enthalpies, such as Ir, Ru, Pt and Pd[19,61–65].

The $\alpha\text{-Mn}_2\text{O}_3$ compound, on the other hand, was shown to catalyze the one-electron reduction of molecularly adsorbed O_2 even in the presence of VC substrate. From the LiO_2 species formed during this reaction the desired discharge product Li_2O_2 is generated. Because the ORR observed for $\alpha\text{-Mn}_2\text{O}_3/\text{C}$ proceeds *via* a different reaction pathway, the apparent rate constant k_{app}^0 indicating the kinetic activity is hardly comparable to those for noble metal catalysts reported in the literature as well as those for the pure VC and $\text{Mn}_x\text{O}_y/\text{C}$ electrodes discussed in this work.

However, as the presence of $\alpha\text{-Mn}_2\text{O}_3$ results in the desired ORR pathway (and decreases the amount of O_{ads} intermediates), this compound is proposed to be the most promising catalyst investigated in this work.

4.4. The scan rate dependence of the observed ORR processes

In the previous section the assumption was made that the ORR mechanisms observed for the different electrode materials at a scan rate of 100 mV/s result from the respective material properties, such as the Mn^{z+} oxidation states and particle diameters. In order to confirm this suggestion, CV measurements recorded at scan rates between 1 mV/s and 1000 mV/s are discussed in this section with respect to the scan rate dependence of the detected ORR processes for the different electrode materials. This section contains results already published elsewhere[105,135].

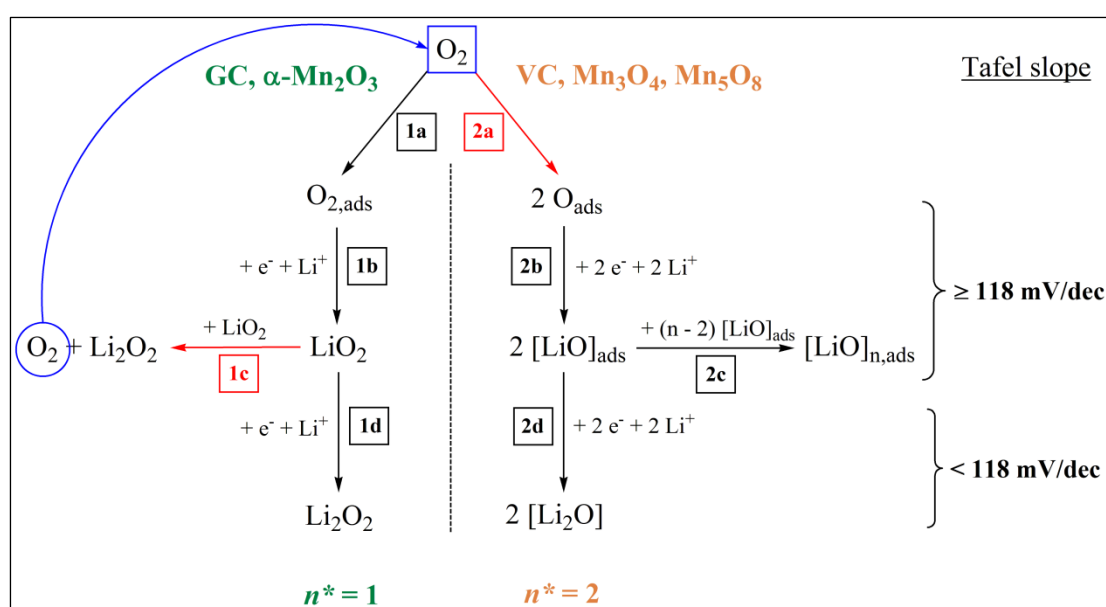
4.4.1. The scan rate dependence of the ORR mechanisms

Scheme 4.5 depicts the ORR pathways, which have been suggested in the previous section to take place in the presence of the different electrode materials (see next page). These ORR mechanisms were derived from the Tafel slopes (giving information about the reaction steps preceding and/or during the initial electron transfer) as well as the n^* values obtained from the Nicholson/Shain relationship (indicating the rate limitation of the overall ORR process). The interpretation of the Tafel slopes and n^* values is done as mentioned for the general case in section 2.4.1. A short summary with respect to the ORR processes given in Scheme 4.5 is discussed below.

A value of $n^* = 1$, which was obtained for α -Mn₂O₃/C and GC in section 4.3.2 (see Scheme 4.5) indicates a diffusion-controlled ORR mechanism (with fast electron transfers). Here, O₂ is molecularly adsorbed (rct. 1a) and reduced to LiO₂ (rct. 1b). Subsequently, Li₂O₂ is generated by either a chemical disproportionation of LiO₂ (rct. 1c) or a further electron transfer (rct. 1d). $n^* = 2$, which was observed for VC, Mn₃O₄/C and

4.4.1. The scan rate dependence of the ORR mechanisms

$\text{Mn}_5\text{O}_8/\text{C}$ at $\nu = 100$ mV/s, indicates a diffusionless process (with either a slow electron transfer or a preceding chemical step). In the case of the ORR mechanism depicted in Scheme 4.5 the slow electron transfer is suggested to derive from the kinetic control by the initial dissociation of O_2 , by which adsorbed O atoms are formed on the electrode surface (rct. 2a). A subsequent reduction leads to the generation of $[\text{LiO}]_{\text{ads}}$ (rct. 2b), which can either be further reduced to $[\text{Li}_2\text{O}]$ (rct. 2d) or form $[\text{LiO}]_{\text{n,ads}}$ species by $[\text{LiO}]$ layer growth (rct. 2c)[19,138].



Scheme 4.5: ORR mechanisms detected at various scan rates. Chemical reactions, which can be deduced from the CV measurements are given in red; the Tafel slopes at the right side indicate the electrochemical and chemical reactions taking place prior to and/or during the rate-determining steps (rds); for further information, see text.

For these mechanisms, Tafel slopes below 118 mV/dec are attributed to two consecutive electron transfers, of which the last electron transfer is the rate-determining step[49,53,54], i.e., for $n^* = 1$ the reduction of LiO_2 to Li_2O_2 (rct. 1d) and for $n^* = 2$ the reduction of $[\text{LiO}]$ to $[\text{Li}_2\text{O}]$ (rct. 2d). (Ideal)

Tafel slopes of 118 mV/dec indicate rate-determining one-electron transfers without preceding electron transfers, i.e., for $n^* = 1$ the reduction of $O_{2,ads}$ to LiO_2 (rct. 1a) and for $n^* = 2$ the reduction of O_{ads} to $[LiO]_{ads}$. Tafel slopes larger than 118 mV/dec, on the other hand, can be attributed to an electrode transfer through an oxide layer as well as electron transfers with either a preceding chemical dissociation or a subsequent chemical combination. For the ORR mechanisms depicted in Scheme 4.5, this means that for $n^* = 1$ the chemical disproportionation of LiO_2 to Li_2O_2 (rct. 1c) and/or an oxide layer formed from the ORR products could be detected. For $n^* = 2$ the reason for large Tafel slopes could be the chemical adsorption of O_2 (rct. 2a) and/or an oxide layer formation.

In order to ascribe the ORR pathways given in Scheme 4.5 to the different electrode materials, the results from the Nicholson/Shain plots revealing the rate limitation of the overall ORR processes are discussed prior to the Tafel slopes.

Figure 4.23 (see next page) shows the detection of a diffusion-controlled ORR mechanism ($n^* \approx 1$) for GC at all scan rates (light grey squares in Figure 4.23), which was also suggested in the literature at $\nu = 100$ mV/s[10]. The same ORR pathway resulting in LiO_2 and Li_2O_2 species (rcts. 1a-d in Scheme 4.5) is also observed for α - Mn_2O_3/C over the complete range of scan rates (blue circles in Figure 4.23). For these electrode materials, the diffusion control of the ORR mechanism does not change with the applied scan rate. This observation supports the assumption of the large impact of the electrode surface properties on the ORR mechanism, i.e., a smooth surface for GC and large particle sizes in combination with surface Mn^{3+} ions for α - Mn_2O_3/C .

More complex observations, however, are made in Figure 4.23 for the electrode materials, for which diffusionless ORR mechanisms ($n^* = 2$) were obtained at $\nu = 100$ mV/s. At low scan rates from 1 mV/s to 50 mV/s

4.4.1. The scan rate dependence of the ORR mechanisms

$n^* \approx 1.5$ is obtained for VC (dark grey circles in Figure 4.23). This is assumed to be due to the detection of parallel diffusionless and diffusion-controlled ORR mechanisms. In this range the scan rates are slow enough to allow a simultaneous detection of the kinetically favored $[\text{LiO}]_{\text{n,ads}}$ formation as well as the generation of LiO_2 and Li_2O_2 , which was not observed for VC at $\nu = 100$ mV/s for VC. At $\nu \geq 100$ mV/s, however, only diffusionless ORR processes leading to the generation of $[\text{LiO}]_{\text{n,ads}}$ species are observed.

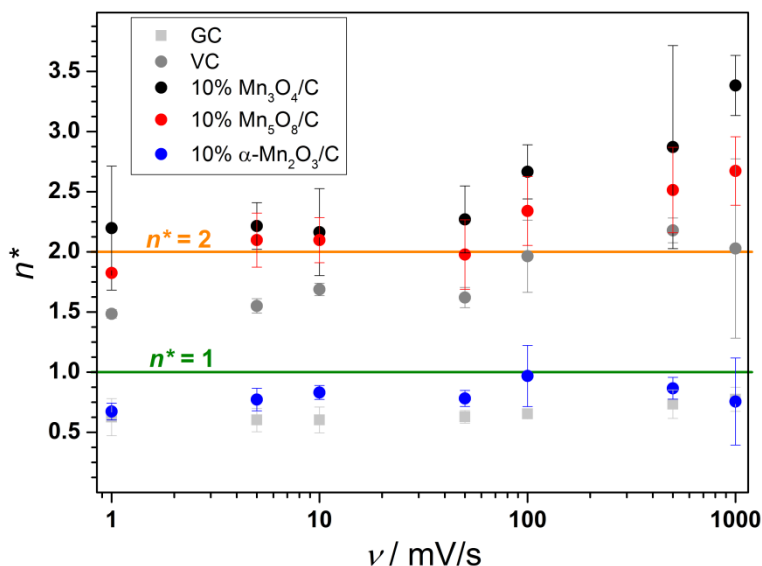


Figure 4.23: Variation of the n^* values with the applied scan rate. GC (light grey), VC (dark grey), $\text{Mn}_3\text{O}_4/\text{C}$ (black), $\text{Mn}_5\text{O}_8/\text{C}$ (red) and $\alpha\text{-Mn}_2\text{O}_3/\text{C}$ (blue); the green and orange lines denote values of $n^* = 1$ and $n^* = 2$, respectively.

In Figure 4.23, the catalytic activities of Mn_5O_8 and especially Mn_3O_4 for the diffusionless ORR processes become apparent at $\nu \leq 50$ mV/s. For pure VC mixed ORR processes were detected at these scan rates, whereas purely diffusionless ORR mechanisms ($n^* = 2$) are observed for $\text{Mn}_3\text{O}_4/\text{C}$ (black circles) and $\text{Mn}_5\text{O}_8/\text{C}$ (red circles). For both catalysts n^* increases to values > 2 with increasing scan rates. An explanation for the observation of such high n^* values can be found by considering the Nicholson/Shain relationship (eq. (2.12)). All parameters in this equation are either constant

or measured – with the exception of the O_2 concentration, which was replaced by the solubility of O_2 in DMSO, i.e., the maximum O_2 concentration. For highly active surfaces this might result in an estimation of too large n^* values, as these will increase with decreasing O_2 concentration c_{O_2} in front of the electrode surface by:

$$n^* \propto \frac{1}{c_{O_2}} \quad (4.3)$$

Therefore, the n^* values > 2 observed in Figure 4.23 are suggested here to be due to a low O_2 concentration close to the electrode surface resulting from the catalytic activities of the Mn_xO_y species. The fact that an increase of n^* to values > 1 is not observed for the active α - Mn_2O_3 catalyst might be explained by the generation of O_2 during the chemical disproportionation of LiO_2 to Li_2O_2 (ret. 1c in Scheme 4.5). This would result in a more stable O_2 concentration in front of the active α - Mn_2O_3/C surface in comparison to the O_2 concentrations in the presence of Mn_3O_4 and Mn_5O_8 .

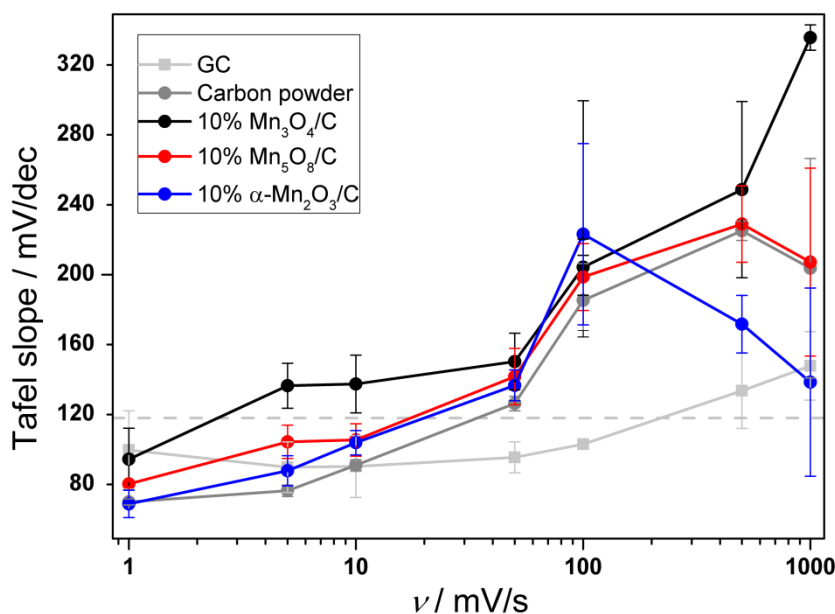


Figure 4.24: Variation of the Tafel slopes with the applied scan rate. GC (light grey), VC (dark grey), Mn_3O_4/C (black), Mn_5O_8/C (red) and α - Mn_2O_3/C (blue); the dashed grey line indicates the theoretical Tafel slope of 118 mV/dec for a rate-determining one-electron transfer.

4.4.1. The scan rate dependence of the ORR mechanisms

For the investigation of the initial electron transfers corresponding to the respective ORR mechanisms the Tafel slopes obtained at the different scan rates are depicted in Figure 4.24 (see previous page). The following discussion of the suggested ORR mechanisms for each electrode material at the different scan rates is based on the observed n^* values in combination with the respective Tafel slopes (see Figure 4.24).

4.4.1.1. The ORR processes on GC and $\alpha\text{-Mn}_2\text{O}_3/\text{C}$

An overview of the diffusion-controlled ORR processes and the final ORR products generated on the surfaces of GC and $\alpha\text{-Mn}_2\text{O}_3/\text{C}$, which are concluded from the Tafel slopes (see Figure 4.24) and $n^* \approx 1$, obtained from the Nicholson/Shain relationship (see Figure 4.23), at the different scan rates is given in Table 4.14 and discussed below.

Table 4.14: Overview of the final products proposed to be generated during the diffusion-controlled ORR processes observed for GC and $\alpha\text{-Mn}_2\text{O}_3/\text{C}$. The formation of the desired product Li_2O_2 (highlighted yellow) is proposed for both electrode materials at all scan rates.

v / mV/s	<i>GC</i>		<i>$\alpha\text{-Mn}_2\text{O}_3/\text{C}$</i>	
	initial e^- transfer	final products	initial e^- transfer	final products
1 – 10	$1 e^- (+ 2 e^-)$	Li_2O_2	$1 e^- (+ 2 e^-)$	Li_2O_2
50 – 100			$1 e^-$ through oxide layer	
500 – 1000	$1 e^-$ through oxide layer		$1 e^-$ through oxide layer (decreasing)	Li_2O_2 (mostly by chemical rect. from LiO_2)

GC. The Tafel slope obtained at $\nu = 100$ mV/s is about 104 mV/dec (see Figure 4.24), whereas the theoretical value for a single one-electron transfer is 118 mV/dec at this scan rate[10]. This observation was already discussed in section 4.2.3 to be due to the influence of the relatively low electrode rotation of $\omega = 200$ rpm, i.e., limited reactant transport. The Tafel slope of 104 mV/dec observed for GC is therefore proposed to be due to the simultaneous detection of one-electron transfers and a small amount of consecutive two-electron transfers. Tafel slopes < 118 mV/dec indicating these parallel electron transfer processes are observed at scan rates ≤ 100 mV/s (see Figure 4.24), which – in combination with the detection of diffusion-controlled ORR processes ($n^* \approx 1$, see Figure 4.23) – indicates the formation of LiO_2 and Li_2O_2 (rects. 1a-d in Scheme 4.5). At $\nu \geq 500$ mV/s Tafel slopes > 118 mV/dec point to electron transfers through oxide layers on the electrode surface consisting of LiO_2 and Li_2O_2 species.

$\alpha\text{-Mn}_2\text{O}_3$. Mixed two-electron and one-electron transfers (Tafel slopes < 118 mV/dec) are observed at scan rates from 1 mV/s to 10 mV/s (see Figure 4.24). As $n^* \approx 1$ was obtained at all scan rates (see Figure 4.23), the detected electron transfers are attributed to the reduction of O_2 to LiO_2 and Li_2O_2 *via* rects. 1a-b and 1d in Scheme 4.5. At $\nu \geq 50$ mV/s Tafel slopes > 118 mV/dec are obtained (see Figure 4.24), which is proposed to be due to electron transfers through a $\text{LiO}_2/\text{Li}_2\text{O}_2$ oxide layer on the electrode surface. At $\nu > 100$ mV/s the Tafel slope values decrease (see Figure 4.24), which is attributed to an increasing amount of Li_2O_2 generated by a chemical disproportionation of LiO_2 (rect. 1c in Scheme 4.5). As discussed previously, the evolution of O_2 as a product of this reaction leads to a decrease of the oxide layer on the catalyst/substrate surface, which results in lower Tafel slopes.

4.4.1. The scan rate dependence of the ORR mechanisms

4.4.1.2. The ORR processes on VC and Mn_5O_8/C

An overview of the ORR processes and the final ORR products for VC and Mn_5O_8/C , which are concluded from the Tafel slopes (see Figure 4.24) and the n^* values obtained from the Nicholson/Shain relationship (see Figure 4.23) at the different scan rates is given in Table 4.15 and discussed in the following.

Table 4.15: Overview of the final products proposed to be generated during the ORR processes observed for VC and Mn_5O_8/C . The desired product Li_2O_2 is highlighted yellow; the undesired product $[Li_2O]$ is highlighted grey.

ν / mV/s	VC		Mn_5O_8/C	
	initial e^- transfer	final products	initial e^- transfer	final products
1 – 10	1 e^- (+ 2 e^-)	Li_2O_2 / [LiO] _{n,ads} / [Li ₂ O]	1 e^- (+ 2 e^-)	[LiO] _{n,ads} / [Li ₂ O]
50 100 – 1000	1 e^- through oxide layer	Li_2O_2 / [LiO] _{n,ads} [LiO] _{n,ads}	1 e^- through oxide layer	[LiO] _{n,ads}

VC. Mixed diffusion-controlled and diffusionless processes are indicated by $n^* \approx 1.5$ at low scan rates of $\nu \leq 50$ mV/s (see Figure 4.23). The Tafel slopes < 118 mV/dec obtained at $\nu \leq 10$ mV/s (see Figure 4.24) additionally show the detection of parallel one- and two-electron transfers with a decreasing amount of two-electron transfer being observed with increasing scan rate. A specific attribution of the one- and two-electron transfers to one of the ORR processes (rects. 1a-d or 2a-d in Scheme 4.5) can therefore not be made with certainty. Hence, at these low scan rates, the possible ORR

products generated on the electrode surface of pure VC are LiO_2 and Li_2O_2 (highlighted yellow in Table 4.15) as well as the undesired $[\text{LiO}]_{\text{n,ads}}$ and probably even the $[\text{Li}_2\text{O}]$ species (highlighted grey in Table 4.15). Tafel slopes > 118 mV/dec indicate one-electron transfers through an oxide layer are observed at $\nu \geq 50$ mV/s (see Figure 4.24). Furthermore, an increase of the scan rate beyond $\nu = 100$ mV/s does not result in a change of the obtained Tafel slope values contrary to the observations made for $\alpha\text{-Mn}_2\text{O}_3/\text{C}$. As at $\nu = 50$ mV/s a value of $n^* \approx 1.5$ was obtained for VC (i.e., parallel diffusionless and diffusion-controlled ORR processes, see Figure 4.23), the oxide layer might consist of Li_2O_2 and $[\text{LiO}]_{\text{n,ads}}$ species (produced during rcts. 1a-d and 2a-c in Scheme 4.5). At $\nu \geq 100$ mV/s, however, values of $n^* = 2$ indicate purely diffusionless ORR processes (see Figure 4.23), so that the oxide layer on VC will only consist of $[\text{LiO}]_{\text{n,ads}}$ species generated by rcts. 2a-c (see Scheme 4.5).

Mn_5O_8 . Comparable to the results obtained for pure VC, Tafel slopes < 118 mV/dec indicate the detection of parallel one- and two-electron transfer processes at low scan rates of $\nu \leq 10$ mV/s (see Figure 4.24). The contribution of the initial two-electron transfers decreases with increasing scan rate. Because $\text{Mn}_5\text{O}_8/\text{C}$ is active for the diffusionless ORR processes ($n^* = 2$) at all scan rates (see Figure 4.23), the final products are suggested to be $[\text{LiO}]_{\text{n,ads}}$ (by an initial one-electron transfer, rcts. 2a-c in Scheme 4.5) and $[\text{Li}_2\text{O}]$ (by an initial two-electron transfer, rcts. 2a-b and 2d in Scheme 4.5). At $\nu \geq 50$ mV/s Tafel slopes > 118 mV/dec indicate one-electron transfers through an oxide layer (see Figure 4.24), which most probably consists of $[\text{LiO}]_{\text{n,ads}}$ species generated by rcts. 2a-c depicted in Scheme 4.5.

4.4.1. The scan rate dependence of the ORR mechanisms

4.4.1.3. The ORR processes on Mn_3O_4/C

An overview of the diffusionless ORR processes and the final products generated on the electrode surface of Mn_3O_4/C , which are concluded from the Tafel slopes (see Figure 4.24) and $n^* \geq 2$ obtained from the Nicholson/Shain relationship (see Figure 4.23) at the different scan rates is given in Table 4.16 and discussed in the following.

Table 4.16: Overview of the final products proposed to be generated during the diffusionless ORR processes observed for Mn_3O_4/C . The undesired product $[Li_2O]$ is highlighted grey.

ν / mV/s	initial e ⁻ transfer	final products
1	1 e ⁻ (+ 2 e ⁻)	$[LiO]_{n,ads}$ / $[Li_2O]$
5 –	1 e ⁻ through oxide	$[LiO]_{n,ads}$
50	layer	
100 –	1 e ⁻ through oxide	
1000	layer (growing)	

A Tafel slope < 118 mV/dec, i.e., the detection of parallel one- and two-electron transfer processes, is only observed at $\nu = 1$ mV/s (see Figure 4.24). At this scan rate $[LiO]_{n,ads}$ and $[Li_2O]$ (rcts. 2a-d in Scheme 4.5) are generated by the diffusionless ORR processes ($n^* = 2$, see Figure 4.23). One-electron transfers through an oxide layer of $[LiO]_{n,ads}$ species are indicated by Tafel slopes > 118 mV/dec at $\nu > 5$ mV/s (see Figure 4.24). Whereas the Tafel slopes for VC and Mn_5O_8/C (for which diffusionless ORR processes are also observed) stay about constant for $\nu > 100$ mV/s, those obtained for Mn_3O_4/C increase up to a value of ~ 335 mV/dec at $\nu = 1000$ mV/s (see Figure 4.24). This observation indicates a considerable build-up of oxide species on the electrode surface, which is in good agreement with the reaction mechanism

proposed to take place in the presence of Mn_3O_4 in section 4.3.2.3 (see Scheme 4.4). Here, the dissociative adsorption of O_2 generates two O atoms: one is built into the structure of the catalyst and another O atom is adsorbed on adjacent carbon atoms of the VC substrate (rct. 1 in Scheme 4.4). Due to the catalytic activity of Mn_3O_4 for the chemical O_2 dissociation step, it is suggested here, that the subsequent reduction of the O atoms adsorbed on the VC substrate might not be fast enough. Hence, the kinetics of the ORR process is limited by the electron transfer. These reactions will ultimately lead to a high intermediate coverage of O_{ads} and $[\text{LiO}]_{\text{ads}}$ species on the VC substrate surrounding the Mn_3O_4 catalyst particles.

This assumption is supported by the results depicted in Figure 4.25 (see next page), where the variation of the Tafel slopes and the change of onset potentials with the applied scan rate observed for $\text{Mn}_3\text{O}_4/\text{C}$ are compared to those obtained for all other VC-based electrodes. Here, an independent development of the Tafel slope values and E_{onset} with increasing scan rate indicates a high coverage of the active electrode area with adsorbed intermediates *generated during the rate-determining step*[49]. A too high coverage of intermediate species will have a negative impact on subsequent reactions (e.g., electron transfers) by blocking the active electrode surface.

For pure VC the onset potential ($E_{\text{onset},\nu} - E_{\text{onset},1 \text{ mV/s}}$) depicted Figure 4.25.b has a relative maximum of about 0.5 V at $\nu = 100 \text{ mV/s}$. At this scan rate $\text{Mn}_5\text{O}_8/\text{C}$ and $\alpha\text{-Mn}_2\text{O}_3/\text{C}$ exhibit absolute maxima of about 0.9 V and 0.15 V, respectively (see Figure 4.25.b), i.e., the *overpotentials* are smallest at $\nu = 100 \text{ mV/s}$ for these VC-based electrodes (see dotted green circle in Figure 4.25.b). This is in good agreement with the observation of a considerable oxide layer formation indicated by the strong increase in Tafel slopes observed for VC, $\text{Mn}_5\text{O}_8/\text{C}$ and $\alpha\text{-Mn}_2\text{O}_3/\text{C}$ at $\nu = 100 \text{ mV/s}$ (see

4.4.1. The scan rate dependence of the ORR mechanisms

Figure 4.25.a) and indicates the most favorable ORR kinetics for these electrode materials at $\nu = 100$ mV/s.

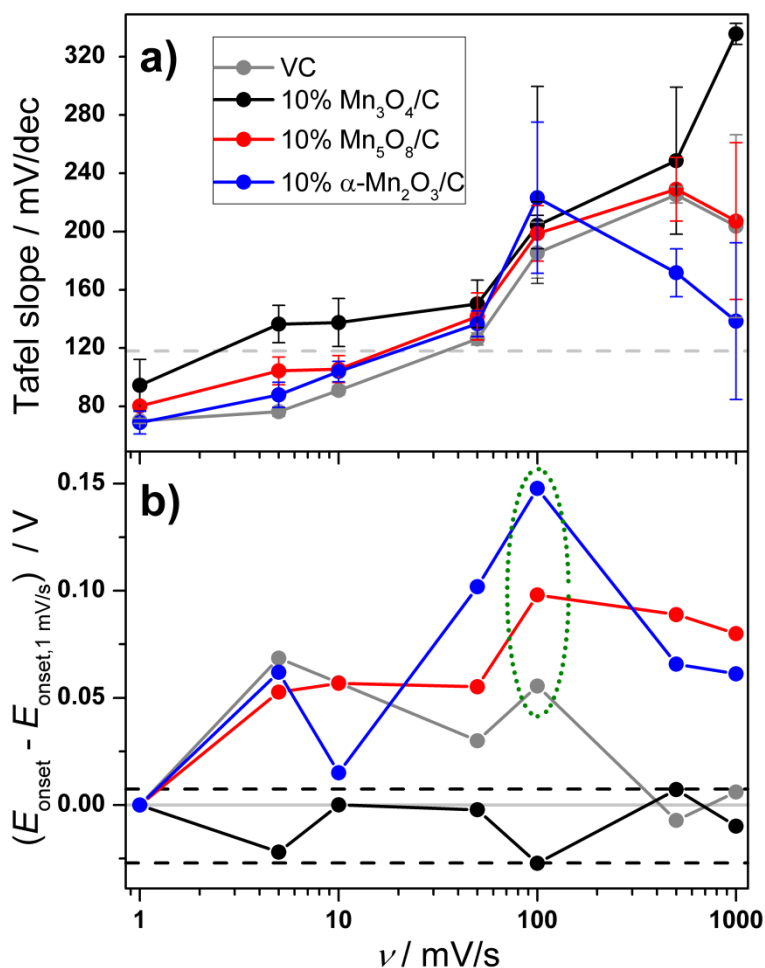


Figure 4.25: Variation of the (a) Tafel slopes and (b) onset potentials with the applied scan rate. VC (grey), $\text{Mn}_3\text{O}_4/\text{C}$ (black), $\text{Mn}_5\text{O}_8/\text{C}$ (red) and $\alpha\text{-Mn}_2\text{O}_3/\text{C}$ (blue); the dashed grey line in (a) indicates the theoretical Tafel slope of 118 mV/dec for a rate-determining one-electron transfer; the change of E_{onset} in (b) is given with respect to E_{onset} at $\nu = 1$ mV/s; the dashed black lines in (b) show the maximum and minimum values of the relative onset potentials of $\text{Mn}_3\text{O}_4/\text{C}$; the dotted green circle in (b) highlights the maxima of the relative onset potentials at $\nu = 100$ mV/s.

An independent development of E_{onset} and the Tafel slope is only observed for $\text{Mn}_3\text{O}_4/\text{C}$: whereas E_{onset} is located at comparable potentials at all scan

rates (see dashed black lines in Figure 4.25.b), the Tafel slope values increase considerably with increasing scan rate (see Figure 4.25.a). As mentioned previously, this indicates a high coverage of the electrode surface with adsorbed intermediate species generated during the rate-determining step. Furthermore, (i) the almost constant E_{onset} (within a potential range of 0.04 V) over the whole range of scan rates indicates scan rate-independent ORR processes, i.e., probably electron transfers following chemical reactions and (ii) the steady increase of the Tafel slopes points to a build-up of an oxide layer. Hence, in the presence of Mn_3O_4 , intermediate species are generated subsequent to or by a chemical reaction and form an oxide layer on the electrode surface. This confirms the assumption of O_{ads} and/or $[\text{LiO}]_{\text{ads}}$ species formed by dissociative O_2 adsorption and subsequent reduction processes (rcts. 2a-b in Scheme 4.5) and supports the findings from section 4.3.2.3, that Mn_3O_4 is an active catalyst for the initial chemical reaction of the CE mechanism.

The peak potentials E_{peak} (see Figure 4.26 on the next page) give further indications to support these argumentations. Figure 4.26 depicts the peak potentials E_{peak} obtained for all electrode materials at scan rates in the range of 1 mV/s to 1000 mV/s. For VC, $\text{Mn}_5\text{O}_8/\text{C}$ and $\alpha\text{-Mn}_2\text{O}_3/\text{C}$ the maximum values of E_{peak} , i.e., the lowest overpotentials, at $\nu = 100$ mV/s coincide with the strongest Tafel slope increase (proposed to be due to oxide layer formation, see Figure 4.25.a). Because E_{peak} indicates the end of the kinetically controlled reactions, the oxide layers on the electrode surfaces do not seem to limit the progress of the ORR processes.

4.4.1. The scan rate dependence of the ORR mechanisms

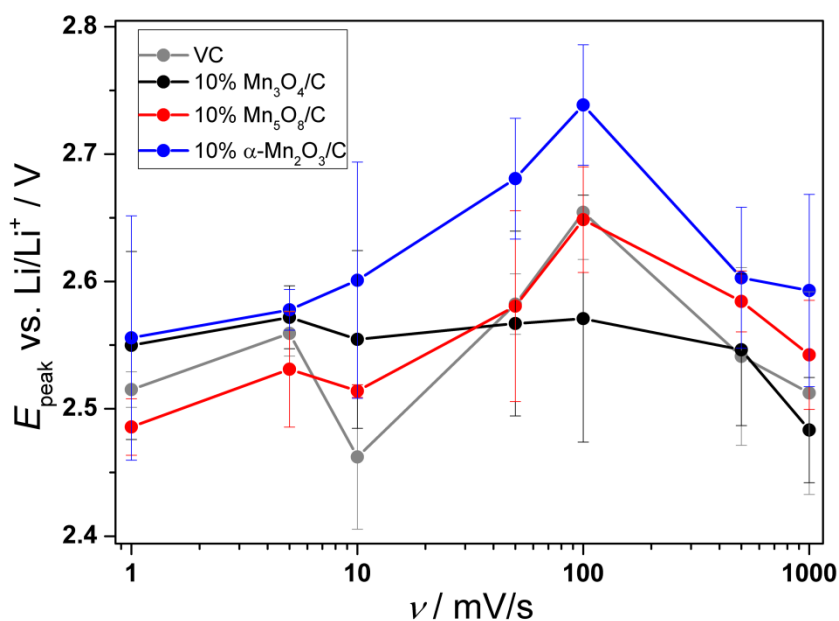


Figure 4.26: Variation of the peak potentials with the scan rate. VC (grey), $\text{Mn}_3\text{O}_4/\text{C}$ (black), $\text{Mn}_5\text{O}_8/\text{C}$ (red) and $\alpha\text{-Mn}_2\text{O}_3/\text{C}$ (blue).

For $\text{Mn}_3\text{O}_4/\text{C}$ a different observation is made: despite increasing Tafel slopes (see Figure 4.25.a), i.e., an increasing chemical activity resulting in oxide layer formation, E_{peak} is comparable at all applied scan rates (see Figure 4.26). Here, the kinetic activity for a further reduction of the adsorbed intermediate species is *not* increasing with increasing oxide layer formation. This supports the assumption that the oxide layer on the $\text{Mn}_3\text{O}_4/\text{C}$ surface consists of intermediate species, which limit the electron transfer (most probably by blocking the active electrode surface).

Therefore it seems, that the Mn_3O_4 catalyst might be too active for efficient ORR processes to take place: due to the catalysis of the dissociative O_2 adsorption, the subsequent electron transfer will not be fast enough at large scan rates. This results in an increasing blocking of carbon sites adjacent to the Mn_3O_4 particles and thus a kinetic limitation of the ORR processes by the electron transfer.

4.4.2. The scan rate dependence of the ORR activities

For an investigation of the impact of the different ORR mechanisms on the ORR activities the apparent rate constants k_{app}^0 obtained for the respective electrode materials at the different scan rates are depicted in Figure 4.27.

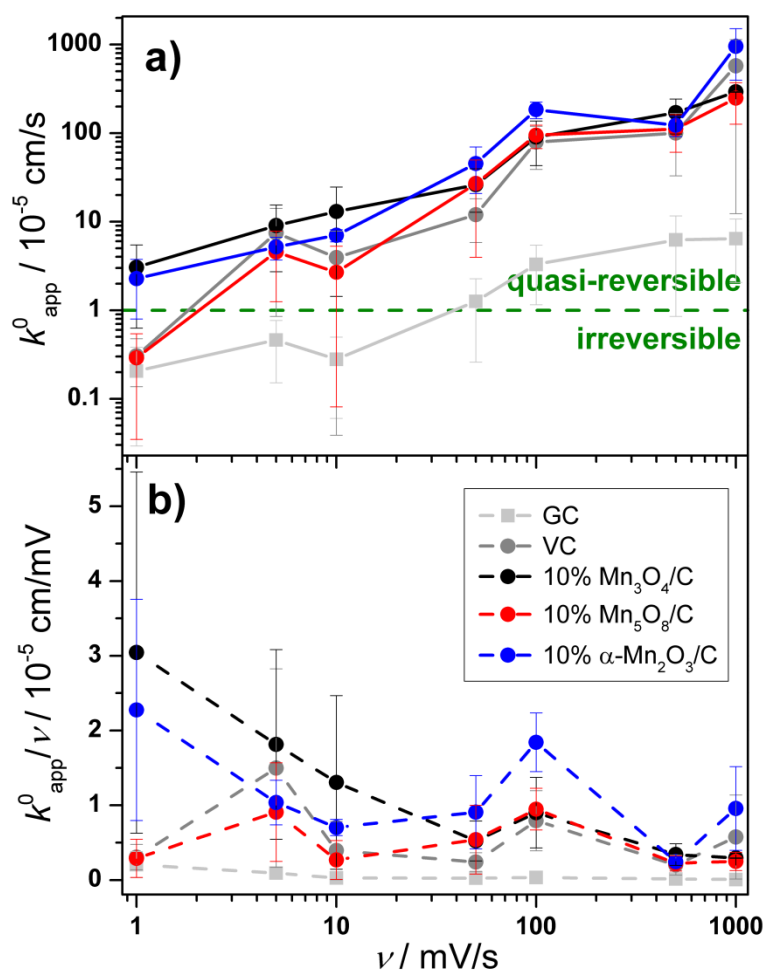


Figure 4.27: Variation of the (a) apparent rate constants k_{app}^0 and (b) scan rate-normalized k_{app}^0 with the scan rate. GC (light grey), VC (dark grey), $\text{Mn}_3\text{O}_4/\text{C}$ (black), $\text{Mn}_5\text{O}_8/\text{C}$ (red) and $\alpha\text{-Mn}_2\text{O}_3/\text{C}$ (blue).

Figure 4.27.a shows that for VC as well as $\text{Mn}_5\text{O}_8/\text{C}$ apparent rate constants $k_{\text{app}}^0 < 1 \cdot 10^{-5} \text{ cm/s}$ are obtained at $\nu = 1 \text{ mV/s}$. This indicates irreversible ORR processes and therefore probably the formation of the

4.4.2. The scan rate dependence of the ORR activities

undesired discharge product Li_2O . This was already proposed to be generated at low scan rates on $\text{Mn}_5\text{O}_8/\text{C}$ and pure VC based on the observations of $n^* = 2$ (the inclusion of chemical steps in the ORR) in combination with Tafel slopes < 118 mV/dec (two consecutive one-electron transfers, see Table 4.15). For GC irreversible processes are observed at $\nu \leq 10$ mV/s. This, however, might be due to its considerably smaller active area compared to those of VC-based electrodes.

Scan rate-normalized k_{app}^0 values are given in Figure 4.27.b for all electrode materials for a better insight into the kinetic ORR activities of the different electrode materials at the respective scan rates. The normalization was carried out to eliminate the linear dependence of k_{app}^0 on the scan rate observed in Figure 4.27.a for a better comparison of the ORR activities obtained at the respective scan rates.

The normalized rate constants k_{app}^0/ν obtained for GC show the ideal values of uncatalyzed reactions. Here, the kinetic activities are comparable for all applied scan rates.

Consistent with the results obtained from the ORR mechanisms in section 4.4.1 all VC-based electrodes show relative maxima of the scan-rate normalized k_{app}^0 values at $\nu = 100$ mV/s. $\text{Mn}_3\text{O}_4/\text{C}$ seems to be the most active catalyst at $\nu \leq 10$ mV/s, at which the reduction processes subsequent to the formation of the O_{ads} intermediates are fast enough, i.e., enough time is provided by the long scanning time, to generate $[\text{LiO}]_{\text{n,ads}}$ species. At larger scan rates, however, the chemically catalyzed formation of the O_{ads} species is faster than the subsequent reduction processes, which results in an accumulation of intermediates on the electrode surface and thus a blocking of the active sites, as discussed in the previous section.

Regarding VC and $\text{Mn}_5\text{O}_8/\text{C}$, for which ORR mechanisms comparable to that discussed for $\text{Mn}_3\text{O}_4/\text{C}$ were observed, the Mn_5O_8 catalyst does not seem

to have any influence on the overall kinetic activity. Considering the ORR mechanism discussed in section 4.4.1, its presence even seems to have a negative effect, as it is active for the formation of $[\text{LiO}]_{\text{n,ads}}$ and $[\text{Li}_2\text{O}]$ species at low scan rates, which are only partially generated on pure VC (see Table 4.15).

The largest kinetic activity is observed for the $\alpha\text{-Mn}_2\text{O}_3$ catalyst at $\nu = 50$ mV/s and $\nu = 100$ mV/s (at which for all electrode materials the largest ORR potentials, i.e., the highest activity, were found in the previous section). Here, the catalysis of the diffusion-controlled ORR mechanism by $\alpha\text{-Mn}_2\text{O}_3$ seems to be of considerable advantage by comparison to the normalized rate constants k_{app}^0/ν obtained for the other electrode materials.

At scan rates > 100 mV/s no significantly different k_{app}^0/ν values are obtained for any of the VC-based electrodes, which might be due to either (i) too small kinetic activities of the Mn_xO_y catalysts or (ii) a non-significant kinetic impact of catalysts at large scan rates in general.

4.4.3. Conclusion

The investigation of the ORR mechanisms detected at scan rates between $\nu = 1$ mV/s and $\nu = 1000$ mV/s for the different electrode materials generally confirmed the suggestion, that the ORR mechanisms discussed for a scan rate of 100 mV/s depend on the respective material properties.

The diffusion-controlled ORR pathways resulting in the formation of LiO_2 and Li_2O_2 were observed for GC at all scan rates.

Interestingly, the ORR processes on the VC surface were found to be diffusionless at large scan rates (i.e., result in $[\text{LiO}]_{\text{n,ads}}$ species), whereas at low scan rates the ORR proceeds *via* mixed diffusionless and diffusion-

4.4.3. Conclusion

controlled processes (resulting in the generation of $[\text{LiO}]_{\text{n,ads}}$ and the desired Li_2O_2 species). Here, at least to a certain degree, the measurement conditions, i.e., the applied scan rate, – and not only the material properties – influence the species generated during the ORR processes.

The presence of the $\alpha\text{-Mn}_2\text{O}_3$ catalyst results in a suppression of the diffusionless ORR pathways in favor of diffusion-controlled ORR processes and thus the generation of LiO_2 and Li_2O_2 species at all scan rates. The catalysis of this mechanism leads to the highest kinetic ORR activities of $\alpha\text{-Mn}_2\text{O}_3/\text{C}$ compared to the other electrode materials at scan rates of 50 mV/s and 100 mV/s.

In the presence of the Mn_5O_8 and Mn_3O_4 compounds, on the other hand, the diffusion-controlled ORR pathways are suppressed, so that the purely diffusionless ORR processes lead to the undesired generation of adsorbed oxygen atoms (O_{ads}) and $[\text{LiO}]_{\text{n,ads}}$ formation at all scan rates. The initial dissociative O_2 adsorption leading to the formation of O_{ads} intermediates is chemically catalyzed by Mn_3O_4 , which results in the largest ORR activity at low scan rates between 1 mV/s and 10 mV/s. The catalytic activity of Mn_3O_4 , however, has a negative effect at increased scan rates, as the reduction processes subsequent to the chemical generation of the O_{ads} species are not fast enough. This leads to a blocking of active reaction sites by O_{ads} and $[\text{LiO}]_{\text{ads}}$ accumulation on the electrode surface and hence decreased ORR kinetics.

5. Conclusion & Outlook

In this study, three nanostructured Mn_xO_y compounds were synthesized and investigated for their electrocatalytic ORR activities in aprotic media.

Mn_3O_4 , Mn_5O_8 and $\alpha\text{-Mn}_2\text{O}_3$ particles with surface areas of $302\text{ m}^2/\text{g}$, $30\text{ m}^2/\text{g}$ and $20\text{ m}^2/\text{g}$, respectively, were obtained by calcination of nanocrystalline Mn(II) glycolate. The precursor was synthesized by a polyol process yielding nanoparticles with diameters of about 17 nm. The small precursor particle sizes are suggested to be the reason for the nanostructured character of the Mn_xO_y compounds. As the catalytic activity can be enhanced by larger active areas resulting from small particle diameters and mesoporosity, Mn_3O_4 nanoparticles and $\alpha\text{-Mn}_2\text{O}_3$ were investigated as electrocatalysts. Here, the structural and morphological characterization revealed the presence of oxygen vacancies in Mn_3O_4 and the mesoporous character of $\alpha\text{-Mn}_2\text{O}_3$. Additionally, Mn_5O_8 was investigated for the first time as an ORR electrocatalyst in aprotic media.

For the electrochemical measurements LiTFSI/DMSO was used as electrolyte, as it exhibits the best ORR/OER reversibility and ORR kinetics in comparison to other electrolytes.

The catalytic activities of the Mn_xO_y compounds were obtained by comparison to two carbon reference materials glassy carbon (GC) and carbon powder (VC). These carbon materials show different ORR mechanisms. The CV measurements presented in this study support the assumption of LiO_2 and Li_2O_2 formation on the smooth GC surface made in previous reports. The porous VC (which was also used as support material for the catalysts) shows an undesired generation of adsorbed oxygen atoms (O_{ads}), which have previously been suggested to be one reason for the decomposition of ether-based electrolytes. An only small catalytic activity for the latter ORR

5. Conclusion & Outlook

pathway is observed for Mn_5O_8 . The Mn_3O_4 nanoparticles, however, show considerable catalytic activity for the formation of O_{ads} species by chemical O_2 adsorption. This effect is proposed to be due to the presence of oxygen vacancies (derived from structural characterization for this catalyst). Subsequent to the dissociation of O_2 , one of the O atoms might be built into the Mn_3O_4 structure, whereas the other O atom is adsorbed on adjacent carbon sites. The $\alpha\text{-Mn}_2\text{O}_3$ catalyst, on the other hand, is active for the formation of $\text{LiO}_2/\text{Li}_2\text{O}_2$, which has also been observed for GC. As the pure VC substrate generates O_{ads} species, the ORR mechanism in the presence of $\alpha\text{-Mn}_2\text{O}_3$ is proposed to take place to a considerable part on the surface of the catalyst particles. The surface Mn^{3+} ions provide sites, where O_2 can be associatively adsorbed and subsequently be reduced to adsorbed O_2^- species, from which the desired discharge product Li_2O_2 is generated. The $\alpha\text{-Mn}_2\text{O}_3$ compound presented in this work is therefore proposed to be an ORR catalyst, which is also suitable for the use in combination with ether-based electrolytes.

Regarding the application in Li/air systems and the effect on galvanostatic cyclability of Li/air batteries, the formation of Li_2O at low ORR potentials, i.e., large ORR overpotentials, has to be considered. The discharge currents of $100 \mu\text{A}/\text{cm}^2$ presently used in Li/air research result in large discharge capacities, but are not sufficient for an industrial application. Larger current densities, however, result in very low capacities and increased discharge overpotentials, at which – subsequent to the generation of $\text{LiO}_2/\text{Li}_2\text{O}_2$ – the electrochemically irreversible formation of Li_2O will take place.

Here, a catalyst is needed, which (i) reduces the overpotential during discharge by (ii) being active only for the formation of LiO_2 . Thus, the constantly applied current, i.e., the constant electron flow, will lead to the

formation of further LiO_2 , which is followed by (the uncatalyzed) chemical or electrochemical generation of Li_2O_2 . Such an activity was observed for the $\alpha\text{-Mn}_2\text{O}_3$ catalyst in this work. The change of the ORR pathway by this catalyst is mainly attributed to the particle morphology and the presence of surface Mn^{3+} ions. An ideal catalyst for reversible ORR processes could therefore be any transition metal oxide, which (i) consists of large and mesoporous particles, thus decreasing the influence of the carbon substrate on the ORR mechanism, (ii) provides O_2 adsorption and redox centers ($\text{Me}^{z+}/\text{Me}^{(1+z)+}$) on the particle surface and (iii) exhibits a low concentration of oxygen vacancies in its structure to prevent dissociative O_2 adsorption.

The proposals made in this work concerning the influence of surface redox centers of transition metal oxide catalysts for the ORR could be further investigated by surface analysis characterization methods, such as *in situ*-X-ray photoelectron spectroscopy (XPS). In addition, electrochemical analysis (e.g., CV, LSV and impedance spectroscopy) should be carried out in combination with *in situ* techniques, such as Raman and IR spectroscopy, to identify the ORR products and exclude possible electrolyte decomposition. Here, the commonly used method of galvanostatic cycling does not give sufficient insight into the reaction processes occurring during discharge and charge of the Li/air system.

References

- [1] P.G. Bruce, S.A. Freunberger, L.J. Hardwick, J.-M. Tarascon, Li-O₂ and Li-S batteries with high energy storage., *Nat. Mater.* 11 (2012) 19–29. doi:10.1038/nmat3191.
- [2] J. Christensen, P. Albertus, R.S. Sanchez-Carrera, T. Lohmann, B. Kozinsky, R. Liedtke, et al., A critical review of Li/air batteries, *J. Electrochem. Soc.* 159 (2012) R1–R30. doi:10.1149/2.086202jes.
- [3] K.M. Abraham, Z. Jiang, A polymer electrolyte-based rechargeable lithium/oxygen battery, *J. Electrochem. Soc.* 143 (1996) 1–5. <http://jes.ecsdl.org/content/143/1/1.short>.
- [4] G. Girishkumar, B.D. McCloskey, A.C. Luntz, S. Swanson, W. Wilcke, Lithium-air battery: Promise and challenges, *J. Phys. Chem. Lett.* 1 (2010) 2193–2203. doi:10.1021/jz1005384.
- [5] J. Lu, L. Li, J. Park, Y. Sun, F. Wu, K. Amine, Aprotic and aqueous Li-O₂ batteries, *Chem. Rev.* 114 (2014) 5611–5640. doi:10.1021/cr400573b.
- [6] J.P. Zheng, R.Y. Liang, M.A. Hendrickson, E.J. Plichta, Theoretical energy density of Li-air batteries, *J. Electrochem. Soc.* 155 (2008) A432–A437. doi:10.1149/1.2901961.
- [7] J. Wang, Y. Li, X. Sun, Challenges and opportunities of nanostructured materials for aprotic rechargeable lithium–air batteries, *Nano Energy.* 2 (2013) 443–467. doi:10.1016/j.nanoen.2012.11.014.
- [8] N. Garcia-Araez, P. Novák, Critical aspects in the development of lithium-air batteries, *J. Solid State Electrochem.* 17 (2013) 1793–1807. doi:10.1007/s10008-013-1999-1.
- [9] C.O. Laoire, S. Mukerjee, K.M. Abraham, E.J. Plichta, M.A. Hendrickson, Elucidating the mechanism of oxygen reduction for lithium-air battery applications, *J. Phys. Chem. C.* 113 (2009) 20127–20134. doi:10.1021/jp908090s.

References

- [10] C.O. Laoire, S. Mukerjee, K.M. Abraham, E.J. Plichta, M.A. Hendrickson, Influence of nonaqueous solvents on the electrochemistry of oxygen in the rechargeable lithium-air battery, *J. Phys. Chem. C*. 114 (2010) 9178–9186. doi:10.1021/jp102019y.
- [11] Y.-C. Lu, D.G. Kwabi, K.P.C. Yao, J.R. Harding, J. Zhou, L. Zuin, et al., The discharge rate capability of rechargeable Li-O₂ batteries, *Energy Environ. Sci.* 4 (2011) 2999–3007. doi:10.1039/c1ee01500a.
- [12] B.D. McCloskey, D.S. Bethune, R.M. Shelby, T. Mori, R. Scheffler, A. Speidel, et al., Limitations in rechargeability of Li-O₂ batteries and possible origins, *J. Phys. Chem. Lett.* 3 (2012) 3043–3047. doi:10.1021/jz301359t.
- [13] C.O. Laoire, S. Mukerjee, E.J. Plichta, M.A. Hendrickson, K.M. Abraham, Rechargeable lithium/TEGDME-LiPF₆/O₂ battery, *J. Electrochem. Soc.* 158 (2011) A302–A308. doi:10.1149/1.3531981.
- [14] Z. Peng, S.A. Freunberger, L.J. Hardwick, Y. Chen, V. Giordani, F. Bardé, et al., Oxygen reactions in a non-aqueous Li⁺ electrolyte., *Angew. Chemie Int. Ed.* 50 (2011) 6351–6355. doi:10.1002/anie.201100879.
- [15] L.J. Hardwick, P.G. Bruce, The pursuit of rechargeable non-aqueous lithium-oxygen battery cathodes, *Curr. Opin. Solid State Mater. Sci.* 16 (2012) 178–185. doi:10.1016/j.cossms.2012.04.001.
- [16] S. Meini, N. Tsiouvaras, K.U. Schwenke, M. Piana, H. Beyer, L. Lange, et al., Rechargeability of Li-air cathodes pre-filled with discharge products using an ether-based electrolyte solution: Implications for cycle-life of Li-air cells., *Phys. Chem. Chem. Phys.* 15 (2013) 11478–11493. doi:10.1039/c3cp51112j.
- [17] T. Ogasawara, A. Débart, M. Holzapfel, P. Novák, P.G. Bruce, Rechargeable Li₂O₂ electrode for lithium batteries., *J. Am. Chem. Soc.* 128 (2006) 1390–1393. doi:10.1021/ja056811q.

-
- [18] Y.-C. Lu, H.A. Gasteiger, M.C. Parent, V. Chiloyan, Y. Shao-Horn, The influence of catalysts on discharge and charge voltages of rechargeable Li-oxygen batteries, *Electrochem. Solid-State Lett.* 13 (2010) A69–A72. doi:10.1149/1.3363047.
- [19] G.K.P. Dathar, W.A. Shelton, Y. Xu, Trends in the catalytic activity of transition metals for the oxygen reduction reaction by lithium, *J. Phys. Chem. Lett.* 3 (2012) 891–895. doi:10.1021/jz300142y.
- [20] B.D. McCloskey, R. Scheffler, A. Speidel, D.S. Bethune, R.M. Shelby, A.C. Luntz, On the efficacy of electrocatalysis in nonaqueous Li-O₂ batteries., *J. Am. Chem. Soc.* 133 (2011) 18038–18041. doi:10.1021/ja207229n.
- [21] Y. Xu, W.A. Shelton, O₂ reduction by lithium on Au(111) and Pt(111), *J. Chem. Phys.* 133 (2010) 024703/1–0247031/9. doi:10.1063/1.3447381.
- [22] Y.-C. Lu, H.A. Gasteiger, E. Crumlin, R. McGuire, Y. Shao-Horn, Electrocatalytic activity studies of select metal surfaces and implications in Li-air batteries, *J. Electrochem. Soc.* 157 (2010) A1016–A1025. doi:10.1149/1.3462981.
- [23] Y.-C. Lu, H.A. Gasteiger, Y. Shao-Horn, Catalytic activity trends of oxygen reduction reaction for nonaqueous Li-air batteries., *J. Am. Chem. Soc.* 133 (2011) 19048–19051. doi:10.1021/ja208608s.
- [24] R.G. Pearson, Hard and soft acids and bases, *J. Am. Chem. Soc.* 85 (1963) 3533–3539. doi:10.1021/ja00905a001.
- [25] J. Yang, D. Zhai, H.-H. Wang, K.C. Lau, J.A. Schlueter, P. Du, et al., Evidence for lithium superoxide-like species in the discharge product of a Li-O₂ battery., *Phys. Chem. Chem. Phys.* 15 (2013) 3764–3771. doi:10.1039/c3cp00069a.
- [26] G.A. Elia, J. Park, B. Scrosati, Y. Sun, J. Hassoun, Investigation of the carbon electrode changes during lithium oxygen cell operation in a tetraglyme-based electrolyte, *Electrochem. Commun.* 34 (2013) 250–253. doi:10.1016/j.elecom.2013.06.024.

References

- [27] M.J. Trahan, S. Mukerjee, E.J. Plichta, M.A. Hendrickson, K.M. Abraham, Studies of Li-air cells utilizing dimethyl sulfoxide-based electrolyte, *J. Electrochem. Soc.* 160 (2012) A259–A267. doi:10.1149/2.048302jes.
- [28] E.J. Calvo, N. Mozhzhukhina, A rotating ring disk electrode study of the oxygen reduction reaction in lithium containing non aqueous electrolyte, *Electrochem. Commun.* 31 (2013) 56–58. doi:10.1016/j.elecom.2013.03.005.
- [29] W.R. Torres, A.Y. Tesio, E.J. Calvo, Solvent co-deposition during oxygen reduction on Au in DMSO LiPF₆, *Electrochem. Commun.* 49 (2014) 38–41. doi:10.1016/j.elecom.2014.09.017.
- [30] B.M. Gallant, D.G. Kwabi, R.R. Mitchell, J. Zhou, C.V. Thompson, Y. Shao-Horn, Influence of Li₂O₂ morphology on oxygen reduction and evolution kinetics in Li-O₂ batteries, *Energy Environ. Sci.* 6 (2013) 2518–2528. doi:10.1039/c3ee40998h.
- [31] G.A. Elia, J. Hassoun, W.-J. Kwak, Y.-K. Sun, B. Scrosati, F. Mueller, et al., An advanced lithium-air battery exploiting an ionic liquid-based electrolyte., *Nano Lett.* 14 (2014) 6572–6577. doi:10.1021/nl5031985.
- [32] F. Mizuno, K. Takechi, S. Higashi, T. Shiga, T. Shiotsuki, N. Takazawa, et al., Cathode reaction mechanism of non-aqueous Li-O₂ batteries with highly oxygen radical stable electrolyte solvent, *J. Power Sources.* 228 (2013) 47–56. doi:10.1016/j.jpowsour.2012.11.077.
- [33] X.-J. Huang, E.I. Rogers, C. Hardacre, R.G. Compton, The reduction of oxygen in various room temperature ionic liquids in the temperature range 293–318 K: Exploring the applicability of the Stokes-Einstein relationship in room temperature ionic liquids., *J. Phys. Chem. B.* 113 (2009) 8953–8959. doi:10.1021/jp903148w.

- [34] M. Hayyan, F.S. Mjalli, M.A. Hashim, I.M. AlNashef, X.M. Tan, Electrochemical reduction of dioxygen in bis (trifluoromethylsulfonyl) imide based ionic liquids, *J. Electroanal. Chem.* 657 (2011) 150–157. doi:10.1016/j.jelechem.2011.04.008.
- [35] Y. Katayama, K. Sekiguchi, M. Yamagata, T. Miura, Electrochemical behavior of oxygen/superoxide ion couple in 1-butyl-1-methylpyrrolidinium bis(trifluoromethylsulfonyl)imide room-temperature molten salt, *J. Electrochem. Soc.* 152 (2005) E247–E250. doi:10.1149/1.1946530.
- [36] D. Zhang, T. Okajima, F. Matsumoto, T. Ohsaka, Electroreduction of dioxygen in 1-n-alkyl-3-methylimidazolium tetrafluoroborate room-temperature ionic liquids, *J. Electrochem. Soc.* 151 (2004) D31–D37. doi:10.1149/1.1649748.
- [37] M. Taige, D. Hilbert, T.J.S. Schubert, Mixtures of ionic liquids as possible electrolytes for lithium ion batteries, *Zeitschrift für Phys. Chemie.* 226 (2012) 129–139. doi:10.1524/zpch.2012.0161.
- [38] K. Xu, Nonaqueous liquid electrolytes for lithium-based rechargeable batteries, *Chem. Rev.* 104 (2004) 4303–4418. doi:10.1021/cr030203g.
- [39] R. Black, S.H. Oh, J.-H. Lee, T. Yim, B. Adams, L.F. Nazar, Screening for superoxide reactivity in Li-O₂ batteries: Effect on Li₂O₂/LiOH crystallization., *J. Am. Chem. Soc.* 134 (2012) 2902–2905. doi:10.1021/ja2111543.
- [40] D.T. Sawyer, J.L. Roberts, Electrochemistry of oxygen and superoxide ion in dimethylsulfoxide at platinum, gold and mercury electrodes, *J. Electroanal. Chem.* 12 (1966) 90–101. doi:10.1016/0022-0728(66)80021-9.
- [41] X. Lin, X. Lu, T. Huang, Z. Liu, A. Yu, Binder-free nitrogen-doped carbon nanotubes electrodes for lithium-oxygen batteries, *J. Power Sources.* 242 (2013) 855–859. doi:10.1016/j.jpowsour.2013.05.100.

References

- [42] F. Bardé, Y. Chen, L. Johnson, S. Schaltin, J. Fransaer, P.G. Bruce, Sulfone-based electrolytes for nonaqueous Li-O₂ batteries, *J. Phys. Chem. C*. 118 (2014) 18892–18898. doi:10.1021/jp5048198.
- [43] D. Xu, Z. Wang, J. Xu, L. Zhang, X. Zhang, Novel DMSO-based electrolyte for high performance rechargeable Li-O₂ batteries., *Chem. Commun.* 48 (2012) 6948–6950. doi:10.1039/c2cc32844e.
- [44] S.E. Herrera, A.Y. Tesio, R. Clarenc, E.J. Calvo, AFM study of oxygen reduction products on HOPG in the LiPF₆-DMSO electrolyte., *Phys. Chem. Chem. Phys.* 16 (2014) 9925–9929. doi:10.1039/c3cp54621g.
- [45] N. Mozhzhukhina, L.P. Méndez De Leo, E.J. Calvo, Infrared spectroscopy studies on stability of dimethyl sulfoxide for application in a Li-air battery, *J. Phys. Chem. C*. 117 (2013) 18375–18380. doi:10.1021/jp407221c.
- [46] R.S. Nicholson, Semiempirical procedure for measuring with stationary electrode polarography rates of chemical reactions involving the product of electron transfer., *Anal. Chem.* 38 (1966) 1406–1406. doi:10.1021/ac60242a030.
- [47] R. Guidelli, R.G. Compton, J.M. Feliu, E. Gileadi, J. Lipkowski, W. Schmickler, et al., Defining the transfer coefficient in electrochemistry: An assessment (IUPAC Technical Report), *Pure Appl. Chem.* 86 (2014) 245–258. doi:10.1515/pac-2014-5026.
- [48] A.J. Bard, L.R. Faulkner, *Electrochemical Methods: Fundamentals and Applications*, 2nd ed., John Wiley & Sons, 2001.
- [49] M.C. Lefebvre, Establishing the link between multistep electrochemical reaction mechanisms and experimental Tafel slopes, in: B.E. Conway, J.O. Bockris, R.E. White (Eds.), *Mod. Asp. Electrochem. Number 32*, 1st ed., Springer, New York, 1999: pp. 249–300.

- [50] B.E. Conway, J.O. Bockris, On the calculation of potential energy profile diagrams for processes in electrolytic metal deposition, *Electrochim. Acta.* 3 (1961) 340–366.
doi:10.1016/0013-4686(61)85009-3.
- [51] R.A. Marcus, On the theory of electrochemical and chemical electron transfer processes, *Can. J. Chem.* 37 (1959) 155–163.
doi:10.1139/v59-022.
- [52] J. Heinze, Cyclovoltammetrie – die „Spektroskopie“ des Elektrochemikers, *Angew. Chemie.* 96 (1984) 823–840.
doi:10.1002/ange.19840961104.
- [53] C.M.A. Brett, A.M.O. Brett, *Electrochemistry: Principles, Methods, and Applications*, 1st ed., Oxford University Press, USA, Oxford, 1993.
- [54] J.O. Bockris, A.K.N. Reddy, M. Gamboa-Aldeco, *Modern Electrochemistry, Vol. 2A – Fundamentals of Electrode Processes*, 2nd ed., Kluwer Academic Publishers, New York, 2002.
- [55] F.S. Gittleston, R.C. Sekol, G. Doubek, M. Linardi, A.D. Taylor, Catalyst and electrolyte synergy in Li-O₂ batteries., *Phys. Chem. Chem. Phys.* 16 (2014) 3230–3237.
doi:10.1039/c3cp54555e.
- [56] J.E.B. Randles, A cathode ray polarograph. Part II. – The current-voltage curves., *Trans. Faraday Soc.* 44 (1948) 327–338.
doi:10.1039/tf9484400322.
- [57] A. Ševčík, Oscillographic polarography with periodical triangular voltage, *Collect. Czechoslov. Chem. Commun.* 13 (1948) 349–377.
doi:10.1135/cccc19480349.
- [58] R.S. Nicholson, I. Shain, Theory of stationary electrode polarography. single scan and cyclic methods applied to reversible, irreversible, and kinetic systems., *Anal. Chem.* 36 (1964) 706–723.
doi:10.1021/ac60210a007.

References

- [59] C.J. Allen, S. Mukerjee, E.J. Plichta, M.A. Hendrickson, K.M. Abraham, Oxygen electrode rechargeability in an ionic liquid for the Li-air battery, *J. Phys. Chem. Lett.* 2 (2011) 2420–2424. doi:10.1021/jz201070t.
- [60] R. Guidelli, R.G. Compton, J.M. Feliu, E. Gileadi, J. Lipkowski, W. Schmickler, et al., Definition of the transfer coefficient in electrochemistry (IUPAC Recommendations 2014), *Pure Appl. Chem.* 86 (2014) 259–262. doi:10.1515/pac-2014-5025.
- [61] Y. Xu, M. Mavrikakis, Adsorption and dissociation of O₂ on Ir(111), *J. Chem. Phys.* 116 (2002) 10846. doi:10.1063/1.1479716.
- [62] S.L. Parrott, G. Praline, B.E. Koel, J.M. White, T.N. Taylor, Oxygen chemisorption on a stepped Ru (\sim 001) crystal, *J. Chem. Phys.* 71 (1979) 3352–3354.
- [63] C.-M. Chan, W.H. Weinberg, Low-energy electron diffraction structural analysis of the (2 \times 2) oxygen overlayer on the iridium (111) surface, *J. Chem. Phys.* 71 (1979) 2788. doi:10.1063/1.438683.
- [64] R. Imbihl, J.E. Demuth, Adsorption of oxygen on a Pd(111) surface studied by high resolution electron energy loss spectroscopy (EELS), *Surf. Sci.* 173 (1986) 395–410. doi:10.1016/0039-6028(86)90198-6.
- [65] C.W. Tucker, Low-energy electron diffraction studies of gas adsorption on platinum (100), (110), and (111) surfaces, *J. Appl. Phys.* 35 (1964) 1897. doi:10.1063/1.1713766.
- [66] Z. Chen, D. Higgins, A. Yu, L. Zhang, J. Zhang, A review on non-precious metal electrocatalysts for PEM fuel cells, *Energy Environ. Sci.* 4 (2011) 3167–3192. doi:10.1039/c0ee00558d.
- [67] Y. Feng, N. Alonso-Vante, Nonprecious metal catalysts for the molecular oxygen-reduction reaction, *Phys. Status Solidi B.* 245 (2008) 1792–1806. doi:10.1002/pssb.200879537.

- [68] K.P.C. Yao, Y.-C. Lu, C. V Amanchukwu, D.G. Kwabi, M. Risch, J. Zhou, et al., The influence of transition metal oxides on the kinetics of Li_2O_2 oxidation in Li- O_2 batteries: High activity of chromium oxides, *Phys. Chem. Chem. Phys.* 16 (2014) 2297–2304. doi:10.1039/c3cp53330a.
- [69] R.S. Kalubarme, M.-S. Cho, J.-K. Kim, C.-J. Park, Ceria based catalyst for cathode in non-aqueous electrolyte based Li/ O_2 batteries., *Nanotechnology*. 23 (2012) 435703/1–435703/11. doi:10.1088/0957-4484/23/43/435703.
- [70] H.W. Park, D.U. Lee, L.F. Nazar, Z. Chen, Oxygen reduction reaction using MnO_2 nanotubes/nitrogen-doped exfoliated graphene hybrid catalyst for Li- O_2 battery applications, *J. Electrochem. Soc.* 160 (2012) A344–A350. doi:10.1149/2.086302jes.
- [71] Z. Jian, P. Liu, F. Li, P. He, X. Guo, M. Chen, et al., Core-shell-structured CNT@ RuO_2 composite as a high-performance cathode catalyst for rechargeable Li- O_2 batteries., *Angew. Chemie Int. Ed.* 53 (2014) 442–446. doi:10.1002/anie.201307976.
- [72] J. Suntivich, H.A. Gasteiger, N. Yabuuchi, Y. Shao-Horn, Electrocatalytic measurement methodology of oxide catalysts using a thin-film rotating disk electrode, *J. Electrochem. Soc.* 157 (2010) B1263–B1268. doi:10.1149/1.3456630.
- [73] Y. Hu, X. Han, Q. Zhao, J. Du, F. Cheng, J. Chen, Porous perovskite calcium-manganese oxide microspheres as an efficient catalyst for rechargeable sodium-oxygen batteries, *J. Mater. Chem. A*. 3 (2015) 3320–3324. doi:10.1039/C4TA06287F.
- [74] M. Fayette, A. Nelson, R.D. Robinson, Electrophoretic deposition improves catalytic performance of Co_3O_4 nanoparticles for oxygen reduction/oxygen evolution reactions, *J. Mater. Chem. A*. 3 (2015) 4274–4283. doi:10.1039/C4TA04189E.

References

- [75] Y.-X. Zhang, X. Guo, X. Zhai, Y.-M. Yan, K.-N. Sun, Diethylenetriamine (DETA)-assisted anchoring of Co_3O_4 nanorods on carbon nanotubes as efficient electrocatalysts for the oxygen evolution reaction, *J. Mater. Chem. A*. **3** (2014) 1761–1768. doi:10.1039/C4TA04641B.
- [76] H.G. Sanchez Casalongue, M.L. Ng, S. Kaya, D. Friebel, H. Ogasawara, A. Nilsson, *In situ* observation of surface species on iridium oxide nanoparticles during the oxygen evolution reaction, *Angew. Chemie Int. Ed.* **53** (2014) 7169–7172. doi:10.1002/anie.201402311.
- [77] J.S. Hummelshøj, A.C. Luntz, J.K. Nørskov, Theoretical evidence for low kinetic overpotentials in Li-O_2 electrochemistry., *J. Chem. Phys.* **138** (2013) 034703/1–034703/12. doi:10.1063/1.4773242.
- [78] A. Débart, J. Bao, G. Armstrong, P.G. Bruce, An O_2 cathode for rechargeable lithium batteries: The effect of a catalyst, *J. Power Sources*. **174** (2007) 1177–1182. doi:10.1016/j.jpowsour.2007.06.180.
- [79] L. Jin, L. Xu, C. Morein, C. Chen, M. Lai, S. Dharmarathna, et al., Titanium containing $\gamma\text{-MnO}_2$ (TM) hollow spheres: One-step synthesis and catalytic activities in Li/air batteries and oxidative chemical reactions, *Adv. Funct. Mater.* **20** (2010) 3373–3382. doi:10.1002/adfm.201001080.
- [80] H. Cheng, K. Scott, Selection of oxygen reduction catalysts for rechargeable lithium-air batteries – Metal or oxide?, *Appl. Catal. B Environ.* **108-109** (2011) 140–151. doi:10.1016/j.apcatb.2011.08.021.
- [81] J.E. Post, Manganese oxide minerals: Crystal structures and economic and environmental significance, *Proc. Natl. Acad. Sci.* **96** (1999) 3447–3454. doi:10.1073/pnas.96.7.3447.

- [82] M.A. Subramanian, G. Aravamudan, G.V. Subba Rao, Oxide pyrochlores – A review, *Prog. Solid State Chem.* 15 (1983) 55–143. doi:10.1016/0079-6786(83)90001-8.
- [83] S.H. Oh, R. Black, E. Pomerantseva, J. Lee, L.F. Nazar, Synthesis of a metallic mesoporous pyrochlore as a catalyst for lithium-O₂ batteries., *Nat. Chem.* 4 (2012) 1004–1010. doi:10.1038/nchem.1499.
- [84] H.S. Horowitz, J.M. Longo, H.H. Horowitz, Oxygen electrocatalysis on some oxide pyrochlores, *J. Electrochem. Soc.* 130 (1983) 1851–1859. doi:10.1149/1.2120111.
- [85] T. Akazawa, Y. Inaguma, T. Katsumata, K. Hiraki, T. Takahashi, Flux growth and physical properties of pyrochlore Pb₂Ru₂O_{6.5} single crystals, *J. Cryst. Growth.* 271 (2004) 445–449. doi:10.1016/j.jcrysgro.2004.08.002.
- [86] C.J. Howard, T.M. Sabine, F. Dickson, Structural and thermal parameters for rutile and anatase, *Acta Crystallogr. Sect. B Struct. Sci.* 47 (1991) 462–468. doi:10.1107/S010876819100335X.
- [87] M. Calatayud, F. Tielens, Exploring metal oxides: A theoretical approach, in: E. Santos, W. Schmickler (Eds.), *Catal. Electrochem. From Fundam. to Strateg. Fuel Cell Dev.*, 1st ed., John Wiley & Sons, Inc., Hoboken, New Jersey, 2011: pp. 375–426.
- [88] M.V. Ganduglia-Pirovano, A. Hofmann, J. Sauer, Oxygen vacancies in transition metal and rare earth oxides: Current state of understanding and remaining challenges, *Surf. Sci. Rep.* 62 (2007) 219–270. doi:10.1016/j.surfrep.2007.03.002.
- [89] M. Augustin, Formation of reaction-inhibiting adsorbed side products during CO oxidation on supported Au/TiO₂ and Au/Ti_xSi_{1-x}O₂ catalysts based on mesoporous materials, Ulm University, 2010.
- [90] M. Valden, X. Lai, D.W. Goodman, Onset of catalytic activity of gold clusters on titania with the appearance of nonmetallic properties, *Science.* 281 (1998) 1647–1650. doi:10.1126/science.281.5383.1647.

References

- [91] B. Santara, P.K. Giri, K. Imakita, M. Fujii, Microscopic origin of lattice contraction and expansion in undoped rutile TiO_2 nanostructures, *J. Phys. D. Appl. Phys.* 47 (2014) 215302/1–215302/13. doi:10.1088/0022-3727/47/21/215302.
- [92] V. Giordani, S.A. Freunberger, P.G. Bruce, J.-M. Tarascon, D. Larcher, H_2O_2 decomposition reaction as selecting tool for catalysts in Li- O_2 cells, *Electrochem. Solid-State Lett.* 13 (2010) A180–A183. doi:10.1149/1.3494045.
- [93] K.-N. Jung, A. Riaz, S.-B. Lee, T.-H. Lim, S.-J. Park, R.-H. Song, et al., Urchin-like $\alpha\text{-MnO}_2$ decorated with Au and Pd as a bi-functional catalyst for rechargeable lithium-oxygen batteries, *J. Power Sources.* 244 (2013) 328–335. doi:10.1016/j.jpowsour.2013.01.028.
- [94] J. Liu, R. Younesi, T. Gustafsson, K. Edström, J. Zhu, Pt/ $\alpha\text{-MnO}_2$ nanotube: A highly active electrocatalyst for Li- O_2 battery, *Nano Energy.* 10 (2014) 19–27. doi:10.1016/j.nanoen.2014.08.022.
- [95] A.K. Thapa, B. Pandit, H.S. Paudel, R. Thapa, S. Ida, J.B. Jasinski, et al., Polythiophene mesoporous birnessite- MnO_2 /Pd cathode air electrode for rechargeable Li-air battery, *Electrochim. Acta.* 127 (2014) 410–415. doi:10.1016/j.electacta.2014.02.071.
- [96] Y. Huang, Y. Lin, W. Li, Controllable syntheses of $\alpha\text{-}$ and $\delta\text{-MnO}_2$ as cathode catalysts for zinc-air battery, *Electrochim. Acta.* 99 (2013) 161–165. doi:10.1016/j.electacta.2013.03.088.
- [97] R.S. Kalubarme, C.-H. Ahn, C.-J. Park, Electrochemical characteristics of graphene/manganese oxide composite catalyst for Li-oxygen rechargeable batteries, *Scr. Mater.* 68 (2013) 619–622. doi:10.1016/j.scriptamat.2012.12.020.
- [98] L. Chen, X. Guo, J. Han, P. Liu, X. Xu, A. Hirata, et al., Nanoporous metal/oxide hybrid materials for rechargeable lithium-oxygen batteries, *J. Mater. Chem. A.* 3 (2015) 3620–3626. doi:10.1039/C4TA05738D.

- [99] S. Chen, G. Liu, H. Yadegari, H. Wang, S.Z. Qiao, Three-dimensional MnO_2 ultrathin nanosheet aerogels for high-performance Li- O_2 batteries, *J. Mater. Chem. A.* (2015) 1–5. doi:10.1039/C5TA00004A.
- [100] H. Geaney, C. O'Dwyer, Electrochemical investigation of the role of MnO_2 nanorod catalysts in water containing and anhydrous electrolytes for Li- O_2 battery applications, *Phys. Chem. Chem. Phys.* (2015). doi:10.1039/C4CP05785F.
- [101] N. Tang, X. Tian, C. Yang, Z. Pi, Q. Han, Facile synthesis of $\alpha\text{-MnO}_2$ nanorods for high-performance alkaline batteries, *J. Phys. Chem. Solids.* 71 (2010) 258–262. doi:10.1016/j.jpcs.2009.11.016.
- [102] J. Luo, Q. Zhang, J. Garcia-Martinez, S.L. Suib, Adsorptive and acidic properties, reversible lattice oxygen evolution, and catalytic mechanism of cryptomelane-type manganese oxides as oxidation catalysts., *J. Am. Chem. Soc.* 130 (2008) 3198–3207. doi:10.1021/ja077706e.
- [103] L. Liu, H. Yang, J. Wei, Y. Yang, Controllable synthesis of monodisperse Mn_3O_4 and Mn_2O_3 nanostructures via a solvothermal route, *Mater. Lett.* 65 (2011) 694–697. doi:10.1016/j.matlet.2010.11.042.
- [104] M. Wang, L. Cheng, Q. Li, S. Wang, Two-dimensional nanosheets associated with one-dimensional single-crystalline nanorods self-assembled into three-dimensional flower-like Mn_3O_4 hierarchical architectures, *Phys. Chem. Chem. Phys.* 16 (2014) 21742–21746. doi:10.1039/C4CP03407D.
- [105] M. Augustin, D. Fenske, I. Bardenhagen, A. Westphal, M. Knipper, T. Plaggenborg, et al., Manganese oxide phases and morphologies: A study on calcination temperature and atmospheric dependence, *Beilstein J. Nanotechnol.* 6 (2015) 47–59. doi:10.3762/bjnano.6.6.
- [106] F. Kapteljn, L. Sngoredjo, A. Andreml, Activity and selectivity of pure manganese oxides in the selective catalytic reduction of nitric oxide with ammonia, *Appl. Catal. B Environ.* 3 (1994) 173–189. doi:10.1016/0926-3373(93)E0034-9

References

- [107] S. Lei, K. Tang, Z. Fang, Q. Liu, H. Zheng, Preparation of α - Mn_2O_3 and MnO from thermal decomposition of MnCO_3 and control of morphology, *Mater. Lett.* 60 (2006) 53–56. doi:10.1016/j.matlet.2005.07.070.
- [108] L. Liu, Z. Yang, H. Liang, H. Yang, Y. Yang, Shape-controlled synthesis of manganese oxide nanoplates by a polyol-based precursor route, *Mater. Lett.* 64 (2010) 891–893. doi:10.1016/j.matlet.2010.01.054.
- [109] C.B. Azzoni, M.C. Mozzati, P. Galinetto, A. Paleari, V. Massarotti, D. Capsoni, Thermal stability and structural transition of metastable Mn_5O_8 : *In situ* micro-Raman study, *Solid State Commun.* 112 (1999) 375–378. doi:10.1016/S0038-1098(99)00368-3.
- [110] B.L. Cushing, V.L. Kolesnichenko, C.J. O'Connor, Recent advances in the liquid-phase syntheses of inorganic nanoparticles, *Chem. Rev.* 104 (2004) 3893–3946. doi:10.1021/cr030027b.
- [111] Q. Javed, W. Feng-Ping, M.Y. Rafique, A.M. Toufiq, M.Z. Iqbal, Canted antiferromagnetic and optical properties of nanostructures of Mn_2O_3 prepared by hydrothermal synthesis, *Chinese Phys. B.* 21 (2012) 117311–117317. doi:10.1088/1674-1056/21/11/117311.
- [112] Z.-Y. Yuan, T.-Z. Ren, G. Du, B.-L. Su, A facile preparation of single-crystalline α - Mn_2O_3 nanorods by ammonia-hydrothermal treatment of MnO_2 , *Chem. Phys. Lett.* 389 (2004) 83–86. doi:10.1016/j.cplett.2004.03.064.
- [113] H. Dhaouadi, O. Ghodbane, F. Hosni, F. Touati, Mn_3O_4 nanoparticles: Synthesis, characterization, and dielectric properties, *ISRN Spectrosc.* 2012 (2012) 1–8. doi:10.5402/2012/706398.
- [114] B. Gillot, M. El Guendouzi, M. Laarj, Particle size effects on the oxidation – reduction behavior of Mn_3O_4 hausmannite, *Mater. Chem. Phys.* 70 (2001) 54–60. doi:10.1016/S0254-0584(00)00473-9.

- [115] Z. Gui, R. Fan, W. Mo, X. Chen, L. Yang, Y. Hu, Synthesis and characterization of reduced transition metal oxides and nanophase metals with hydrazine in aqueous solution, *Mater. Res. Bull.* 38 (2003) 169–176. doi:10.1016/S0025-5408(02)00983-2.
- [116] L. Dimesso, L. Heider, H. Hahn, Synthesis of nanocrystalline Mn-oxides by gas condensation, *Solid State Ionics*. 123 (1999) 39–46. doi: 10.1016/s0167-2738(99)00107-1.
- [117] D. Larcher, G. Sudant, R. Patrice, J.-M. Tarascon, Some insights on the use of polyols-based metal alkoxides powders as precursors for tailored metal-oxides particles, *Chem. Mater.* 15 (2003) 3543–3551. doi:10.1021/cm030048m.
- [118] W. Feitknecht, Einfluß der Teilchengröße auf den Mechanismus von Festkörperreaktionen, *Pure Appl. Chem.* 9 (1964) 423–440. <http://www.iupac.org/publications/pac/pdf/1964/pdf/0903x0423.pdf>.
- [119] H.R. Oswald, M.J. Wampetich, Die Kristallstrukturen von Mn_5O_8 und $Cd_2Mn_3O_8$, *Helv. Chim. Acta.* 50 (1967) 2023–2034. doi:10.1002/hlca.19670500736.
- [120] A. Punnoose, H. Magnone, M.S. Seehra, Synthesis and antiferromagnetism of Mn_5O_8 , *IEEE Trans. Magn.* 37 (2001) 2150–2152. doi:10.1109/20.951107.
- [121] S. Thota, B. Prasad, J. Kumar, Formation and magnetic behaviour of manganese oxide nanoparticles, *Mater. Sci. Eng. B.* 167 (2010) 153–160. doi:10.1016/j.mseb.2010.01.049.
- [122] A. Patterson, The Scherrer formula for X-ray particle size determination, *Phys. Rev.* 56 (1939) 978–982. doi:10.1103/PhysRev.56.978.
- [123] G. Caglioti, A. Paoletti, F.P. Ricci, Choice of collimators for a crystal spectrometer for neutron diffraction, *Nucl. Instruments.* 3 (1958) 223–228. doi:10.1016/0369-643X(58)90029-X.

References

- [124] V. Pecharsky, P. Zavalij, *Fundamentals of Powder Diffraction and Structural Characterization of Materials*, 2nd ed., Springer Science & Business Media, 2009.
- [125] S. Ceré, M. Vazquez, S.R. de Sánchez, D.J. Schiffrin, Surface redox catalysis and reduction kinetics of oxygen on copper-nickel alloys, *J. Electroanal. Chem.* 505 (2001) 118–124.
doi:10.1016/S0022-0728(01)00469-7.
- [126] E. Mendelovici, R. Villalba, A. Sagarzazu, Synthesis and characteristics of Fe-Mn glycerate (alkoxides), new precursors of ferrite structures, *J. Mater. Sci. Lett.* 9 (1990) 28–31. doi:10.1007/BF00722859.
- [127] M. Augustin, O. Yezerska, J. Derendorf, M. Knipper, D. Fenske, T. Plaggenborg, et al., Colloidal manganese oxide nanoparticles as bifunctional catalysts for oxygen reduction and evolution reactions in lithium/air batteries, *ECS Trans.* 45 (2013) 1–10.
doi:10.1149/04527.0001ecst.
- [128] Y. Sun, X. Hu, W. Luo, Y. Huang, Porous carbon-modified MnO disks prepared by a microwave-polyol process and their superior lithium-ion storage properties, *J. Mater. Chem.* 22 (2012) 19190–19195.
doi:10.1039/c2jm32036c.
- [129] N. Chakroune, G. Viau, S. Ammar, N. Jouini, P. Gredin, M.J. Vaulay, et al., Synthesis, characterization and magnetic properties of disk-shaped particles of a cobalt alkoxide: $\text{Co}^{\text{II}}(\text{C}_2\text{H}_4\text{O}_2)$, *New J. Chem.* 29 (2005) 355–361. doi:10.1039/b411117f.
- [130] G. Aminoff, XXVIII. Über die Kristallstruktur von Hausmannit (MnMn_2O_4), *Zeitschrift für Krist. – Cryst. Mater.* 64 (1926) 475–490.
doi:10.1524/zkri.1926.64.1.475.
- [131] T.-Z. Ren, Z.-Y. Yuan, W. Hu, X. Zou, Single crystal manganese oxide hexagonal plates with regulated mesoporous structures, *Microporous Mesoporous Mater.* 112 (2008) 467–473.
doi:10.1016/j.micromeso.2007.10.025.

- [132] X. Jiang, Y. Wang, T. Herricks, Y. Xia, Ethylene glycol-mediated synthesis of metal oxide nanowires, *J. Mater. Chem.* 14 (2004) 695–703. doi:10.1039/b313938g.
- [133] Y. Zhang, Y. Yan, X. Wang, G. Li, D. Deng, L. Jiang, et al., Facile synthesis of porous Mn_2O_3 nanoplates and their electrochemical behavior as anode materials for lithium ion batteries., *Chem. – A Eur. J.* 20 (2014) 6126–6130. doi:10.1002/chem.201304935.
- [134] E.M. Logothetis, K. Park, The electrical conductivity of Mn_3O_4 , *Solid State Commun.* 16 (1975) 909–912. doi:10.1016/0038-1098(75)90891-1.
- [135] M. Augustin, O. Yezerska, D. Fenske, I. Bardenhagen, A. Westphal, M. Knipper, et al., Mechanistic study on the activity of manganese oxide catalysts for oxygen reduction reaction in an aprotic electrolyte, *Electrochim. Acta.* 158 (2015) 383–389. doi:10.1016/j.electacta.2015.01.163.
- [136] B.D. McCloskey, R. Scheffler, A. Speidel, G. Girishkumar, A.C. Luntz, On the mechanism of nonaqueous Li-O_2 electrochemistry on C and its kinetic overpotentials: Some implications for Li-air batteries, *J. Phys. Chem. C.* 116 (2012) 23897–23905. doi:10.1021/jp306680f.
- [137] D.T. Sawyer, G. Chiericato, C.T. Angelis, E.J. Nanni, T. Tsuchiya, Effects of media and electrode materials on the electrochemical reduction of dioxygen, *Anal. Chem.* 54 (1982) 1720–1724. doi:10.1021/ac00248a014.
- [138] Y.-C. Lu, B.M. Gallant, D.G. Kwabi, J.R. Harding, R.R. Mitchell, M.S. Whittingham, et al., Lithium-oxygen batteries: Bridging mechanistic understanding and battery performance, *Energy Environ. Sci.* 6 (2013) 750–768. doi:10.1039/c3ee23966g.
- [139] M.L. Calegari, F.H.B. Lima, E.A. Ticianelli, Oxygen reduction reaction on nanosized manganese oxide particles dispersed on carbon in alkaline solutions, *J. Power Sources.* 158 (2006) 735–739. doi:10.1016/j.jpowsour.2005.08.048.

References

- [140] D.F. Baker, R.H. Bragg, The electrical conductivity and Hall effect of glassy carbon, *J. Non. Cryst. Solids*. 58 (1983) 57–69.
doi:10.1016/0022-3093(83)90103-5.
- [141] J.J. Fontanella, M.C. Wintersgill, R.S. Chen, Y. Wu, S.G. Greenbaum, Charge transport and water molecular motion in variable molecular weight nafion membranes: High pressure electrical conductivity and NMR, *Electrochim. Acta*. 40 (1995) 2321–2326.
doi:10.1016/0013-4686(95)00186-I.
- [142] D. Pantea, H. Darmstadt, S. Kaliaguine, C. Roy, Electrical conductivity of conductive carbon blacks: Influence of surface chemistry and topology, *Appl. Surf. Sci.* 217 (2003) 181–193.
doi:10.1016/S0169-4332(03)00550-6.
- [143] F.H.B. Lima, M.L. Calegari, E.A. Ticianelli, Electrocatalytic activity of manganese oxides prepared by thermal decomposition for oxygen reduction, *Electrochim. Acta*. 52 (2007) 3732–3738.
doi:10.1016/j.electacta.2006.10.047.
- [144] J. Perez, E.R. Gonzalez, E.A. Ticianelli, Oxygen electrocatalysis on thin porous coating rotating platinum electrodes, *Electrochim. Acta*. 44 (1998) 1329–1339. doi:10.1016/S0013-4686(98)00255-2.
- [145] C.W. Lee, Effect of binary conductive agents in spinel LiMn_2O_4 cathodes on electrochemical performance of Li-ion batteries, *J. Ind. Eng. Chem.* 12 (2006) 967–971.
<http://infosys.korea.ac.kr/PDF/JIEC/IE12/IE12-6-0967.pdf>.
- [146] M. Kumari, D. Kumar Sharma, Synthesis of (1-ethyl-2-phenyl-1,4-dihydroquinolin-4-yl)-(2,4,6-trimethylphenyl)-amine by electrochemical methods in aprotic media, *Croat. Chem. Acta*. 84 (2011) 455–460.
doi:10.5562/cca1855.

-
- [147] H.-Y. Su, Y. Gorlin, I.C. Man, F. Calle-Vallejo, J.K. Nørskov, T.F. Jaramillo, et al., Identifying active surface phases for metal oxide electrocatalysts: A study of manganese oxide bi-functional catalysts for oxygen reduction and water oxidation catalysis., *Phys. Chem. Chem. Phys.* 14 (2012) 14010–14022. doi:10.1039/c2cp40841d.
- [148] D. Zhou, X. Lü, D. Liu, Electro-catalytic effect of manganese oxide on oxygen reduction at teflonbonded carbon electrode, *Trans. Nonferrous Met. Soc. China.* 16 (2006) 217–222. doi:10.1016/S1003-6326(06)60038-1.
- [149] R.S. Kalubarme, H.S. Jadhav, C.-N. Park, K.-N. Jung, K.-H. Shin, C.-J. Park, Nanostructured doped ceria for catalytic oxygen reduction and Li_2O_2 oxidation in non-aqueous electrolytes, *J. Mater. Chem. A.* 2 (2014) 13024–13032. doi:10.1039/C4TA01938E.
- [150] M. Haruta, Gold as a novel catalyst in the 21st century: Preparation, working mechanism and applications, *Gold Bull.* 37 (2004) 27–36. <http://link.springer.com/article/10.1007/BF03215514>.
- [151] J.H. Lee, Y.J. Sa, T.K. Kim, H.R. Moon, S.H. Joo, A transformative route to nanoporous manganese oxides of controlled oxidation states with identical textural properties, *J. Mater. Chem. A.* 2 (2014) 10435–10443. doi:10.1039/c4ta01272k.

Danksagung

Die vorliegende Arbeit wurde in der Zeit von April 2011 bis Juli 2015 in der Arbeitsgruppe Elektrische Energiespeicher, Fraunhofer IFAM, und dem Institut für Physik, Abteilung Energie- und Halbleiterforschung, Universität Oldenburg angefertigt.

An dieser Stelle möchte ich allen Personen danken, die mich in den letzten drei Jahren unterstützt und wesentlich zum Gelingen dieser Arbeit beigetragen haben.

Mein Dank gilt Herrn Prof. Dr. Parisi für die Möglichkeit der Bearbeitung dieser interessanten Aufgabenstellung und die Betreuung zum Gelingen dieser Arbeit. Die großen Freiheiten, die mir zur Umsetzung des Themas eingeräumt wurden, weiß ich sehr zu schätzen. Bei Herrn Prof. Dr. Busse bedanke ich mich für die große Unterstützung und die exzellenten Messbedingungen in seinem Institut, sowie für seine Bereitschaft diese Arbeit zu begutachten.

Ebenso möchte ich mich bei Frau Dr. Daniela Fenske für die Betreuung dieser Arbeit und die anregenden wissenschaftlichen Diskussionen bedanken. Weiterhin danke ich Herrn Dr. Thorsten Plaggenborg für die wissenschaftliche Beratung bei der Durchführung der Arbeit und die vielen kritischen Fragen und Anregungen. An dieser Stelle möchte ich mich sowohl bei ihnen als auch bei Frau Dr. Anne Westphal für die Hilfe bei der Korrektur des Dissertationsmanuskripts bedanken.

Frau Jun.-Prof. Kolny-Olesiak danke ich für die Betreuung der synthesechemischen Arbeiten und ihre Bereitschaft diese in einem wissenschaftlichen Rahmen zu diskutieren. Großer Dank gilt auch Herrn Dr. Martin Knipper für die Unterstützung bei XRD-Messungen. Darüber hinaus

danke ich Herrn Johannes Neumann vom Fraunhofer IFAM für die Durchführung der TGA-Messungen.

Allen Mitarbeitern der Arbeitsgruppe Parisi und der IFAM-Arbeitsgruppe in Oldenburg danke ich für die angenehme Arbeitsatmosphäre und die sehr gute Stimmung in den verschiedenen Laboren und Büros (der ist für dich, Ingo), die ich während meiner Promotionszeit bevölkert habe. Bei Magdalena „Maggie“ Bogacka und Christin Warns möchte ich mich neben der Einführung in die Künste der elektrochemischen Messtechnik und der Elektrodenpräparation für ihre reine Anwesenheit bedanken.

Ein riesengroßer Dank für die unermüdlichen Diskussionen über elektrochemische Fragestellungen geht an die wunderbare Frau Dr. Olga Yezerska, die in mir die Begeisterung für die Elektrochemie geweckt hat.

Außerdem möchte ich hiermit meinen Ex-IFAM-Kollegen Hauke Holst und Janis Derendorf für die reichhaltigen Erinnerungen an die guten alten Zeiten sowie die reine Freude an den guten neuen Zeiten danken. Auch Herr Dipl.-Ing. Ralf Meyer soll hier nicht unerwähnt bleiben, der musiktechnisch ein ganz Großer ist und mit Rat und Tat immer zur Seite steht, wenn es mal irgendwo brennt (metaphorisch gesprochen).

Meinem Vater und meinen beiden kleinen Geschwistern gilt großer Dank für die Unterstützung meines Tuns und die Ablenkung von meinem Tun, was so manches Mal für einen klaren Kopf gesorgt hat.

Nichts zu dieser Arbeit beigetragen haben (aber auch erwähnt werden wollen) meine ehemaligen Chemie-Kollegen in Ulm, die mich bei jedem Besuch mit offenen Armen empfangen. Simon, Dömy, Björn, Stehp: die hierbei zustande kommenden Wiedervereinigungen der *Muschelschubser*, des halben *Ponyhofs*, der *Comedian Inharmonists* und vieler weiterer äußerst verdächtiger Gruppierungen sind immer wieder eine wahre Freude. Besonders erwähnt sei hier der gute Claus M., der mir jedes Mal eine außerordentlich

gemütliche Heimstatt bietet und durch chaotische Spontaneität zu beeindrucken weiß.

Natürlich dürfen auch die Nordlichter von Next Energy nicht fehlen, deren ungebrochene Lebensfreude nur von ihrer Vorliebe fürs Kartenspielen übertroffen wird. Die Toleranz von Jan, Geischi und Martin gegenüber Instituts-Externen wie Steffen und mir auf der unendlichen Jagd nach mehr Tacken weiß ich sehr zu schätzen. Hierfür soll ich auch ein großes „Vielen vielen Danke!“ von Renate, Werner und Rollo ausrichten.

Zu guter Letzt möchte ich meiner Freundin Rany und ihrer Familie für die schier unendliche Geduld und das lecker Essen danken, die mir unter anderem von ihrer Seite entgegengebracht werden.

I SALUTE YOU !!!

Matthias Augustin

Hochheider Weg 207
26125 Oldenburg
matthias.augustin@uni-oldenburg.de

Persönliche Angaben

Geburtsdatum/-ort: 05. August 1984, Buxtehude
Familienstand: ledig
Staatsangehörigkeit: deutsch

Ausbildung

- 09/1996 – 06/2004 Gymnasium Halepighen-Schule, Buxtehude
Leistungskurse: Englisch und Biologie
Abschluss: Abitur (Note: 2,4)
- 05/2008 Vordiplom Chemie
- 10/2005 – 12/2010 Chemie-Studium an der Universität Ulm
Prüfungsfächer: Physikalische Chemie, Energietechnik,
Anorganische Chemie, Organische Chemie
Abschluss: Diplom-Chemiker (Note: 1,7)
Abschlussarbeit: *Formation of reaction-inhibiting adsorbed side products during CO oxidation on supported Au/TiO₂ and Au/Ti_xSi_{1-x}O₂ catalysts based on mesoporous materials*
- 04/2011 – 06/2015 Promotionsstudent und wissenschaftlicher Mitarbeiter am Fraunhofer IFAM, Abteilung Elektrische Energiespeicher und der Universität Oldenburg, Arbeitsgruppe für Energie- und Halbleiterforschung; Promotion bei Prof. J. Parisi
Abschlussarbeit: *The electrocatalytic ORR activity of nanostructured manganese oxides in aprotic media*

Veröffentlichungen, Zeitschriftenartikel

M. Augustin, O. Yezerka, J. Derendorf, M. Knipper, D. Fenske, T. Plaggenborg, J. Parisi, *Colloidal Manganese Oxide Nanoparticles as Bifunctional Catalysts for Oxygen Reduction and Evolution Reactions in Lithium/Air Batteries*, ECS Transactions, 45 (2013) 1-10

I. Bardenhagen, O. Yezerka, M. Augustin, D. Fenske, A. Wittstock, M. Bäumer, *In situ investigation of pore clogging during discharge of a Li/O₂ battery by electrochemical impedance spectroscopy*, Journal of Power Sources, 278 (2015) 255-264

M. Augustin, D. Fenske, I. Bardenhagen, A. Westphal, M. Knipper, T. Plaggenborg, J. Kolny-Olesiak, J. Parisi, *Manganese oxide phases and morphologies: A study on calcination temperature and atmosphere dependence*, The Beilstein Journal of Nanotechnology, 6 (2015) 47-59

M. Augustin, O. Yezerka, D. Fenske, I. Bardenhagen, A. Westphal, M. Knipper, T. Plaggenborg, J. Kolny-Olesiak, J. Parisi, *Mechanistic study on the activity of manganese oxide catalysts for oxygen reduction reaction in an aprotic electrolyte*, Electrochimica Acta, 158 (2015) 383-389

Konferenzbeiträge

M. Augustin, O. Yezerka, J. Derendorf, M. Knipper, D. Fenske, T. Plaggenborg, J. Parisi, *Colloidal Manganese Oxide Nanoparticles as Bifunctional Catalysts for Oxygen Reduction and Evolution Reactions in Lithium/Air Batteries*, 221st Meeting of the Electrochemical Society 2012, Seattle, USA, Vortrag

M. Augustin, D. Fenske, T. Plaggenborg, J. Parisi, *Colloidal Synthesis of Mn Alkoxides as Precursors for Bifunctional Oxide Electrocatalysts in Li/Air Batteries*, Electrochemistry-Tagung der Gesellschaft Deutscher Chemiker 2012, München, Vortrag

M. Augustin, D. Fenske, T. Plaggenborg, J. Parisi, *Colloidal Synthesis of Manganese Glycolate Particles as Precursor for Bifunctional Manganese Oxide Electrocatalysts in Li/Air Batteries*, Konferenz „Next Generation Batteries – Materials, Technology, and Applications“ 2013, Delmenhorst, Posterbeitrag

M. Augustin, D. Fenske, M. Knipper, T. Plaggenborg, J. Kolny-Olesiak, J. Parisi, *High Surface Manganese Oxides as Bifunctional Catalysts for the Oxygen Reduction and Evolution Reactions in Metal/Air Batteries*, Ulm ElectroChemical Talks 2014, Ulm, Posterbeitrag

M. Augustin, I. Bardenhagen, D. Fenske, M. Knipper, T. Plaggenborg, J. Kolny-Olesiak, J. Parisi, *Manganese Oxides as Catalysts for the Oxygen Reduction Reaction in Metal/Air Batteries*, Electrochemistry-Tagung der Gesellschaft Deutscher Chemiker 2014, Mainz, Posterbeitrag

Erklärung

Hiermit erkläre ich, dass ich die Dissertation selbstständig verfasst habe und dass die benutzten Hilfsmittel vollständig angegeben sind. Die vorliegende Arbeit wurde in Teilen bereits veröffentlicht. Die jeweiligen Textabschnitte sind entsprechend gekennzeichnet und eine Publikationsliste ist beigefügt.

Des Weiteren erkläre ich, dass die Dissertation weder in ihrer Gesamtheit noch in Teilen einer anderen Hochschule zur Begutachtung in einem Promotionsverfahren vorliegt oder vorgelegen hat. Die Leitlinien guter wissenschaftlicher Praxis der Carl von Ossietzky Universität Oldenburg wurden bei der Erstellung dieser Arbeit befolgt. Es wurden im Zusammenhang mit dem Promotionsvorhaben keine kommerziellen Vermittlungs- oder Beratungsdienste in Anspruch genommen.

Oldenburg, den 25. Juni 2015

Matthias Augustin